Determination of Bragg Scatter in an Aircraft Generated Wake Vortex System for Radar Detection

Theodore J. Myers

Dissertation submitted to the Faculty of the Virginia Polytechnic Institute and State University in partial fulfillment of the requirements for the degree of

Doctor of Philosophy
in
Electrical Engineering

W. A. Scales, Chair
G. S. Brown
W. A. Davis
W. J. Devenport
D. A. DeWolf
R. E. Marshall
S. A. Ragab

September 5, 1997
Blacksburg, Virginia

Keywords: Wake Vortex, Bragg, Radar, Radar Cross Section, Doppler Radar

Determination of Bragg Scatter in an Aircraft Generated Wake Vortex System for Radar Detection

Theodore J. Myers

(ABSTRACT)

Remote detection and tracking of wingtip generated wake vortices is important for hazard avoidance especially near airports. Aircraft that fly through these hazardous vortices experience sudden induced roll. Experiments have demonstrated that there is sufficient radar cross section for remote detection at frequencies ranging from VHF to C band (100 MHz to 5 GHz). The mechanism that yields this radar cross section is Bragg scattering from the index of refraction variations due to the atmospheric water vapor and potential temperature fields being mixed by the wake vortex system. Refractive index variations of the size that correspond to half the operating radar wavelength produce the observed radar return. Previous analysis has postulated turbulence within the wake vortex to be the generator of the index of refraction variations. In this work, a new mechanism is identified that does not assume turbulence within the wake vortex system. This "laminar flow mechanism" causes refractive index structuring that stretches into successively smaller spirals over time as the wake vortex system swirls and descends through the stratified atmosphere. The results are quantitatively consistent with experimental data. Results indicate that this new mechanism has a sharply peaked doppler spectrum which is encouraging for coherent detection by doppler radar.

Dedication

This work is dedicated to the memory of Jonathon Wells, my high school physics teacher. His enthusiasm, patience, and vast understanding of science helped me choose my life's direction.

Acknowledgement

I would like to thank all those that made this work possible. My advisor, Dr. Wayne Scales, was extremely helpful and supportive and I am honored to have worked with someone of such talent and dedication. I would also like to thank all of the members of the committee for their encouragement and valuable guidance. I would especially like to thank my mother, Carole, and my father, Scott, who have always been there for me.

Contents

1 Introduction **1**

1.1 Wake Vortex Hazard 1

1.2 Radar Detection 2

1.3 Bragg Scatter of Electromagnetic Waves From the Wake Vortex System . . 4

1.4 Previous RCS Determination 5

1.5 Wake Vortex - Passive Conservative Simulation (WV-PCS) 7

1.6 WV-PCS Model Assumptions 7

1.7 Doppler Processor Simulator (DPS) 9

1.8 Overview 10

2 Previous Wake Vortex Radar Cross Section Determination **11**

2.1 TASS Model 12

2.2 Determination of Reflectivity 14

2.3 Consequences of Erroneous Closure 15

2.4 General Derivation of RCS From Refractive Index Field 16

3 Coherent Bragg Scatter Via Laminar Mixing Mechanism and Simulation Overview 24

3.1 RCS Derivation From Passive Conservative Simulation 26

3.1.1 Potential Temperature 27

3.1.2 First Order Approximation 28

3.1.3 Zero Pressure Gradient Approximation 29

3.1.4 Generalize Passive Conservative 29

3.1.5 Determination of RCS 32

3.2 WV-PCS Assumptions and Justifications 33

3.2.1 Crow Instability 33

3.2.2 Pre-Rollup Homogenization 34

3.2.3 No Turbulence Assumption 35

3.2.4 Constant Descent Rate 36

3.3 Extension to Other Aircraft 36

4 Wake Vortex - Passive Conservative Simulation (WV-PCS) 41

4.1 Finite Difference Formulation 42

4.1.1 Equation Set 42

4.1.2 Finite Difference Formulation 42

4.2 Boundary Conditions 43

4.3 Grid Spacing 44

4.4 Even-Odd Instability 46

4.5 Velocity Field 49

4.6 Upwash Velocity 50

4.7 Courant Condition 52

4.8 WV-PCS Output 53

5 Radar Cross Section Determination **55**

5.1 Determination of Atmospheric Parameter, A 55

5.2 Temporal Evolution of Water Vapor Distribution 56

5.3 Temporal Evolution of RCS Spectrum 61

5.3.1 C-5A 61

5.3.2 747 72

5.4 Temporal Evolution of RCS at Selected Bands 77

5.5 Extrapolated Radar Cross Section 81

5.6 Bistatic Radar Cross Section 85

6 Doppler Processing **87**

6.1 Doppler Processing Simulation (DPS) 88

6.2 Temporal Evolution of Doppler Spectra 92

6.2.1 C5-A 95

6.2.2 747 121

6.3 Effect of Coherent Processing Interval (CPI) 129

7 Conclusions **136**

7.1 Summary 136

7.2 Future Work 138

List of Figures

1.1 Wake Vortex Creation [Gilson, 1991] 2

1.2 Bragg Scatter 5

1.3 Turbulent and Laminar Scattering Mechanisms 8

3.1 Evolution of the downstream average of the tracer concentrations for the ER-2 wake at 15 s, 30 s, 62 s, and 325 s [Lewellen and Lewellen, 1996] . . . 34

3.2 Descent of Wake Vortex System [Proctor, 1996] 36

4.1 Full Computational Grid, C5-A and 747 47

4.2 Computational Grid Over Vortex Core, C-5A and 747 48

5.1 Full View of Water Vapor Distribution for C-5A, 70 Seconds After Rollup . 58

5.2 Spiral Visualization of Water Vapor for C-5A, 5-40 Seconds 59

5.3 Spiral Visualization of Water Vapor for C-5A, 50-100 Seconds 60

5.4 Evolution of RCS for C-5A, 5-20 Seconds, 90^o Look Angle 64

5.5 Evolution of RCS for C-5A, 5-20 Seconds, 0^o Look Angle 65

5.6 Evolution of RCS for C-5A, 30-60 Seconds, 90^o Look Angle 66

5.7 Evolution of RCS for C-5A, 30-60 Seconds, 0^o Look Angle 67

5.8 Evolution of RCS for C-5A, 70-100 Seconds, 90^o Look Angle 68

5.9 Evolution of RCS for C-5A, 70-100 Seconds, 0^o Look Angle 69

5.10 Evolution of RCS for C-5A, 110-115 Seconds, 90^o Look Angle 70

5.11 Evolution of RCS for C-5A, 110-115 Seconds, 90^o Look Angle 71

5.12 Evolution of RCS for 747, 5-20 Seconds, 90^o Look Angle 73

5.13 Evolution of RCS for 747, 5-20 Seconds, 0^o Look Angle 74

5.14 Evolution of RCS for 747, 25-35 Seconds, 90^o Look Angle 75

5.15 Evolution of RCS for 747, 25-35 Seconds, 0^o Look Angle 76

5.16 RCS Evolution for C-5A at 90^o Look Angle 78

5.17 RCS Evolution for C-5A at 0^o Look Angle 79

5.18 RCS Evolution for 747 at 90^o Look Angle 80

5.19 Extrapolated vs. Actual 747 RCS 83

5.20 Extrapolated Learjet-36 RCS 84

5.21 Bistatic vs. Monostatic RCS 86

6.1 Doppler Processor [Schleher, 1991] 88

6.2 Doppler Processing for C-5A, 90^o Look Angle, 10 Seconds 97

6.3 Doppler Processing for C-5A, 90^o Look Angle, 20 Seconds 98

6.4 Doppler Processing for C-5A, 90^o Look Angle, 30 Seconds 99

6.5 Doppler Processing for C-5A, 90^o Look Angle, 40 Seconds 100

6.6 Doppler Processing for C-5A, 90^o Look Angle, 50 Seconds 101

6.7 Doppler Processing for C-5A, 90^o Look Angle, 60 Seconds 102

6.8 Doppler Processing for C-5A, 90^o Look Angle, 70 Seconds 103

6.9 Doppler Processing for C-5A, 90^o Look Angle, 80 Seconds 104

6.10 Doppler Processing for C-5A, 90^o Look Angle, 90 Seconds 105

6.11 Doppler Processing for C-5A, 90^o Look Angle, 100 Seconds 106

6.12 Doppler Processing for C-5A, 90^o Look Angle, 110 Seconds 107

6.13 Doppler Processing for C-5A, 0^o Look Angle, 10 Seconds 110

6.14 Doppler Processing for C-5A, 0^o Look Angle, 20 Seconds 111

6.15 Doppler Processing for C-5A, 0^o Look Angle, 30 Seconds 112

6.16 Doppler Processing for C-5A, 0^o Look Angle, 40 Seconds 113

6.17 Doppler Processing for C-5A, 0^o Look Angle, 50 Seconds 114

6.18 Doppler Processing for C-5A, 0^o Look Angle, 60 Seconds 115

6.19 Doppler Processing for C-5A, 0^o Look Angle, 70 Seconds 116

6.20 Doppler Processing for C-5A, 0^o Look Angle, 80 Seconds 117

6.21 Doppler Processing for C-5A, 0^o Look Angle, 90 Seconds 118

6.22 Doppler Processing for C-5A, 0^o Look Angle, 100 Seconds 119

6.23 Doppler Processing for C-5A, 0^o Look Angle, 110 Seconds 120

6.24 Doppler Processing for 747, 90^o Look Angle, 5 Seconds 122

6.25 Doppler Processing for 747, 90^o Look Angle, 10 Seconds 123

6.26 Doppler Processing for 747, 90^o Look Angle, 15 Seconds 124

6.27 Doppler Processing for 7476, 90^o Look Angle, 20 Seconds 125

6.28 Doppler Processing for 747, 90^o Look Angle, 25 Seconds 126

6.29 Doppler Processing for 747, 90^o Look Angle, 30 Seconds 127

6.30 Doppler Processing for 747, 90^o Look Angle, 35 Seconds 128

6.31 Peak Effective RCS as a Function of CPI 131

6.32 VHF Peak Effective RCS 132

6.33 UHF Peak Effective RCS 133

6.34 L-Band Peak Effective RCS 134

6.35 S-Band Peak Effective RCS 135

List of Tables

4.1 Grid Parameters for C5-A and 747 46

4.2 C-5A Simulation Parameters 51

4.3 747 Simulation Parameters 51

4.4 Wavelengths for Specific Frequency Bands 54

5.1 Environmental Parameters 56

5.2 Reported Radar Cross Sections at 90 Seconds for a C5-A at a 90^o Look Angle 81

5.3 Reported Radar Cross Sections at 90 Seconds for a C5-A at a 10^o Look Angle 81

5.4 Learjet-36 Parameters 82

6.1 Learjet-36 Parameters 93

6.2 Doppler Processor Summary, C5-A, 0^o Look Angle 94

6.3 Doppler Processor Summary, 747, 90^o Look Angle 94

7.1 Frequency Dependence of Important Wake Vortex Detection Parameters . 137

Chapter 1

Introduction

As an airplane passes through the atmosphere, an impulsive force is given to the air surrounding the wings which forms a planar wake. As the planar wake is an unstable velocity field, the wake rolls up around the lift discontinuity created at the tip of the wings. This forms the system of counter-rotating vortices shown in Figure 1.1.

1.1 Wake Vortex Hazard

Aircraft generated wake vortices from larger aircraft pose a danger when a smaller aircraft flies through the vortex system and experiences sudden and often unexpected induced roll. Between 1986 and 1992, there were 48 reported encounters with wake vortices [ASRS, 1992].

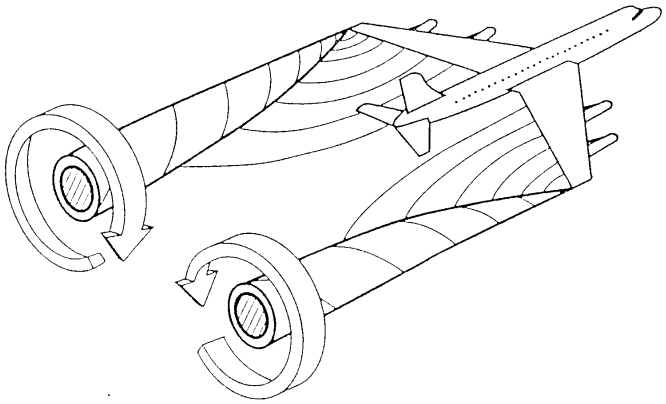

Figure 1.1: Wake Vortex Creation [Gilson, 1991]

Remote detection by radar of wake vortices would be an effective technique for avoidance of the threat. In addition, remote tracking of wake vortices would allow a determination of minimum safe spacing between landing aircraft. This would result in an increase in airport throughput for those airports where aircraft spacing is the bottleneck.

1.2 Radar Detection

Radio detection and ranging (radar) consists of a transmitter that emits a propagating electromagnetic wave in the direction of an anticipated target and a receiver that detects scattered energy from this target. In most cases, the transmitter and receiver are co-located (located in the same place.) This system is referred to as a monostatic radar system and uses the backscattered energy as input into the receiver for detection. In some cases however, a bistatic system is constructed where the transmitter and receiver are in two different locations. In this system, the energy into the receiver comes from the transmitted energy

scattered by the target in the direction of the receiver.

The radar equation is the the relationship between the design parameters and the resulting signal-to-noise ratio (SNR). The SNR of a single pulse for detection of the wake vortex system is [Eaves and Reedy, 1987]

$$(SNR)_{pulse} = \frac{PG^2\lambda^2\sigma\ell}{(4\pi)^3 R^4 kTBL_a L} \tag{1.1}$$

where

P = peak transmitted power

G = one-way antenna gain

λ = wavelength

σ = radar cross section of the wake vortex system

ℓ = length of the wake vortex within the angular resolution

R = range to the target

k = Boltzmann's constant

T = system temperature in degrees Kelvin

B = bandwidth of the waveform

L_a = atmospheric propagation loss

L = other system losses.

In particular, its important to notice that the SNR is proportional to the radar cross section

(RCS), σ of the target. This dissertation focuses strongly on RCS determination of the wake vortex system. Determining the RCS of a target is very important for the design of the radar system.

1.3 Bragg Scatter of Electromagnetic Waves From the Wake Vortex System

The interaction of the wake vortex system with electromagnetic radiation occurs due to the electrical characteristics of the atmosphere which is mixed by the wake vortex system. The refractive index field, $n(\mathbf{r}, t)$, of the atmosphere is a function of pressure, temperature, and water vapor content. This atmospheric index of refraction is very close to the free space value of unity with the spatially varying atmospheric parameters causing a small perturbation.

It is this small perturbation that interacts with electromagnetic radiation and causes scattering. Since the perturbation is small, the corresponding reflection is also small but measurable. This is the basis of remote detection of hazardous, aircraft wake vortices using radar.

A relationship between a small refractive index perturbation field and RCS has been established [Tartarski, 1971]. The RCS at a given frequency is related to the spatial Fourier transform of the perturbing refractive index field at the wavenumber corresponding to half of the radar wavelength and in the direction of propagation of the electromagnetic wave (see Figure 1.2). This has a similarity to scattering from the periodic structures in crystals observed by Bragg and so this mechanism is referred to as Bragg scatter.

Bragg scatter has been observed at microwave frequencies ranging from VHF to C-Band.

This corresponds to half radar wavelengths of between approximately 5 cm and 1 m.

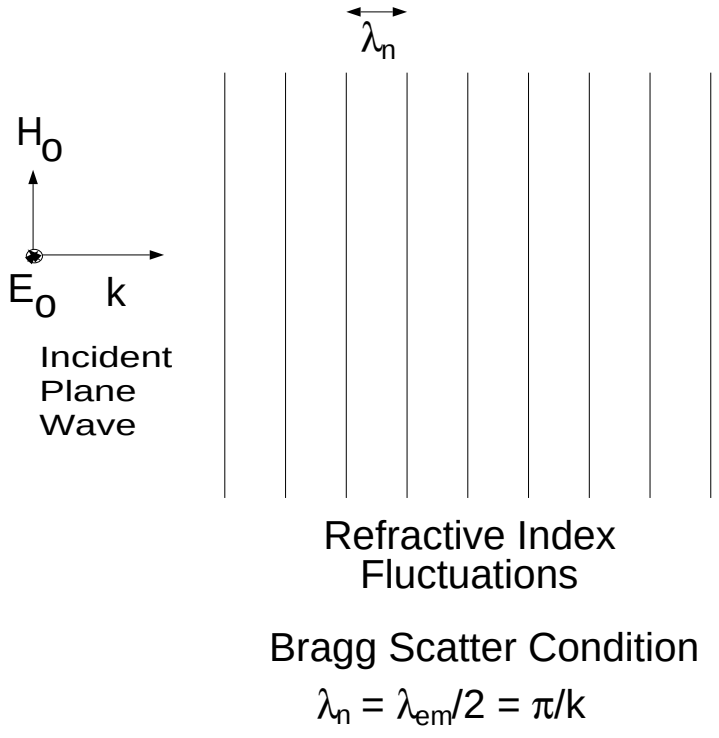

Figure 1.2: Bragg Scatter

1.4 Previous RCS Determination

Previous work has been done in an attempt to quantify RCS from Bragg scatter [Marshall et al., 1996] under the assumption of turbulent mixing of the atmosphere by the wake vortex. Turbulence causes a cascading of energy from the input scale (on order of the wake vortex) to the small scale size where the energy is dissipated by viscous effects

into heat. It has been demonstrated that there is RCS over the wide range of frequencies whose half wavelength corresponds to the inertial subrange [Tennekes and Lumley, 1972]. The turbulent RCS is weakly dependent upon the frequency of operation of the radar and is proportional to the structure constant C_n^2. The structure constant is dependent upon the strength of the turbulence (which eddy dissipation rate is a measure of) and the concentration gradients of atmospheric parameters that make the turbulent eddys visible to radar.

The previous work utilized the output of a large eddy simulation (LES) model called Terminal Area Simulation System (TASS) to find the eddy dissipation rate and the mean flow concentration gradients. LES is a type of simulation that models the small scales that tend to be isotropic and universal in nature (through the use of a closure assumption) and simulates the evolution of the large scale structures. From the outputted eddy dissipation rate and mean flow concentration gradients, a value of RCS was determined [Tartarski, 1971, Ottersten, 1969b].

The modeling of the small scales in the LES model depends on the closure assumptions. The TASS model uses Smagorinski closure. This closure relationship has a direct bearing on the eddy dissipation rate and turbulence mixing rates calculated. Recent literature has indicated that Smagorinski closure greatly overestimates turbulence levels within a wake vortex system [Zeman, 1995] which means that, in actuality, the reported eddy dissipation rate from the TASS model is unrealistically large and this subsequently causes an unrealistically large RCS to be calculated. This indicates that turbulence is not responsible for generating the experimentally reported Bragg RCS. Also, TASS similarly overestimates the amount of turbulent mixing in the wake vortex system meaning that any long term structure of the stratified atmosphere by the mean flow is destroyed by unrealistically large turbulent mixing rates.

1.5 Wake Vortex - Passive Conservative Simulation (WV-PCS)

As will be shown, RCS determination of the wake vortex system can be approximated by simulating the flow of a passive conservative field. "Passive" means that these quantities do not effect the form of the velocity field; "conservative" indicates that there are no source or sinks thus the volume integral of the quantity is conserved. Relevant examples of passive conservative fields include water vapor content and potential temperature. The Wake Vortex - Passive Conservative Simulation (WV-PCS) is used to determine the evolution of a generalized passively conserved quantity, $s(\mathbf{r}, t)$, of the wake vortex of a particular aircraft. This term represents a passive conservative field as it undergoes advection and diffusion under the influence of the velocity field of the counter-rotating pair of wake vortices.

Figure 1.3 illustrates the difference between the previously thought scattering mechanism and the newly proposed laminar mixing mechanism.

1.6 WV-PCS Model Assumptions

There are factors that a 3-dimensional LES model may effectively account for which the WV-PCS can not. The long wavelength instabilities that develop in the wake vortex system such as the Crow instability or vortex linking are 3-dimensional effects and are not modeled. Previous work, however, indicates that these effects evolve slowly and do not have feature sizes at the short wavelengths that govern RCS [Lewellen and Lewellen, 1996]. This does not necessarily mean that these instabilities do not affect the laminar mixing process, but that they do not cause RCS directly and that there is a large period of time where these effects are negligible. This is the region of validity for the WV-PCS.

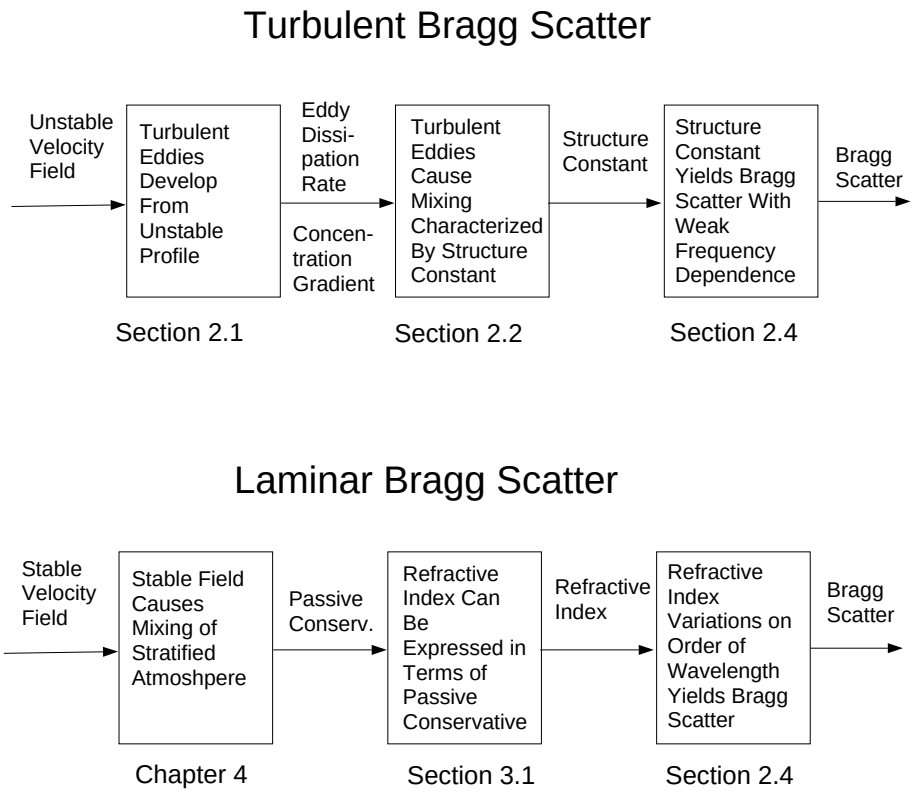

Figure 1.3: Turbulent and Laminar Scattering Mechanisms

Rollup is defined as the point where the wake of an aircraft has "rolled up" into the pair of counter-rotating wake vortices shown in Figure 1.1. The WV-PCS does not simulate pre-rollup turbulence which is generated by the wake. This turbulence may serve to affect the initial conditions of the passive conservative distribution. Specifically, pre-rollup turbulence causes enhanced mixing which may lead to homogenization of atmospheric parameters. The effect of this needs further study.

The WV-PCS uses the assumption of a constant descent rate for the wake vortex system. Whereas the TASS model is capable of factoring in buoyancy effects and ground effects, the WV-PCS is not because the velocity field is modeled, not simulated. Experimental evidence as well as TASS model output shows that the constant descent velocity assumption is reasonable.

Another very important feature of the wake vortex system is that the form of the flow remains relatively constant or self-similar. This, in conjunction with the previous assumptions, allows for an a priori determination of the wake vortex system velocity field. This permits a closed form model of the velocity distribution as a function of space and time.

1.7 Doppler Processor Simulator (DPS)

Doppler radar allows an enhanced detection capability. This allows detection of much weaker radar returns if salient features of the doppler spectrum are known in advance. The output of the WV-PCS serves as input into the Doppler Processing Simulator (DPS). The DPS allows determination of the effectiveness of doppler processing in a real time system for detection of the wake vortex hazard. The SNR improvement from the doppler processing is evaluated as a function of various design parameters and processing algorithms. This information may serve as input into the selection of the parameters of a real time doppler

radar system.

1.8 Overview

This dissertation discusses a newly proposed RCS generating mechanism that relies on mixing of the initially stratified water vapor content and potential temperature fields by the mean flow over a relatively large period of time. Chapter 2 gives a more detailed explanation of previous RCS determination work when turbulent mixing was assumed. The inconsistency of this work with recent literature will be discussed. In addition, Chapter 2 quantifies Bragg scatter beginning with fundamental principles (Maxwell's Equations). Chapter 3 presents the long term laminar flow mixing mechanism and an overview of the WV-PCS used to quantify this mechanism. The assumptions made will be justified and the limitations of the model will be presented. Chapter 4 discusses the details of the WV-PCS and the numerical methods used. Chapter 5 gives the results of the WV-PCS. Aids to visualize the formation of the passive conservative spirals are shown and the temporal evolution of RCS as a function of frequency are shown for the C5-A (for which experimental results exist) and the 747. Chapter 6 explores the temporal evolution of the doppler spectrum that coherent processing will yield for various radar frequencies for both the C-5A and the 747. Chapter 7 presents the conclusions, recommendations regarding future simulation work, and recommendations for hardware issues related to the development of a system used to track and detect hazardous wake vortices.

Chapter 2

Previous Wake Vortex Radar Cross Section Determination

The previous work performed in quantifying RCS employs the Terminal Area Simulation System (TASS) model [Proctor, 1996]. This model uses a modified first order Smagorinski closure to model the sub-grid turbulence. Based on the output of the TASS model, RCS is calculated by using previously developed relationships [Ottersten, 1969a, Tartarski, 1971] that will be explained in more detail. Note that the validity of this approach is dependent upon the accuracy of the closure model used. Recent work has indicated that the Reynold's stress closure (RSC) models (of which Smagorinski closure is one) greatly overpredict the turbulence levels in a wake vortex system [Zeman, 1995].

2.1 TASS Model

The complete TASS equation set in standard tensor notation is given using the Einstein summing convention. All variables represent the mean quantity of the variables, subgrid turbulence is modeled using a closure relationship.

The momentum equation is

$$\frac{\partial u_i}{\partial t} + \frac{H}{\rho_o}\frac{\partial \rho}{\partial x_i} = -\frac{\partial u_i u_j}{\partial x_j} + u_i\frac{\partial u_j}{\partial x_j} + g(H-1)\delta_{i3} - 2\Omega_j(u_k - u_{ok})\epsilon_{ijk} + \frac{1}{\rho_o}\frac{\partial \tau_{ij}}{\partial x_j} \tag{2.1}$$

where the buoyancy term is defined as

$$H = \left[\frac{\theta}{\theta_o} - \frac{\rho C_\nu}{P_{oo}C_p}\right]\left[1 + 0.61(Q_\nu - Q_{\nu o}) - Q_T\right]. \tag{2.2}$$

The pressure deviation equation is

$$\frac{\partial p}{\partial t} + \frac{C_p P}{C_\nu}\frac{\partial u_j}{\partial x_i} = \rho_o g u_j \delta_{j3} + \frac{C_p P}{C_\nu \theta}\frac{\partial \theta}{\partial t}. \tag{2.3}$$

The thermodynamic equation used is

$$\frac{\partial \theta}{\partial t} = -\frac{1}{\rho_o}\frac{\partial \rho_o u_j}{\partial x_j} + \frac{\theta}{\rho_o}\frac{\partial \rho_o u_j}{\partial x_j} + \frac{1}{\rho_o}\frac{\partial S_j(\theta)}{\partial x_j} + \frac{\theta}{LC_p}[L_\nu s_\nu + L_f S_f + L_s S_s] \tag{2.4}$$

with the potential temperature θ defined as

$$\theta = T\left(\frac{P_{oo}}{P}\right)^{\frac{R_d}{C_p}}. \tag{2.5}$$

u_i is the component of the velocity vector, t is time, p is deviation from atmospheric pressure P, T is atmospheric temperature, ρ is the air density, Ω is the earth's angular velocity, C_p and C_ν are the specific heats of air at constant pressure and volume respectively, g is the acceleration due to gravity, R_d is the gas constant for dry air, P_{oo} is a constant equivalent to 1000 millibars of pressure, Q_T is the sum of the mixing ratios for liquid and ice water substances, L_ν is the latent heat of vaporization for water, L_f is the latent heat for fusion for water, L_s is the latent heat for sublimation of water, and s_ν, s_f, and s_s are the respective water source substance term.

The advection and diffusion of a passive conservative is described by

$$\frac{\partial q}{\partial t} = -\frac{1}{\rho_o}\frac{\partial q \rho_o u_j}{\partial x_j} + \frac{q}{\rho_o}\frac{\partial \rho_o u_j}{\partial x_j} + \frac{1}{\rho_o}\frac{\partial S_j(q)}{\partial x_j} \tag{2.6}$$

where q is the mixing ratio for water vapor and $S_j(q)$ is the term due to turbulent mixing and is described by

$$S_j(q) = 3\rho_o K_M \frac{\partial q}{\partial x_j}. \tag{2.7}$$

As was mentioned before, Smagorinski closure is used in the TASS model. The subgrid stress, τ_{ij}, in Equation 2.1 is

$$\tau_{ij} = \rho_o K_M \left[\frac{\partial u_i}{\partial x_j} + \frac{\partial u_j}{\partial x_i} - \frac{2\partial u_k}{3\partial x_k}\right] \tag{2.8}$$

where K_M is the sub-grid eddy viscosity modeled as

$$K_M = l_s^2 \sqrt{\frac{\partial u_i}{\partial x_j}\left(\frac{\partial u_i}{\partial x_j} + \frac{\partial u_j}{\partial x_i}\right) - \frac{2}{3}\left(\frac{\partial u_k}{\partial x_k}\right)^2} \times \sqrt{1 - R_f} \tag{2.9}$$

where R_f is the flux Richardson number and l_s is the subgrid length scale.

The eddy dissipation rate, ϵ, is then calculated as

$$\epsilon = \sum_{ij} u_i \frac{\partial \tau_{ij}}{\partial x_j}. \tag{2.10}$$

2.2 Determination of Reflectivity

The eddy dissipation rate and the mean quantities of thermodynamic variables are output by TASS and then substituted into the following relationship obtained [Ottersten, 1969a] and extended to two dimensions for for the wake vortex geometry [Marshall et al., 1996]

$$C_n^2 = \epsilon^{2/3} \frac{\left(\frac{d\phi}{dx}\right) + \left(\frac{d\phi}{dy}\right)}{\left(\left(\frac{du}{dx}\right)^2 + \left(\frac{du}{dy}\right)^2 + \left(\frac{dv}{dx}\right)^2 + \left(\frac{dv}{dy}\right)^2\right)(1 - R_f)} \tag{2.11}$$

where ϕ is the potential refractive index determined from output TASS quantities as

$$\phi = \frac{79p}{\theta}\left(1 + \frac{7776pq}{\theta}\right), \tag{2.12}$$

p (mb) is pressure, q (g/kg) is water vapor content, θ (K) is potential temperature, u and v are the x and y components respectively of mean velocity, and R_f is the flux Richardson number.

The theory of equilibrium and isotropic turbulence as explained by Tartarski [Tartarski, 1971] relates the volume reflectivity η ($\mathrm{dBm}^3/\mathrm{m}$) to a structure constant of the turbulence and a weak frequency dependence as

$$\eta = 0.38\lambda^{-1/3}C_n^2 \tag{2.13}$$

where C_n is the structure constant that characterizes the turbulence and λ is the radar wavelength in meters.

From Equation 2.13, RCS may be determined by the integrated reflectivity as

$$\sigma = \int \eta \, d\sigma \tag{2.14}$$

where the integration is performed over the cross section of the wake vortex system.

2.3 Consequences of Erroneous Closure

As was mentioned earlier, recent literature has indicated that Smagorinski closure greatly overpredicts the turbulence levels in the wake vortex system. The more realistic value for eddy dissipation rate, ϵ, introduced in Equation 2.10 is close to zero. Consequently, Equation 2.11 indicates that the structure constant, C_n^2, would be more realistically close to zero and this translates into the reflectivity η being near zero in Equation 2.13.

The other effect of very small turbulence levels is that Equation 2.6, which describes the evolution of a passive conservative, greatly overpredicts the diffusion rate. With very little turbulence, molecular diffusion dominates, and the more accurate equation describing the advection and diffusion of a passive conservative would be

$$\frac{\partial q}{\partial t} = -\frac{1}{\rho_o}\frac{\partial q \rho_o u_j}{\partial x_j} + \frac{q}{\rho_o}\frac{\partial \rho_o u_j}{\partial x_j} + \frac{D}{\rho_o}\frac{\partial^2 q}{\partial x_j^2} \tag{2.15}$$

where D is the coefficient of molecular diffusion.

The fact that artificially large turbulent diffusion was used in Equation 2.6 destroys any coherent structure created from advection of the mean variables. As will be shown, this is what causes RCS, not the reflectivity from turbulent eddies.

2.4 General Derivation of RCS From Refractive Index Field

For determination of RCS, it is necessary to use a more general relationship that is independent of whether the mixing mechanism is due to laminar or turbulent processes. The general relationship has been previously derived [Tartarski, 1971] and is presented here.

To quantify the Bragg scattering mechanism, it is necessary to begin with Maxwell's equations. For a time harmonic field, the relevant vector equations in mks units are

$$\nabla \times \mathbf{E} = -j\omega\mu\mathbf{H} \tag{2.16}$$

$$\nabla \times \mathbf{H} = j\omega\epsilon\mathbf{E} \tag{2.17}$$

$$\nabla \cdot \epsilon\mathbf{E} = 0 \tag{2.18}$$

where $\mathbf{E}$ is the electric field intensity, $\mathbf{H}$ is the magnetic field intensity, ϵ is the permittivity of the atmosphere which is a spatially varying function, and μ is the permeability of the atmosphere taken to be equal to the free space value μ_o.

Taking the curl of Equation 2.16, substituting into Equation 2.17, and using the vector identity $\nabla \times \nabla \times \mathbf{E} = -\nabla^2\mathbf{E} + \nabla(\nabla \cdot \mathbf{E})$ yields

$$-\nabla^2\mathbf{E} + \nabla(\nabla \cdot \mathbf{E}) = k^2\mathbf{E} \tag{2.19}$$

where $k = \omega\sqrt{\mu\epsilon}$.

Equation 2.18 can be expanded as

$$\nabla \cdot \epsilon\mathbf{E} = \epsilon\nabla \cdot \mathbf{E} + \mathbf{E} \cdot \nabla\epsilon = 0. \tag{2.20}$$

Using the relations $\frac{\epsilon}{\epsilon_o} = n^2$ and $k_o = \omega\sqrt{\mu_o\epsilon_o}$ where ϵ_o is the permittivity of free space, and substituting Equation 2.20 into equation Equation 2.19 yields

$$\nabla^2\mathbf{E} + k_o^2 n^2\mathbf{E} + 2\nabla\left(\mathbf{E} \cdot \frac{\nabla n}{n}\right) = 0. \tag{2.21}$$

We may decompose the refractive index field as follows

$$n = n_o + n_1 \tag{2.22}$$

where n_1 represents the very small perturbation of refractive index from its free space value of n_o.

Next, we may expand the electric field, $\mathbf{E}$, as

$$\mathbf{E} = \mathbf{E_o} + \mathbf{E_1} + \mathbf{E_2} + \ldots \tag{2.23}$$

where the k^{th} term of the series has the order of smallness n_1^k. Substituting Equations 2.22 and 2.23 into Equation 2.21 and noting that $n_o = 1$

$$\begin{aligned} \nabla^2(\mathbf{E_o} + \mathbf{E_1} + \ldots) &+ k_o^2(1+n_1)^2(\mathbf{E_o} + \mathbf{E_1} + \ldots) \\ &+ 2\nabla\left((\mathbf{E_o} + \mathbf{E_1} + \ldots) \cdot \frac{\nabla(1+n_1)}{1+n_1}\right) = 0. \end{aligned} \tag{2.24}$$

Keeping the first order terms and noting that $\frac{1}{1+n_1} \approx 1$ yields

$$\nabla^2\mathbf{E_1} + k_o^2\mathbf{E_1} = -2k_o^2 n_1 \mathbf{E_o} - 2\nabla\left(\mathbf{E_o} \cdot \nabla n_1\right). \tag{2.25}$$

Equation 2.25 is valid only if the second order term $2\nabla\left(\mathbf{E_1} \cdot \nabla n_1\right)$ is negligible or

$$2\nabla\left(\mathbf{E_1} \cdot \nabla n_1\right) << k_o^2\mathbf{E_1}. \tag{2.26}$$

If k_n is taken to be the highest wavenumber describing the perturbation n_1, then this condition may be approximated as

$$n_1 << \frac{1}{2}\left(\frac{k_o}{k_n}\right)^2 = \frac{1}{2}\left(\frac{\lambda_n}{\lambda_o}\right)^2 \tag{2.27}$$

where λ_o and λ_n are the smallest wavelength component of the incident electromagnetic field and the refractive index perturbation respectively.

Since $\mathbf{E_o}$ is a solution to the unperturbed equation, we can make it assume the form of an incident plane wave in free space as

$$\mathbf{E_o} = E_o e^{-j\mathbf{k_t}\cdot\mathbf{r}}\hat{\mathbf{p}} \tag{2.28}$$

where $\hat{\mathbf{p}}$ is the unit vector denoting the polarization of the electric field, $\mathbf{k_t}$ is in the direction of propagation with $|\mathbf{k_t}| = k_o$, and $\mathbf{k_t}$ is perpendicular to $\hat{\mathbf{p}}$.

Now, we may treat the left hand side as the familiar wave equation and the right hand side, $f(\mathbf{r})$, as a source term

$$\nabla^2\mathbf{E_1} + k_o^2\mathbf{E_1} = f(\mathbf{r}) \tag{2.29}$$

and

$$f(\mathbf{r}) = -2k_o^2 n_1\mathbf{E_o} - 2\nabla\left(\mathbf{E_o}\cdot\nabla n_1\right). \tag{2.30}$$

We may solve for $\mathbf{E_1}$ using the standard Green's function for the wave equation

$$\mathbf{E_1}(\mathbf{r}) = -\frac{1}{4\pi}\int_V f(\mathbf{r}')\frac{e^{-jk_o|\mathbf{r}-\mathbf{r}'|}}{|\mathbf{r}-\mathbf{r}'|}\,dV' \tag{2.31}$$

where $\mathbf{r}$ is the vector describing the field position and $\mathbf{r}'$ is the vector describing the source position.

When the condition $\lambda r >> L^2$ is satisfied where L is the dimension of the scattering volume, λ is the wavelength of the electromagnetic wave, and $r = |\mathbf{r}|$, the Fraunhofer or far field approximation of the Green's function is valid

$$\mathbf{E_1}(r) = -\frac{1}{4\pi}\frac{e^{-jk_o r}}{r}\int_V f(\mathbf{r}')e^{j\mathbf{k_r}\cdot\mathbf{r}'}\,dV' \tag{2.32}$$

where $\mathbf{k_r}$ is the vector from the scattering volume to the observation point with $|\mathbf{k_r}| = k_o$.

Substituting $f(\mathbf{r})$ from Equation 2.30 and the form for the electric field in Equation 2.28 into the Fraunhofer approximation of Equation 2.32 yields

$$\begin{aligned} \mathbf{E_1}(r) &= \frac{E_o k_o^2}{2\pi}\frac{e^{-jk_o r}}{r}\hat{\mathbf{p}}\int_V n_1(\mathbf{r'})e^{-j\mathbf{k_t}\cdot\mathbf{r'}+j\mathbf{k_r}\cdot\mathbf{r'}}\,dV' + \\ &+ \frac{E_o}{2\pi}\frac{e^{-jk_o r}}{r}\int_V \nabla\left(e^{-j\mathbf{k_t}\cdot\mathbf{r}}\hat{\mathbf{p}}\cdot\nabla n_1(\mathbf{r'})\right)e^{j\mathbf{k_r}\cdot\mathbf{r'}}\,dV'. \end{aligned} \tag{2.33}$$

Using the following vector identity

$$\int_V u\nabla\phi\,dV' = \int_S u\phi\,d\sigma - \int_V \phi\nabla u\,dV', \tag{2.34}$$

the fact that the surface integration may be moved beyond the limits of the volume V, and

$$\nabla e^{j\mathbf{k_r}\cdot\mathbf{r}} = j\mathbf{k_r}e^{j\mathbf{k_r}\cdot\mathbf{r}}, \tag{2.35}$$

the second term of Equation 2.33 can be rewritten as

$$-E_o j\mathbf{k_r}\int_V \hat{\mathbf{p}}\cdot\nabla n_1(\mathbf{r'})e^{-j(\mathbf{k_t}-\mathbf{k_r}\cdot\mathbf{r'})}\,dV'. \tag{2.36}$$

The term in Equation 2.36 is a longitudinal component and we will neglect it because it does not contribute to the power flow.

Thus, the expression for the relevant scattered electric field is

$$\mathbf{E_s}(r) = \frac{E_o k_o^2}{2\pi} \frac{e^{-jk_o r}}{r} \hat{\mathbf{p}} \int_V n_1(\mathbf{r'}) e^{-j(\mathbf{k_t}-\mathbf{k_r})\cdot\mathbf{r'}}\, dV'. \tag{2.37}$$

To simplify notation, lets assign

$$\phi_n(\mathbf{k}) = \int_V n_1(\mathbf{r'}) e^{-j\mathbf{k}\cdot\mathbf{r'}}\, dV' \tag{2.38}$$

thus

$$\mathbf{E_s}(r) = \frac{E_o k_o^2}{2\pi} \frac{e^{-jk_o r}}{r} \hat{\mathbf{p}} \phi_n(\mathbf{k_t} - \mathbf{k_r}). \tag{2.39}$$

Using Equation 2.16 we can now calculate the magnetic field as

$$\mathbf{H_s}(r) = -\frac{E_o k_o^2}{2\pi\eta_o j k_o} \phi_n(\mathbf{k_t} - \mathbf{k_r}) \nabla \times \left(\frac{e^{-jk_o r}}{r} \hat{\mathbf{p}} \right) \tag{2.40}$$

where $\eta_o = \sqrt{\frac{\mu_o}{\epsilon_o}}$ and is the characteristic impedance of free space. Here we are using the approximation $\eta_o \approx \eta$ which is valid because $\epsilon_o \approx \epsilon$.

Using the vector identity $\nabla \times \psi\mathbf{A} = \nabla\psi \times \mathbf{A} + \psi\nabla \times \mathbf{A}$ and noting that $\nabla \times \hat{\mathbf{p}} = 0$ yields

$$\mathbf{H_s}(r) = -\frac{E_o}{2\pi\eta_o j} \phi_n(\mathbf{k_t} - \mathbf{k_r}) \left(\frac{-jk_o e^{-jk_o r}}{r} + \frac{e^{-jk_o r}}{r^2} \right) (\mathbf{k_r} \times \hat{\mathbf{p}}). \tag{2.41}$$

Eliminating the small term in the far field yields

$$\mathbf{H_s}(r) = \frac{E_o k_o}{2\pi\eta_o} \phi_n(\mathbf{k_t} - \mathbf{k_r}) \left(\frac{e^{-jk_o r}}{r} \right) (\mathbf{k_r} \times \hat{\mathbf{p}}). \tag{2.42}$$

Poynting's theorem may now be used to calculate the time averaged power density of the radar backscatter

$$|\mathbf{S_s}| = \frac{1}{2} \left| \Re(\mathbf{E_s} \times \mathbf{H_s^*}) \right|. \tag{2.43}$$

Substituting Equations 2.39 and 2.42) into Equation 2.43 yields

$$|\mathbf{S_s}(\mathbf{k_o})| = \frac{E_o^2 k_o^3}{8\pi^2 \eta_o r^2} |\phi(\mathbf{k_t} - \mathbf{k_r})|^2 \left| (\hat{\mathbf{p}} \times (\mathbf{k_r} \times \hat{\mathbf{p}})) \right|. \tag{2.44}$$

Using the vector identity $\mathbf{A} \times (\mathbf{B} \times \mathbf{C}) = \mathbf{B}(\mathbf{A} \cdot \mathbf{C}) - \mathbf{C}(\mathbf{A} \cdot \mathbf{B})$ and the fact that $\mathbf{k_t}$ and $\hat{\mathbf{p}}$ are orthogonal for power transfer

$$|\mathbf{S_s}(\mathbf{k_o})| = \frac{E_o^2 k_o^4}{8\pi^2 \eta_o r^2} |\phi(\mathbf{k_t} - \mathbf{k_r})|^2. \tag{2.45}$$

The intensity of the incident wave may be similarly calculated as

$$|\mathbf{S_i}| = \frac{E_o^2}{2\eta_o}. \tag{2.46}$$

The bistatic Bragg RCS as a function of the incident radiation wave vector $\mathbf{k_t}$ and receiver wave vector $\mathbf{k_r}$ is thus determined by

$$\sigma(\frac{\mathbf{k_t} - \mathbf{k_r}}{2}) = 4\pi r^2 \frac{|\mathbf{S_s}(\mathbf{k_t} - \mathbf{k_r})|}{|\mathbf{S_i}|} = \frac{k_o^4}{\pi} |\phi(\mathbf{k_t} - \mathbf{k_r})|^2 \tag{2.47}$$

which is the Booker-Gordon formula.

For the more common case of a monostatic radar system, Equation 2.47 reduces to

$$\sigma(\mathbf{k_t}) = \frac{k_o^4}{\pi}|\phi(2\mathbf{k_t})|^2. \tag{2.48}$$

Chapter 3

Coherent Bragg Scatter Via Laminar Mixing Mechanism and Simulation Overview

As was explained in Chapter 2, the previous work used to calculate RCS was based on a turbulent closure assumption with which recent literature does not agree. Using a low turbulence closure assumption that is more consistent with the wake vortex, a new mixing mechanism is shown to exist. To quantify the RCS for this mechanism, it is necessary to use the more general relationship derived in Section 2.4. The end result of this derivation is Equation 2.48 which is the relationship between refractive index field and RCS. Note that this relationship is valid regardless of the source of the mixing.

As will be shown, it is not feasible to simulate the full Navier-Stokes equations as the TASS model does because structure on the order of the radar wavelength must be resolved. Instead, it can be shown that to good approximation, it is only necessary to simulate the

advection and diffusion of a single passive conservative to determine RCS. This results in a much faster, less memory intensive simulation.

Another benefit of a passive conservative simulation is the ability to generalize results to other situations. As will be shown, the simulation results are independent of atmospheric conditions. This means that a single simulation of an aircraft will give nearly precise results for any atmosphere. In addition, the results for a simulated aircraft can be generalized to any other aircraft with varying degrees of approximation. Thus, a good feature of the passive conservative simulation is the ability for one computationally expensive simulation run to be generalized to various aircraft and various atmospheric conditions.

The Wake Vortex - Passive Conservative Simulation (WV-PCS) is developed to determine a very good approximation of the refractive index field that causes RCS.

3.1 RCS Derivation From Passive Conservative Simulation

The relationship between refractive index and atmospheric parameters is [Tartarski, 1971]

$$n(\mathbf{r}) = 1 + 10^{-6}\left(\frac{79}{t(\mathbf{r})}\right)\left(p(\mathbf{r}) + \frac{7780p(\mathbf{r})q(\mathbf{r})}{t(\mathbf{r})}\right) \tag{3.1}$$

where $t(\mathbf{r})$, $p(\mathbf{r})$, and $q(\mathbf{r})$ are the absolute temperature (K), pressure (mb), and water vapor content (g/kg) respectively.

The most straightforward approach would be to utilize an LES model such as TASS, incorporate the correct near zero turbulence assumptions, and use the outputted values of $t(\mathbf{r})$, $p(\mathbf{r})$, and $q(\mathbf{r})$ to determine the refractive index field, $n(\mathbf{r})$, using Equation 3.1.

The problem to this approach is that the simulation must be capable of resolving the scales that are on the order of the smallest wavelengths of interest. In this case, it is not feasible for an LES model such as TASS to be able to determine RCS at microwave frequencies because the execution time would be too great. Spatial resolution of approximately 2 cm is necessary to calculate RCS at S-Band. The execution time for the TASS model for a 1 m grid spacing is 15 minutes on a Cray C-90 supercomputer. The execution time for an LES model that has a grid spacing of 2 cm (50 times greater resolution) would be greater by a factor of 50^2 for the increase in number of grid points multiplied by an additional factor of 50 corresponding to a finer time step necessary to satisfy the Courant condition. This would correspond to approximately 3.5 years for a similar simulation.

The advection of a passive conservative is much less computationally expensive. Not only are there less variables necessary to compute during each iteration, but a different stability

condition allows much larger time steps by a factor of v_{sound}/v_{wv} where v_{sound} is the velocity of sound and v_{wv} is the maximum velocity in the wake vortex system. This factor alone accounts for a faster execution time by a factor of approximately 100 for a typical aircraft. An additional factor of approximately 5 in execution time exists because of the fewer variables. Thus, an increase of approximately 500 results from the passive conservative approach thus making the simulation feasible.

3.1.1 Potential Temperature

It is useful to recast Equation 3.1 into a form including potential temperature instead of temperature.

Potential temperature, unlike temperature, may be treated as a passive conservative. (Note that although potential temperature is not passive in that it does contribute to the velocity field, its effect is shown to be small and it is treated as "passive" in this simulation.) As a parcel of air changes altitude, it undergoes adiabatic expansion and changes temperature, however, potential temperature remains unchanged. Potential temperature is related to temperature by

$$\theta = T\left(\frac{p_o}{p}\right)^{\alpha} \tag{3.2}$$

where $\alpha = 0.286$ for air.

Substituting Equation 3.2 into Equation 3.1 yields the form of the relationship using potential temperature

$$n(\mathbf{r}) = 1 + 10^{-6}\left(\frac{p(\mathbf{r})}{p_o}\right)^{\alpha}\left(\frac{79}{\theta(\mathbf{r})}\right)\left(p(\mathbf{r}) + \left(\frac{p(\mathbf{r})}{p_o}\right)^{\alpha}\frac{7780p(\mathbf{r})q(\mathbf{r})}{\theta(\mathbf{r})}\right). \tag{3.3}$$

3.1.2 First Order Approximation

The next step in finding the relationship between RCS and a passive conservative is to use a Taylor series expansion of Equation 3.3 and keep only the first order terms. This approximation is accurate because the percentage deviation of the atmospheric parameters is very small. The result is

$$n(\mathbf{r}) \approx n_o + (p(\mathbf{r}) - p_o)\frac{\partial n}{\partial p}|_{n=n_o} + (\theta(\mathbf{r}) - \theta_o)\frac{\partial n}{\partial \theta}|_{n=n_o} + (q(\mathbf{r}) - q_o)\frac{\partial n}{\partial q}|_{n=n_o} \tag{3.4}$$

and the notation $n = n_o$ represents the full condition where $p = p_o$, $\theta = \theta_o$, and $q = q_o$.

Evaluating the derivatives in Equation 3.4 yields

$$\frac{\partial n}{\partial p} = 10^{-6}\left(\frac{p(\mathbf{r})}{p_o}\right)^{\alpha}\left(\frac{79}{\theta(\mathbf{r})}\right)\left((1+\alpha) + (1+2\alpha)\left(\frac{p(\mathbf{r})}{p_o}\right)^{\alpha}\frac{7780q(\mathbf{r})}{\theta(\mathbf{r})}\right) \tag{3.5}$$

$$\frac{\partial n}{\partial \theta} = 10^{-6}\left(\frac{p(\mathbf{r})}{p_o}\right)^{\alpha}79\left(-\frac{p(\mathbf{r})}{\theta(\mathbf{r})^2} - \left(\frac{p(\mathbf{r})}{p_o}\right)^{\alpha}\frac{2(7780)p(\mathbf{r})q(\mathbf{r})}{\theta(\mathbf{r})^3}\right) \tag{3.6}$$

$$\frac{\partial n}{\partial q} = 10^{-6}\left(\frac{p(\mathbf{r})}{p_o}\right)^{2\alpha}79(7780)\frac{p(\mathbf{r})}{\theta(\mathbf{r})^2}. \tag{3.7}$$

Substituting the nominal values of pressure and temperature of $p_o = 1000$ mb and $\theta_o = 300$ K in Equations 3.5 to 3.7 yields

$$\frac{\partial n}{\partial p}|_{n=n_o} = 10^{-6}(0.34 + 10.7q_o) \tag{3.8}$$

$$\frac{\partial n}{\partial \theta}|_{n=n_o} = 10^{-6}(0.878 + 45.5q_o) \tag{3.9}$$

$$\frac{\partial n}{\partial q}|_{n=n_o} = 10^{-6}(6830) \tag{3.10}$$

3.1.3 Zero Pressure Gradient Approximation

It can be argued that the first term in Equation 3.4 does not contribute to RCS. Pressure equalizes itself very quickly to the surrounding atmosphere via acoustical processes so it is not stretched into smaller scales over time. Since pressure deviation remains at large scales, it provides no RCS because pressure deviation scales do not exist at scales of the order of magnitude of the electromagnetic radiation.

The variable n' disregards the pressure perturbation term and results in the same RCS

$$n' = 10^{-6}[(0.878 + 45.5q_o)(\theta - \theta_o) + (6830)(q - q_o)]. \tag{3.11}$$

3.1.4 Generalize Passive Conservative

We now introduce the generalized linearly stratified passive conservative, $s(\mathbf{r}, t)$, which is governed by the advection and diffusion of the velocity field of the wake vortex. The passive conservative field combines the effects of RCS generated from both the water vapor content and potential temperature stratification. Let $s(\mathbf{r}, t)$ be the unique solution to the equation

$$\frac{\partial s}{\partial t} + u_j \frac{\partial s}{\partial x_j} - D \frac{\partial^2 s}{\partial x_j^2} = 0 \tag{3.12}$$

with initial conditions of

$$s(y\hat{\mathbf{y}}, 0) = y_o - y \tag{3.13}$$

which indicates a stratification of unitary negative slope and $\hat{\mathbf{y}}$ is the unit vector in the vertical direction.

We will now show that the water vapor concentration field, $q(\mathbf{r}, t)$, can be expressed in terms of the generalized passive conservative, $s(\mathbf{r}, t)$, as

$$q(\mathbf{r}, t) = -m_q s(\mathbf{r}, t) + q_o \tag{3.14}$$

where m_q is the slope of the stratified water vapor concentration field.

Combining Equation 3.14 into Equation 3.12 yields

$$\frac{\partial q}{\partial t} + u_j \frac{\partial q}{\partial x_j} - D \frac{\partial^2 q}{\partial x_j^2} = 0 \tag{3.15}$$

which is the valid equation describing advection and diffusion of water vapor.

Furthermore, substituting Equation 3.13 into Equation 3.14 yields

$$q(y\hat{\mathbf{y}}, 0) = m_q(y - y_o) + q_o \tag{3.16}$$

which is the correct initial condition of the stratified atmosphere. Since $q(\mathbf{r}, t)$ satisfies both the correct partial differential equation and the initial conditions, Equation 3.14 is the unique equation describing the water vapor field.

Similarly letting

$$\theta(\mathbf{r}, t) = -m_\theta s(\mathbf{r}, t) + \theta_o \tag{3.17}$$

and combining with Equation 3.12 yields

$$\frac{\partial \theta}{\partial t} + u_j \frac{\partial \theta}{\partial x_j} - \frac{k}{\rho c_p} \frac{\partial^2 \theta}{\partial x_j^2} = 0 \tag{3.18}$$

where $\frac{k}{\rho c_p}$ has been substituted for D because they have approximately the same value for air. Equation 3.18 is the equation describing the evolution of the potential temperature field.

Furthermore, substituting the initial condition of $s(\mathbf{r}, t)$ in Equation 3.13 into Equation 3.17 yields

$$\theta(y\hat{\mathbf{y}}, 0) = m_\theta (y - y_o) + \theta_o \tag{3.19}$$

which is the initial condition of the stratified atmosphere. Thus, Equation 3.17 is the unique equation describing the potential temperature field.

Substituting Equation 3.14 and 3.17 into Equation 3.11 yields

$$n(\mathbf{r}, t)' = 10^{-6}[(0.878 + 45.5 q_o) m_\theta s(\mathbf{r}, t) + (6830) m_q s(\mathbf{r}, t)]. \tag{3.20}$$

We may now decompose the modified refractive index, $n'(\mathbf{r}, t)$, into an atmospheric parameter A and the generalized linearly stratified passive conservative, $s(\mathbf{r}, t)$, as

$$n(\mathbf{r}, t)' = \sqrt{A} s(\mathbf{r}, t) \tag{3.21}$$

where

$$\sqrt{A} = 10^{-6} \left[(0.878 + 45.5 q_o) m_\theta + (6830) m_q \right]. \tag{3.22}$$

3.1.5 Determination of RCS

We may now determine the RCS of the wake vortex system from the generalized passive conservative. Substituting Equation 3.21 into Equation 2.48 yields

$$\sigma(\mathbf{k_t}, t) = A \frac{k_o^4}{\pi} |\phi_s(2\mathbf{k_t}, t)|^2 \tag{3.23}$$

where the direction of the radian wave number $\mathbf{k_t}$ is the radar radial direction and magnitude $k_o = |\mathbf{k_t}|$ is related to the radar wavelength λ through $k_o = 2\pi\lambda^{-1}$. $\phi_s(k)$ is the obtained by taking the Fourier transform of the aircraft dependent term, $s(\mathbf{r}, t)$, at half the operating radar wavelength as

$$\phi_s(2\mathbf{k_t}, t) = \int s(\mathbf{r}, t) e^{-j2\mathbf{k_t}\cdot\mathbf{r}} \, d\mathbf{r} \tag{3.24}$$

and is computed by performing a numerical integration over the passive conservative field.

To accurately determine $\phi_s(2\mathbf{k_t}, t)$, the resolution of the simulation must satisfy the Nyquist criteria

$$\Delta l < \frac{\pi}{2k} \tag{3.25}$$

where Δl is the grid spacing (see Section 4.5). For example, with the highest resolution grid spacing of 2 cm that is used in the C5-A simulation, RCS for up to 3.75 GHz may be determined. To determine RCS at higher frequencies, the simulation time increases as the cube of the frequency.

3.2 WV-PCS Assumptions and Justifications

3.2.1 Crow Instability

Because the simulation uses a deterministic velocity field, non-linear effects such as the long wavelength instabilities are not considered. Recent simulations [Lewellen and Lewellen, 1996] have indicated that the time scales for these instabilities to develop are on the order of minutes and they do not cascade down to small eddies. Thus, although the long wavelength instabilities change the velocity field and cause error in the simulation, there is a substantial period of time where the long wavelength instabilities are negligible and this represents the window of accuracy for the simulation.

Figure 3.1 is the result of a 3-D LES simulation [Lewellen and Lewellen, 1996]. The grey scales correspond to the concentration of a passive conservative or "tracer". Notice that the time scales in the figure is on the order of minutes and the turbulence does not cascade down to small eddies. This would indicate that the turbulence has a negligible effect on RCS because only eddies that are on the order of the operating radar wavelength are important for RCS. At 3 GHz, for example, the eddies that contribute to RCS would be

5 cm in dimension. The resolution of the simulation shown in Figure 3.1 is 1 meter and there do not seem to be eddies at even this size scale.

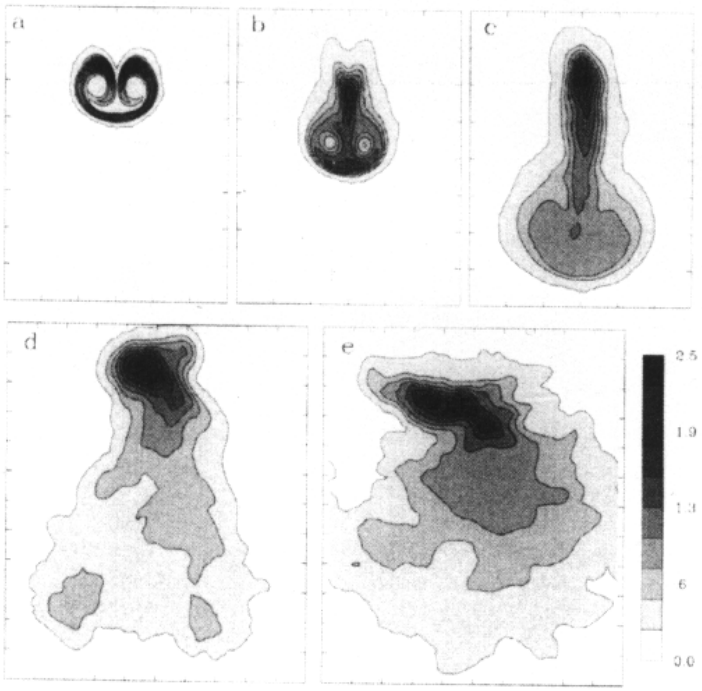

Figure 3.1: Evolution of the downstream average of the tracer concentrations for the ER-2 wake at 15 s, 30 s, 62 s, and 325 s [Lewellen and Lewellen, 1996]

3.2.2 Pre-Rollup Homogenization

Turbulence exists in the wake vortex system close behind the aircraft [Devenport et al., 1996] which causes a homogenization to some degree. The initial stratification is mixed by this turbulence. Since the WV-PCS does not model the pre-rollup homogenization, the exact effect of this phenomenon is not known and will require further study.

3.2.3 No Turbulence Assumption

Recent work has indicated that the far-field evolution of the wake vortex system is dominated by viscous effects and not by turbulence. Previous work has utilized a Reynold's stress closure (RSC) model to quantify RCS generated by turbulent mixing [Marshall et al., 1996]. This work expands upon that work in that turbulence is not cited as the dominant cause of mixing in a wake vortex system. This is consistent with recent literature that states that RSC models yield unacceptably high turbulence intensities [Zeman, 1995].

Other studies have been performed that have concluded that unless there is unrealistically high axial flow, the wake vortex is a stabilizing structure that tends to damp out initial disturbances that would cause unstable growth for other structures such as unstable jets [Ragab, 1995].

Recent literature indicates that after these initial levels of turbulence at roll-up, turbulent breakdown of the wake vortex occurs over a relatively large period of time and does not necessarily cascade all the way down the the Kolmogorov microscale where viscous dissipation dominates [Lewellen and Lewellen, 1996]. Unless there is unrealistically high axial flow, the wake vortex is a stabilizing structure that tends to damp out initial disturbances that would cause unstable growth for other structures such as unstable jets [Ragab, 1995].

Furthermore, there is a large body of literature that is in agreement with the fact that the wake vortices are predominantly laminar especially in and around the core [Newman, 1959, Batchelor, 1964, McCormick, 1968, Saffman, 1973, Mayer and Powell, 1992]. In addition, the length of time that the wake vortex system persists gives indication that decay levels are low and are more consistent with the viscous decay of a laminar wake rather than the inviscid decay of a turbulent wake vortex.

3.2.4 Constant Descent Rate

An important assumption used in the WV-PCS is a constant descent rate of the wake vortex system. Figure 3.2 shows the altitude as simulated by the TASS model and as experimentally measured using a LIDAR system [Proctor, 1996]. The results indicate a relatively constant descent rate until the wake vortex system approaches approximately 50 m from the ground. Thus, the window of accuracy of the constant descent rate assumption is reasonable until the wake vortex system nears the ground.

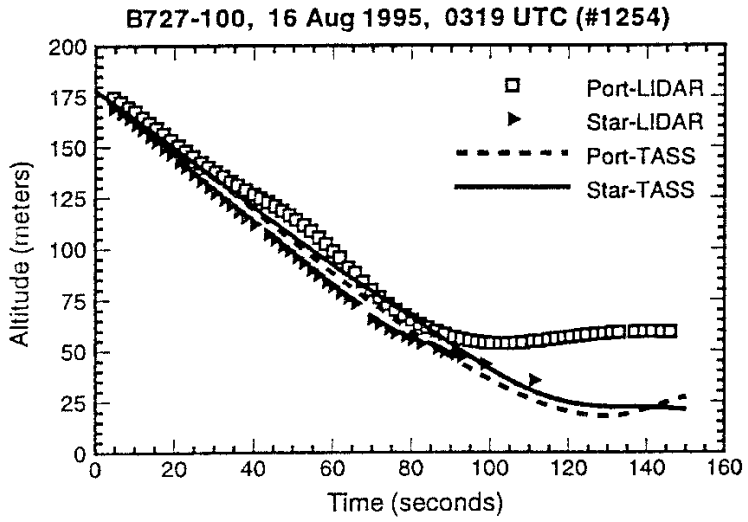

Figure 3.2: Descent of Wake Vortex System [Proctor, 1996]

3.3 Extension to Other Aircraft

Since parametric studies are computationally expensive due to the large amount of CPU time per simulation, it is useful to extrapolate a single simulation to a wide variety of aircraft.

As has been mentioned earlier, the equation describing the advection and diffusion of the generalized passive conservative is

$$\frac{\partial s}{\partial t} + u_j \frac{\partial s}{\partial x_j} - D\frac{\partial^2 s}{\partial x_j^2} = 0 \tag{3.26}$$

with an initial condition of

$$s(y\hat{\mathbf{y}}, 0) = m_q y. \tag{3.27}$$

Using Equations 4.13 and 4.19, it can be shown that the form of the wake vortex velocity field for an elliptically loaded aircraft of arbitrary mass, wingspan, and velocity is

$$u_j(\mathbf{r}, t) = \left(\frac{B_{C5}}{B}\right)^2 \left(\frac{M}{M_{C5}}\right) \left(\frac{v_{C5}}{v}\right) u_{j,C5}\left(\left[\frac{B_{C5}}{B}\right]\mathbf{r}, \left[\left(\frac{B_{C5}}{B}\right)^2 \left(\frac{M}{M_{C5}}\right) \left(\frac{v_{C5}}{v}\right)\right] t\right) \tag{3.28}$$

where M_{C5}, B_{C5}, and v_{C5} is the mass, wingspan, and aircraft velocity respectively of the C5-A, M, B,and v is the mass, wingspan, and aircraft velocity of an arbitrary aircraft, and $u_{j,C5}$ is the wake vortex velocity field for the C5-A.

Consider the following approximation of the aircraft generalized passive conservative as a function of position and time

$$s(\mathbf{r}, t) = \left(\frac{r}{r'}\right) s_{C5}\left(\mathbf{r}', t'\right) \tag{3.29}$$

where

$$\mathbf{r}' = \frac{B_{C5}}{B}\mathbf{r}, \tag{3.30}$$

$$t' = \left(\frac{B_{C5}}{B}\right)^3 \left(\frac{M}{M_{C5}}\right) \left(\frac{v}{v_{C5}}\right) t, \tag{3.31}$$

and $s_{C5}(\mathbf{r}', t')$ is the passive conservative distribution for the C5-A which has been determined through computationally expensive simulation.

To demonstrate the validity of this approximation, it is necessary to show that it satisfies an approximate differential equation and satisfies the initial conditions. First, we may demonstrate that the aircraft generalized passive conservative distribution, $s(\mathbf{r}, t)$, satisfies the advection and diffusion equation.

Beginning with the advection and the diffusion equation for the C5-A

$$\frac{\partial s_{C5}}{\partial t} = -u_{j,C5} \frac{\partial s_{C5}}{\partial x_j} + D \frac{\partial^2 s_{C5}}{\partial {x_j}^2} \tag{3.32}$$

substituting the value of s in Equation 3.29 into Equation 3.32 and using the chain rule yields

$$\frac{\partial s}{\partial t} = -u_j \frac{\partial s}{\partial x_j} + \left(\frac{B_{C5}}{B}\right) \left(\frac{M}{M_{C5}}\right) \left(\frac{v_{C5}}{v}\right) D \frac{\partial^2 s}{\partial {x_j}^2}. \tag{3.33}$$

Note that this is an approximation in that the diffusion term is multiplied by the term $\left(\frac{B_{C5}}{B}\right) \left(\frac{M}{M_{C5}}\right) \left(\frac{v_{C5}}{v}\right)$. The effect of this will be discussed later.

Next we may demonstrate that the initial conditions are satisfied by substituting Equation 3.27 into Equation 3.29

$$s(y\hat{\mathbf{y}}, 0) = \left(\frac{r}{r'}\right) s_{C5}\left(\mathbf{r}', 0\right) = \left(\frac{r}{r'}\right) \left(\frac{r'}{r}\right) (y_o - y) = y_o - y \tag{3.34}$$

Next, we may determine that quantity $\phi_s(2\mathbf{k_t}, t)$ for an aircraft of arbitrary dimensions. Repeating the relationship

$$\phi_s(2\mathbf{k_t}, t) = \int s(\mathbf{r}, t) e^{-j2\mathbf{k_t}\cdot\mathbf{r}}\, d\mathbf{r} \tag{3.35}$$

and substituting Equation 3.29

$$\phi_s(2\mathbf{k_t}, t) = \left(\frac{r}{r'}\right) \int s_{C5}\left(\mathbf{r}', t'\right) e^{-j2\mathbf{k}'_\mathbf{t}\cdot\mathbf{r}'} \left(\frac{r}{r'}\right)^2 d\mathbf{r}' = \left(\frac{r}{r'}\right)^3 \phi_{s,C5}(2\mathbf{k}'_\mathbf{t}, t) \tag{3.36}$$

where the integration variable has been changed from $\mathbf{r}$ to $\mathbf{r}'$, and

$$\mathbf{k}'_\mathbf{t} = \frac{B}{B_{C5}}\mathbf{k_t}. \tag{3.37}$$

Substituting into the relationship to determine cross section

$$\sigma(\mathbf{k_t}, t) = \frac{k^4}{\pi}|\phi_s(2\mathbf{k_t}, t)|^2 \tag{3.38}$$

yields

$$\sigma(\mathbf{k_t}, t) = \left(\frac{r}{r'}\right)^6 \left(\frac{k}{k'}\right)^4 \left(\frac{k'^4}{\pi}\right) |\phi_{s,C5}(\mathbf{2k}'_\mathbf{t}, t')|^2. \tag{3.39}$$

Finally, using Equations 3.30 and 3.37 yields

$$\sigma(\mathbf{k_t}, t) = \left(\frac{B}{B_{C5}}\right)^2 \sigma_{C5}(\mathbf{k}'_\mathbf{t}, t'). \tag{3.40}$$

As was shown in Equation 3.33, the implicit diffusion term used is different from the physical constant for an aircraft other than the C-5A at the particular velocity assumed. Section 5.5 explores this deviation with actual simulation results.

Chapter 4

Wake Vortex - Passive Conservative Simulation (WV-PCS)

To determine the Bragg scatter RCS from the water vapor distribution, it is necessary to simulate the flow of a passive conservative due to the velocity field of the wake vortex system. The simulation of the stratified passive conservative flow due to the wake vortex is performed using a two-dimensional finite difference numerical simulation. The water vapor is modeled as a passive conservative that is advected by the velocity field [Hatliner and Williams, 1980]. In addition, thermal diffusion causes a flow across concentration gradients.

The simulation is computationally intensive because the smallest spirals must be resolvable by the simulation grid. For the C5-A simulation performed, one minute of actual wake vortex evolution takes 84 hours of computation time on a Silicon Graphics Power Challenge.

4.1 Finite Difference Formulation

4.1.1 Equation Set

The simulation of the mechanics of the wake vortex is performed using a two-dimensional finite difference method. Equation 4.1 is the equation that describes the time evolution of the generalized passive conservative [Schmidt et al., 1984]

$$\frac{\partial s}{\partial t} + u_j \frac{\partial s}{\partial x_j} - D\frac{\partial^2 s}{\partial x_j^2} = 0 \tag{4.1}$$

where u_1, and u_2 are the two components of velocity in the x_1, and x_2 directions, s is the generalized passive conservative, and $D = .242 s/cm^2$ is the diffusion coefficient for a air/water vapor system with large excess of air [Lide and Fredericks, 1997].

The velocity field is assumed a priori (see Section 4.5), so s is the variable that describes the state of the system.

4.1.2 Finite Difference Formulation

Equation 4.1 is a mixed partial differential equation [Lapidus and Pinder, 1982]. The first term $u_j \frac{\partial s}{\partial x_j}$ is the advection term and is a component of a hyperbolic PDE. The second term $D\frac{\partial^2 s}{\partial x_j^2}$ is the diffusion term and is a component of a parabolic PDE.

The following set of coupled difference equations were used:

$$s_{i,j}^n = r_{i,j}^{n-1} - 2\Delta t_s \left(u_1 \left(\frac{s_{i+1,j}^{n-1} - s_{i-1,j}^{n-1}}{2\Delta l_x} \right) + u_2 \left(\frac{s_{i,j+1}^{n-1} - s_{i,j-1}^{n-1}}{2\Delta l_y} \right) \right) \tag{4.2}$$

$$r_{i,j}^{n} = s_{i,j}^{n-1} + 2\Delta t_s D \left(\frac{s_{i+1,j}^{n-1} + s_{i-1,j}^{n-1} - 2s_{i,j}^{n-1}}{{\Delta l_x}^2} + \frac{s_{i,j+1}^{n-1} + s_{i,j-1}^{n-1} - 2s_{i,j}^{n-1}}{{\Delta l_y}^2} \right). \tag{4.3}$$

where $r_{i,j}$ is an intermediate variable coupled to the passive conservative $s_{i,j}$.

To verify that these are accurate and stable equations, it is instructive to examine the advective and diffusive limits of this finite differencing scheme.

In the advective limit where $D = 0$ this system of coupled equations reduces to

$$s_{i,j}^{n} = s_{i,j}^{n-2} - 2\Delta t_s \left(u_1 \left(\frac{s_{i+1,j}^{n-1} - s_{i-1,j}^{n-1}}{2\Delta l_x} \right) + u_2 \left(\frac{s_{i,j+1}^{n-1} - s_{i,j-1}^{n-1}}{2\Delta l_y} \right) \right). \tag{4.4}$$

This is the form of the leapfrog differencing scheme with centered spatial derivatives. This scheme is conditionally stable subject to the Courant condition (see Section 4.7) and has the advantage of second order accuracy.

In the diffusive limit where $u_i = 0$ this system of coupled equations reduces to

$$s_{i,j}^{n} sq_{i,j}^{n-2} + 2\Delta t_s D \left(\frac{s_{i+1,j}^{n-2} + s_{i-1,j}^{n-2} - 2s_{i,j}^{n-2}}{{\Delta l_x}^2} + \frac{s_{i,j+1}^{n-2} + s_{i,j-1}^{n-2} - 2s_{i,j}^{n-2}}{{\Delta l_y}^2} \right). \tag{4.5}$$

This is the form for forward time centered space (FTCS) with time step of $2\Delta t_s$ and is stable for the diffusive PDE.

4.2 Boundary Conditions

The boundary conditions are periodic in all directions with a bias in the vertical y-direction to account for stratification. The periodic boundary conditions are implemented when

calculating the spatial derivatives by the following relations

$$s_{N_x+1,j} = s_{1,j}, \qquad s_{0,j} = s_{N_x,j} \tag{4.6}$$

$$s_{i,N_y+1} = s_{i,1} + \Delta s, \qquad s_{i,0} = s_{i,N_y} - \Delta s \tag{4.7}$$

where N_x and N_y are the number of points in the x and y directions respectively. The bias term Δs is the difference between the average value of the variable s at the top and bottom of the system where

$$\Delta s = < s_{i,N_y+1} > - < s_{i,1} > \tag{4.8}$$

and has the desirable effect of allowing diffusion and advection through the boundary yet maintains stability in the average values of the stratified variables. The same boundary conditions are used on the coupled variable $r_{i,j}$.

4.3 Grid Spacing

A fine uniform grid spacing is used over the core of the wake vortices. Outside of the core, the grid size is described by an exponential function of the indices. The grid is designed for fine resolution where the passive conservative spirals are on the smallest scale and progressively courser resolution as the scale of the spirals increase. This scheme results in a minimum number of gridpoints while achieving the necessary resolution.

The spacing in the x direction for the left side of the grid ($x < 0$) is described by

$$\begin{aligned} \Delta l_x(i,j) &= \Delta l_{x_o} r^{B_{ox}-i} & i < B_{ox} \\ &= \Delta l_{x_o} & B_{ox} \leq i \leq B_{fx} \\ &= \Delta l_{x_o} r^{i-B_{fx}} & B_{fx} < i < N_x/2 \end{aligned} \tag{4.9}$$

where r is a constant slightly larger than unity used to determine how rapidly the grid stretches with distance, B_{ox} and B_{fx} are the respective upper and lower bounding x indices of the uniform center portion of the system, and Δl_{x_o} is the uniform x grid spacing at the center of the system. This grid spacing scheme allows for a smooth transition from the closely spaced center to the more coarse outer edges. The x grid spacing for the right side ($x > 0$) is the mirror image of the left side

$$\Delta l_x(i - N_x/2, j) = \Delta l_x(i,j). \tag{4.10}$$

The spacing in the y direction is described by

$$\begin{aligned} \Delta l_y(i,j) &= \Delta l_{y_o} r^{B_{oy}-j} & j < B_{oy} \\ &= \Delta l_{y_o} & B_{oy} \leq j \leq B_{fy} \\ &= \Delta l_{y_o} r^{j-B_{fy}} & B_{fy} < j < N_y. \end{aligned} \tag{4.11}$$

Table 4.1 lists the values of the parameters describing the computational mesh for the C5-A and 747 simulation. The same grid parameters could be used for both simulations because the two aircraft have the same wingspan.

Figure 4.1 shows the resultant mesh of the entire system for the C5-A and 747 simulation. The system is large enough such that the wake vortex velocity is very close to zero at the

Table 4.1: Grid Parameters for C5-A and 747

Quantity	Value
l_{xo}	0.02 m
l_{yo}	0.02 m
N_x	1764
N_y	1007
S_{xo}	293
S_{yo}	303
S_{xf}	694
S_{yf}	704
r_x	1.0155
r_y	1.0155

edges. This is necessary for using periodic boundary conditions. Figure 4.2 shows the small uniform grid over the left vortex core. In Figures 4.1 and 4.2, the mesh is drawn every 16 simulation grid spacings so that the resolution of the simulation is 256 times finer than displayed.

4.4 Even-Odd Instability

The even-odd instability that occurs in time-centered finite difference is removed by placing an averaging step every M iterations [Press, 1986]:

$$f_{i,j,k}^{n-1} = \frac{f_{i,j,k}^{n} + f_{i,j,k}^{n-2}}{2} \tag{4.12}$$

This step is performed before calculating the spatial derivatives during the n_{th} iteration.

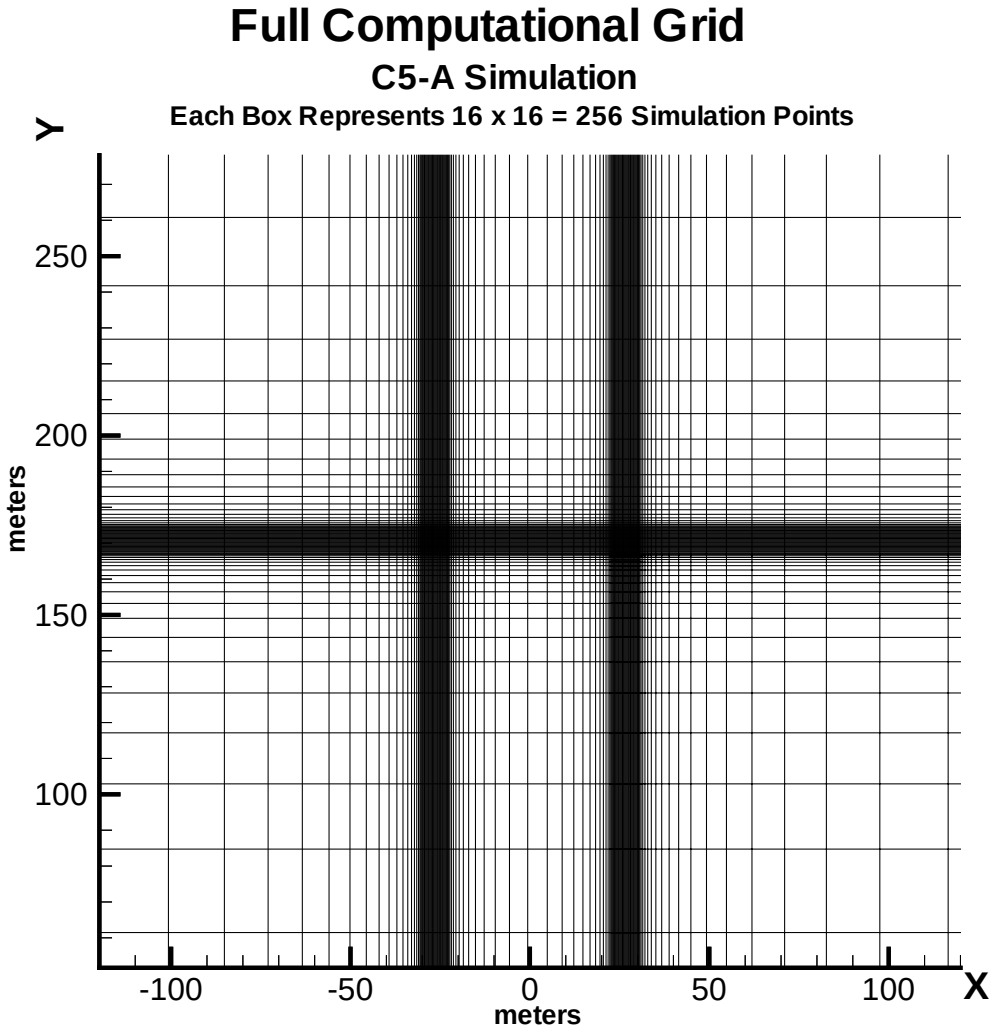

Figure 4.1: Full Computational Grid, C5-A and 747

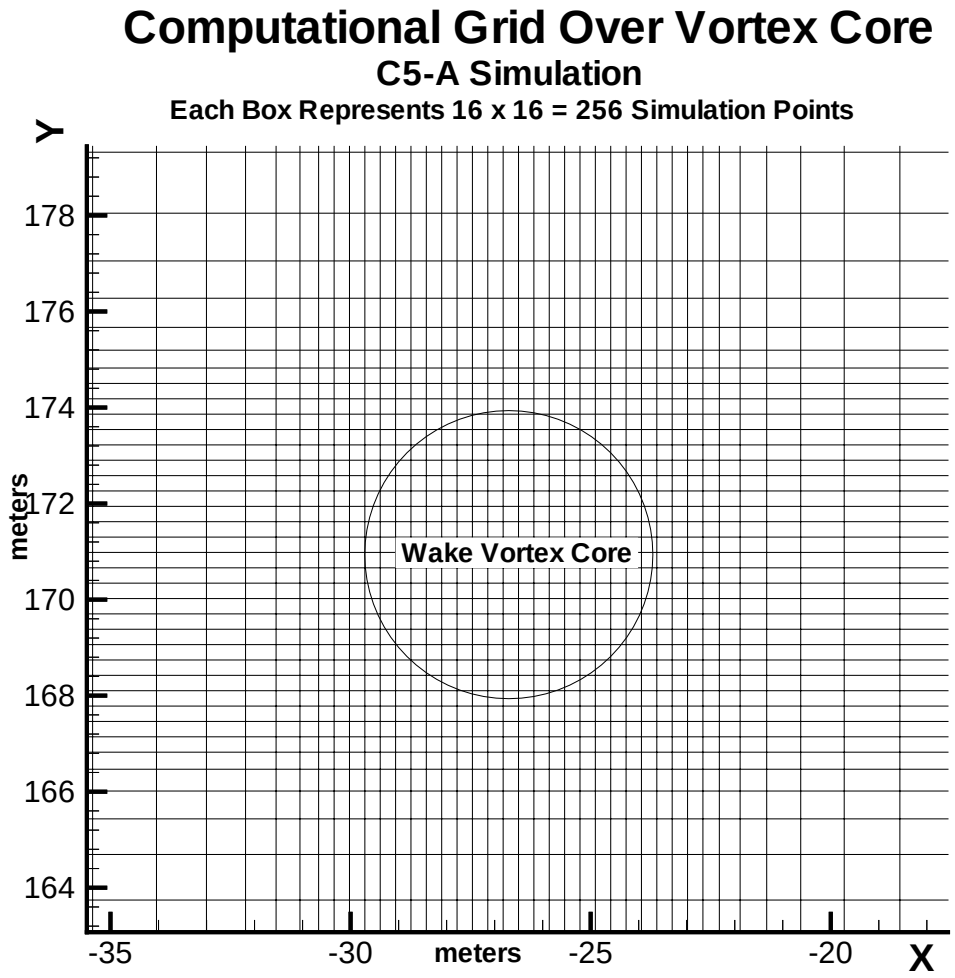

Figure 4.2: Computational Grid Over Vortex Core, C-5A and 747

4.5 Velocity Field

The initial velocity field was taken to be the superposition of two counter rotating vortices. The Burnham-Hallock model was used for each vortex [Burnham and Hallock, 1982] where the velocity of a single vortex is described by

$$\mathbf{v}_{vortex}(\mathbf{r}-\mathbf{r_o}(t)) = \frac{\Gamma_\infty}{2\pi}\frac{(|\mathbf{r}-\mathbf{r_o}(t)|)}{|\mathbf{r}-\mathbf{r_o}(t)|^2 + {r_c}^2}\hat{\theta}_\mathbf{o} \tag{4.13}$$

where $\mathbf{r}$ is the displacement vector from the axis of the wake vortex, r_c is the radius of the core, $\mathbf{r_0}(t)$ is the center of the vortex as a function of time, $\hat{\theta}_\mathbf{o}$ is the unit vector in the azimuthal direction of the vortex, and Γ_∞ is the circulation at $r >> r_c$. The counter rotating vortex system is thus described by

$$\mathbf{v}_{system}(\mathbf{r}) = \mathbf{v}_{vortex}(\mathbf{r}-\mathbf{r_2}(t)) - \mathbf{v}_{vortex}(\mathbf{r}-\mathbf{r_1}(t)) \tag{4.14}$$

where $\mathbf{r_2}(t) - \mathbf{r_1}(t)$ is the separation between the vortices.

The two vortices descend at the same rate which is the induced velocity of one vortex upon the other

$$v_d = \frac{\Gamma_\infty}{2\pi}\frac{d_s}{d_s^2 + {r_c}^2}. \tag{4.15}$$

The vortex centers are described by

$$\mathbf{r_1}(t) = \mathbf{r_{1o}} - v_d t\hat{\mathbf{y}} \tag{4.16}$$

$$\mathbf{r_2}(t) = \mathbf{r_{2o}} - v_d t\hat{\mathbf{y}} \tag{4.17}$$

where $\mathbf{r_{1o}}$ and $\mathbf{r_{2o}}$ are the initial centers of the vortices at rollup and $\hat{\mathbf{y}}$ is the unit vector in the positive y direction.

The vortex core radius r_c is taken to be 5% of the aircraft's wingspan [Proctor, 1996]. The vortex separation d_s and the circulation Γ_∞ can be determined using the assumption of an elliptically loaded wing [Karamcheti, 1980]

$$d_s = \frac{\pi}{4}B \tag{4.18}$$

$$\Gamma_\infty = \frac{4Mg}{\pi\rho V_a B} \tag{4.19}$$

where $\rho = 1.16\,\mathrm{kg/m^3}$ is the density of air at room temperature [Schmidt et al., 1984].

Tables 4.2 and 4.3 summarizes the simulation parameters used for the C5-A and 747 simulation.

4.6 Upwash Velocity

Since the wake vortex system descends through the atmosphere, it is desirable to add an upwash velocity to the grid. This eliminates the problem of the vortex system descending into the lower resolution portion of the grid. The upwash velocity is an offset that is added to the vertical velocity of each grid point. The vertical coordinate then undergoes the appropriate transformation.

Table 4.2: C-5A Simulation Parameters

Quantity	Value
mass M	250 Mg
wingspan B	68 m
air speed V_a	133 m/s
Γ_∞	297 m^2/s
maximum velocity v_{max}	6.56 m/s
separation distance d_s	53.41 m
core radius r_c	3.4 m
descent velocity v_d	0.832 m/s
minimum grid spacing Δl_o	0.02 m
time step Δt_s	0.0015 s

Table 4.3: 747 Simulation Parameters

Quantity	Value
mass M	350 Mg
wingspan B	68 m
air speed V_a	70 m/s
Γ_∞	790 m^2/s
maximum velocity v_{max}	17.45 m/s
separation distance d_s	9.425 m
core radius r_c	0.6 m
descent velocity v_d	2.213 m/s
minimum grid spacing Δl_o	0.002 m
time step Δt	0.0005 s

Before the differential equations are updated, an upwash velocity is added

$$v_{i,j}(t) = v'_{i,j}(t) + v_d \tag{4.20}$$

where the primed velocity corresponds to the velocity in the stationary frame of reference and the non-primed variables are those in the frame of reference of the system descending with a velocity of v_d. Note that it is the PDE in the non-primed system that is solved.

The following transformation is performed prior to output

$$y'_j(t) = y_j - v_d t. \tag{4.21}$$

$$v'_{i,j}(t) = v_{i,j}(t) - v_d \tag{4.22}$$

so that the quantities are in the desired stationary frame.

4.7 Courant Condition

The Courant condition must be considered for a stable simulation. This condition governs the maximum allowable size of the time step Δt_s. The passive conservative may not advect more than half a grid cell during the time step or instability results. A conservative Courant condition was used to determine a stable time step [Press, 1986]

$$\Delta t_s = \frac{1}{3}\frac{\Delta l}{|v|_{max}}. \tag{4.23}$$

where $|v|_{max}$ is the maximum velocity in the wake vortex system and Δl is the minimum

grid spacing of the computational mesh. The time steps are summarized in Tables 4.2 and 4.3.

4.8 WV-PCS Output

The WV-PCS consists of three distinct outputs:

- Output 1.The generalized conservative field $s(\mathbf{r}, t)$.
- Output 2.The function $\phi_s(2\mathbf{k_t}, t_i)$ for the complete wavenumber spectrum and for look angles of 0^o and 90^o at specific snapshots in time corresponding to t_i.
- Output 3.The function $\phi_s(2\mathbf{k_t}_i, n\Delta t_s)$ at every iteration at discrete wavenumbers that corresponds to VHF, UHF, L-Band, and S-Band radar frequencies and for the two look angles of 0^o and 90^o.

Output 1 is used to form grey scale contour plots that give a feel for the mixing mechanism. The contour plots are shown in Section 5.2.

Output 2 is used to form the RCS spectrum as a function of radar frequency at specific instances in time (Section 5.3) and is numerically approximated as

$$\phi_s(2\mathbf{k_t}, t_i) = \int s(\mathbf{r}, t_i) e^{-j2\mathbf{k_t}\cdot\mathbf{r}}\, d\mathbf{r} \approx \sum_{k=1}^{N_y}\sum_{j=1}^{N_x} s(\mathbf{r}_{jk}, t_i) e^{-j2\mathbf{k_t}\cdot\mathbf{r}_{jk}} \Delta l_x \Delta l_y \tag{4.24}$$

where $\mathbf{k_t} = 2\pi\lambda^{-1}\hat{\mathbf{x}} = \frac{\omega}{c}\hat{\mathbf{x}}$ for the 0^o look angle and $\mathbf{k_t} = 2\pi\lambda^{-1}\hat{\mathbf{y}} = \frac{\omega}{c}\hat{\mathbf{y}}$ for the 90^o look angle and $\mathbf{r}_{jk}$ is the position vector of the discrete computational grid points. The

Table 4.4: Wavelengths for Specific Frequency Bands

i	Band	Wavelength (λ)
1	VHF	1.90 m
2	UHF	0.709 m
3	L-Band	0.23 m
4	S-Band	0.1 m

variable ω is stepped through fine resolution increments such that the RCS as a function of frequency is computed.

Output 3 is useful for the detailed temporal evolution of RCS at specific frequencies of interest (Section 5.4). In addition, the doppler processor simulator (DPS) uses this data to determine the doppler behavior of the wake vortex system (Chapter 6). The quantity $\phi_s(\mathbf{k_t}_i, t)$ is numerically approximated during each iteration as

$$\phi_s(\mathbf{k_t}_i, n\Delta t_s) = \int s(\mathbf{r}, n\Delta t_s) e^{-j2\mathbf{k_t}_i \cdot \mathbf{r}}\, d\mathbf{r} \approx \sum_{k=1}^{N_y} \sum_{j=1}^{N_x} s(\mathbf{r}_{jk}, n\Delta t_s) e^{-j2\mathbf{k_t}_i \cdot \mathbf{r}_{jk}} \Delta l_x \Delta l_y \qquad (4.25)$$

where $\mathbf{k_t}_i = 2\pi\lambda_i^{-1}\hat{\mathbf{x}}$ for the 0^o look angle and $\mathbf{k_t}_i = 2\pi\lambda_i^{-1}\hat{\mathbf{y}}$ for the 90^o look angle and Δt_s is the simulation time step. λ_i are the radar wavelength of the specific bands whose values are given in Table 4.4.

Chapter 5

Radar Cross Section Determination

The output of the WV-PCS model described in Chapter 4 is presented in this chapter for both the C5-A and 747.

Because experimental results exist for VHF, UHF, L-Band, and S-Band at various times after rollup and different look angles, the atmospheric parameter, A, corresponding to the environmental conditions at the time and location of the Kwajelein experiment is used for determination of radar cross section (RCS). This allows a comparison of simulated results from the passive conservative approach with actual experimental data.

5.1 Determination of Atmospheric Parameter, A

A sounding of the atmospheric water vapor content is available when the Kwajelein experiment was performed [Gilson, 1991]. Table 5.1 summarizes the important atmospheric parameters during the experiment. Since the relative humidity was high (about 80%), the water vapor contributed almost entirely to the RCS so that the gradient of the potential

Table 5.1: Environmental Parameters

Quantity	Value
temperature T	300 K
pressure p	1000 mb
water vapor content offset q_o	0.018 kg/kg
water vapor content slope m_q	-8×10^{-6} kg/mkg

temperature was not important. Thus the value of the atmospheric parameter, A, (derived in Section 3.1.4) during the experiment is

$$A \approx 10^{-12}[6830 m_q]^2 = -184\,\mathrm{dB} \tag{5.1}$$

5.2 Temporal Evolution of Water Vapor Distribution

Output 1 of the WV-PCS described in Section 4.8 is used to form grey scale contour plots of the general passive conservative field, $s(\mathbf{r}, t)$. Figures 5.1 through 5.6 show various views of the initially stratified passive conservative field with the brighter regions indicating a larger value (initially at lower altitude) and the darker regions indicating a smaller value (initially at higher altitude). Note that the form of the passive conservative field is independent of the actual atmosphere.

Figure 5.1 shows the passive conservative distribution of the wake vortex system for the C5-A after 70 seconds of simulation.

The vortex core of the left wake vortex is outlined and the vertically aligned rectangle is

the region represented by the expanded views in Figures 5.2 and 5.3. The "horizontally aligned ledge" is the discontinuity that contributes strongly to incoherent Bragg scatter for a 90^o (vertical) look angle. The "vertically aligned channel" is principally responsible for the incoherent Bragg scatter for a 0^o (horizontal) look angle. These are discussed more fully in Section 5.3.

Figures 5.2 and 5.3 represents a higher resolution temporal evolution of the passive conservative distribution. From this, it can be seen that the small scale refractive index variations are from a relatively small region surrounding the wake vortex core. There is appreciable more RCS as the passive conservative distribution is stretched into smaller scales (comparable to radar wavelength) over time. When the scales are stretched small enough, there is coherent Bragg scatter due to the coherently summed reflection off of each of the small scale spirals. Within the core, the passive conservative at rollup is entrained so it does not contribute to RCS and is fully mixed within a short period of time. This homogeneity within the core is consistent with previous experimental work [Maxworthy, 1972].

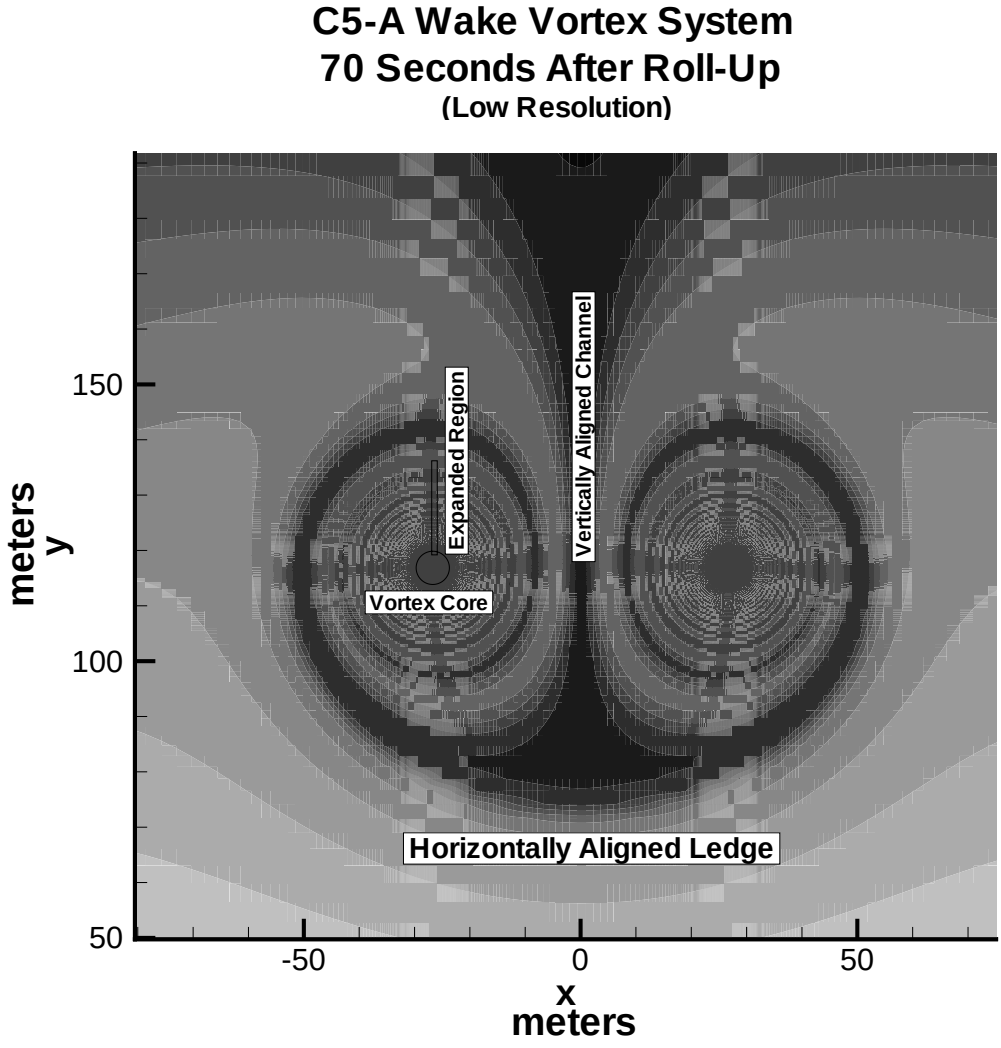

Figure 5.1: Full View of Water Vapor Distribution for C-5A, 70 Seconds After Rollup

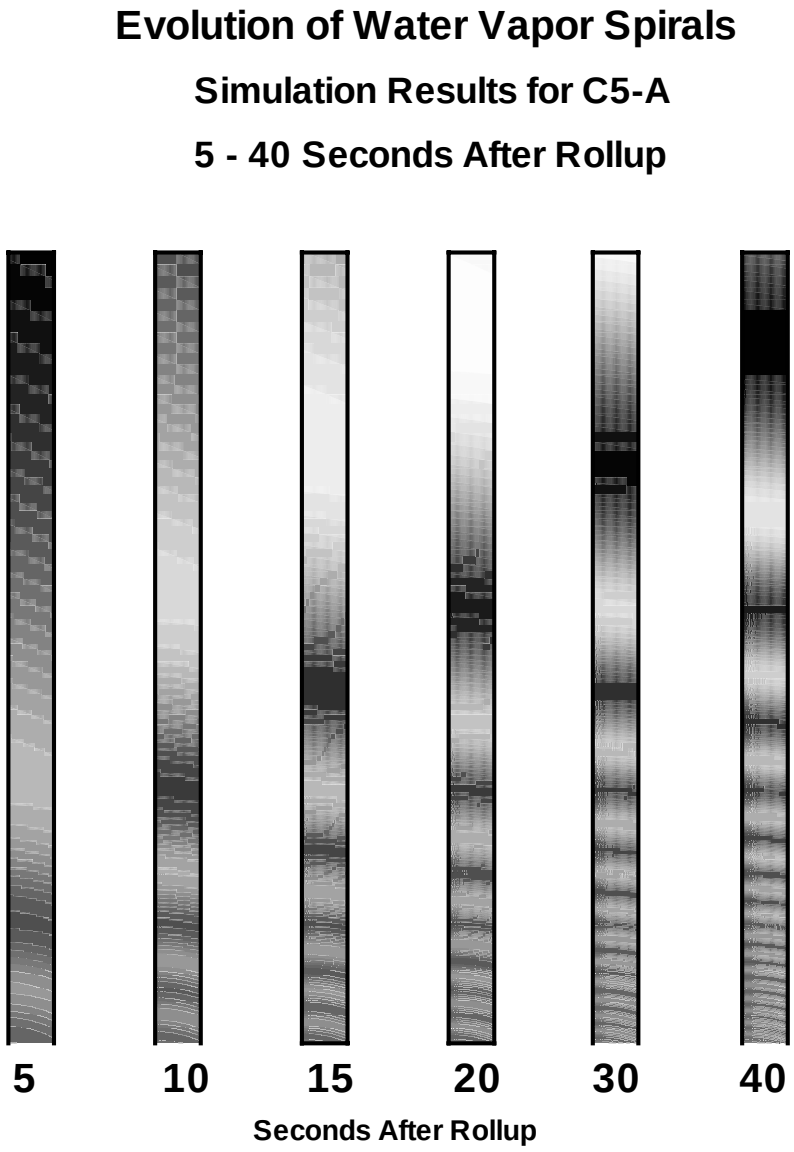

Figure 5.2: Spiral Visualization of Water Vapor for C-5A, 5-40 Seconds

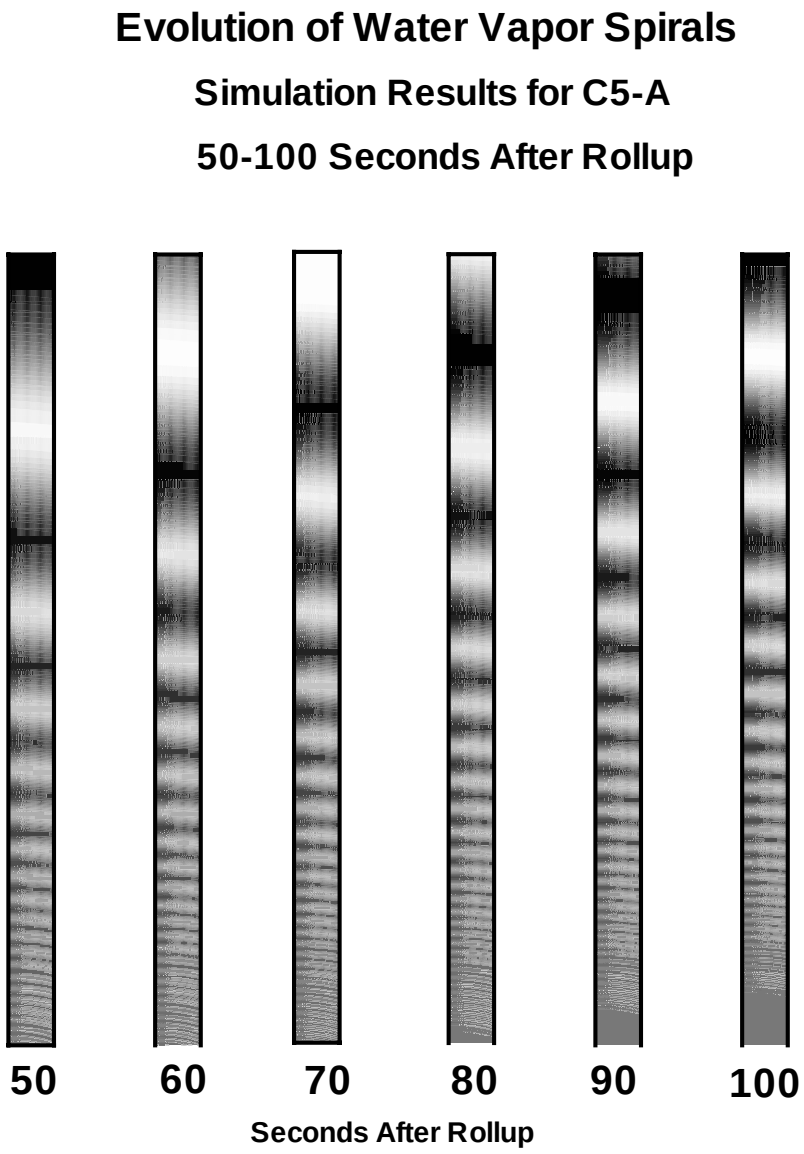

Figure 5.3: Spiral Visualization of Water Vapor for C-5A, 50-100 Seconds

5.3 Temporal Evolution of RCS Spectrum

During the execution of the WV-PCS, the RCS spectrum was computed at specific snapshots in time. These snapshots give an indication of the frequency dependence of RCS as a function of time.

Section 3.1.5 derived the dependence of RCS upon the generalized passive conservative, s, and the atmospheric parameter, A,

$$\sigma(\mathbf{k_t}, t) = A\frac{k_o^4}{\pi}|\phi_s(2\mathbf{k_t}, t)|^2. \tag{5.2}$$

Output 2 described in Section 4.8 of the WV-PCS serves as input to Equation 5.2 and the results were plotted in Figures 5.4 through 5.15 for the Kwajelein atmosphere. Recall that the relationship between frequency and wavenumber vector is $|\mathbf{k_t}| = \frac{\omega}{c}$.

The results in Figures 5.4 to 5.15 can be directly applied to an arbitrary atmosphere through the use of the following formula where the RCS, σ, is in units of $\mathrm{dBm}^2/\mathrm{m}$

$$\sigma(\mathrm{dBm}^2/\mathrm{m}) = \sigma_{kwaj}(\mathrm{dBm}^2/\mathrm{m}) + 20\log[(0.878 + 45.5q_o)m_\theta + (6830)m_q] + 64\,\mathrm{dBm}^2/\mathrm{m} \tag{5.3}$$

where σ_{kwaj} is the y-axis value of Figures 5.4 through 5.15.

5.3.1 C-5A

Figures 5.4 through 5.11 show the temporal evolution of the RCS spectrum for the C5-A.

Figure 5.4 shows the spectrum between 5 and 20 seconds for a 90^o look angle or when the

wake vortex is directly overhead. Figure 5.5 shows a similar evolution with the difference that the wake vortex system is at a 0^o look angle which is when the aircraft is close to the horizon. Notice that the RCS is much larger at VHF than it is at higher frequencies at 5 seconds after rollup. At 20 seconds, this region of larger RCS has extended to the UHF band. This corresponds to the passive conservative spirals being stretched from initial size scales on the order of several meters which correspond to VHF, into scales on the order of 1 meter which is comparable to UHF wavelength. Scattering from these small spirals will be referred to as coherent because it relies on the coherent addition of scattered field off of each of the individual small spirals.

Referring back to Figure 5.1, notice that there is a large discontinuity of passive conservative content below and surrounding the entire wake vortex system that is generally aligned horizontally and is labeled "horizontally aligned ledge." This large structure causes reflection similar to the way in which any discontinuous interface causes reflection. At a 90^o look angle, this energy is reflected directly back into the receiver of the radar. At 0^o, the reflection comes predominantly from the "vertically aligned channel" shown in Figure 5.1. This discontinuity is not as severe as the "horizontally aligned ledge" which explains the approximately 30 dB less incoherent RCS at 90^o then at 0^o. Scattering from these large structures will be referred to as incoherent to differentiate between the coherent scatter from the small scale spirals.

Figures 5.6 and 5.7 show the temporal evolution of RCS spectrum between 30 and 60 seconds. The passive conservative spirals are continuously stretched into smaller and smaller scales and the region of large coherent RCS extends to higher and higher frequencies over time. By 60 seconds, this region is nearing L-Band. Notice that in this region of large, coherent RCS, both 0^o and 90^o look angles have similarly valued RCS. This indicates that the coherent reflection from the small water vapor structure dominates the incoherent scatter. The RCS has the same value because, close to the core of the wake vortices where

the smallest scale structure exists, the structure is symmetrical with respect to the look angle (it is circularly symmetric) as can be seen in Figure 5.1. This causes the RCS to be independent of angle. Notice that the RCS due to incoherent scatter grows during the period for both 0^o and 90^o look angles. This is because the large spirals are of increasingly large gradient. The mixing action of the wake vortex system brings in passive conservative content from increasingly distant altitudes. This causes the large outer spirals to consist of growing passive conservative content from the lower altitudes being swirled into spirals of decreasing passive conservative content from the higher altitudes.

Figures 5.8 and 5.9 show a continuation of earlier trends between 70 and 100 seconds.

Figures 5.10 and 5.11 shows the temporal evolution between 110 and 115 seconds. In these figures, a small scale instability is beginning to develop in the simulation due to the spirals becoming comparable to the resolution of the grid. This causes inflated RCS values at the higher frequencies. The peak RCS of coherent scatter is still thought to be accurate and reaches approximately -85 dBm^2/m at 115 seconds for the VHF, UHF, and L-Bands.

Continued simulation after 115 seconds was not possible due to the spirals becoming smaller than the resolution of the grid.

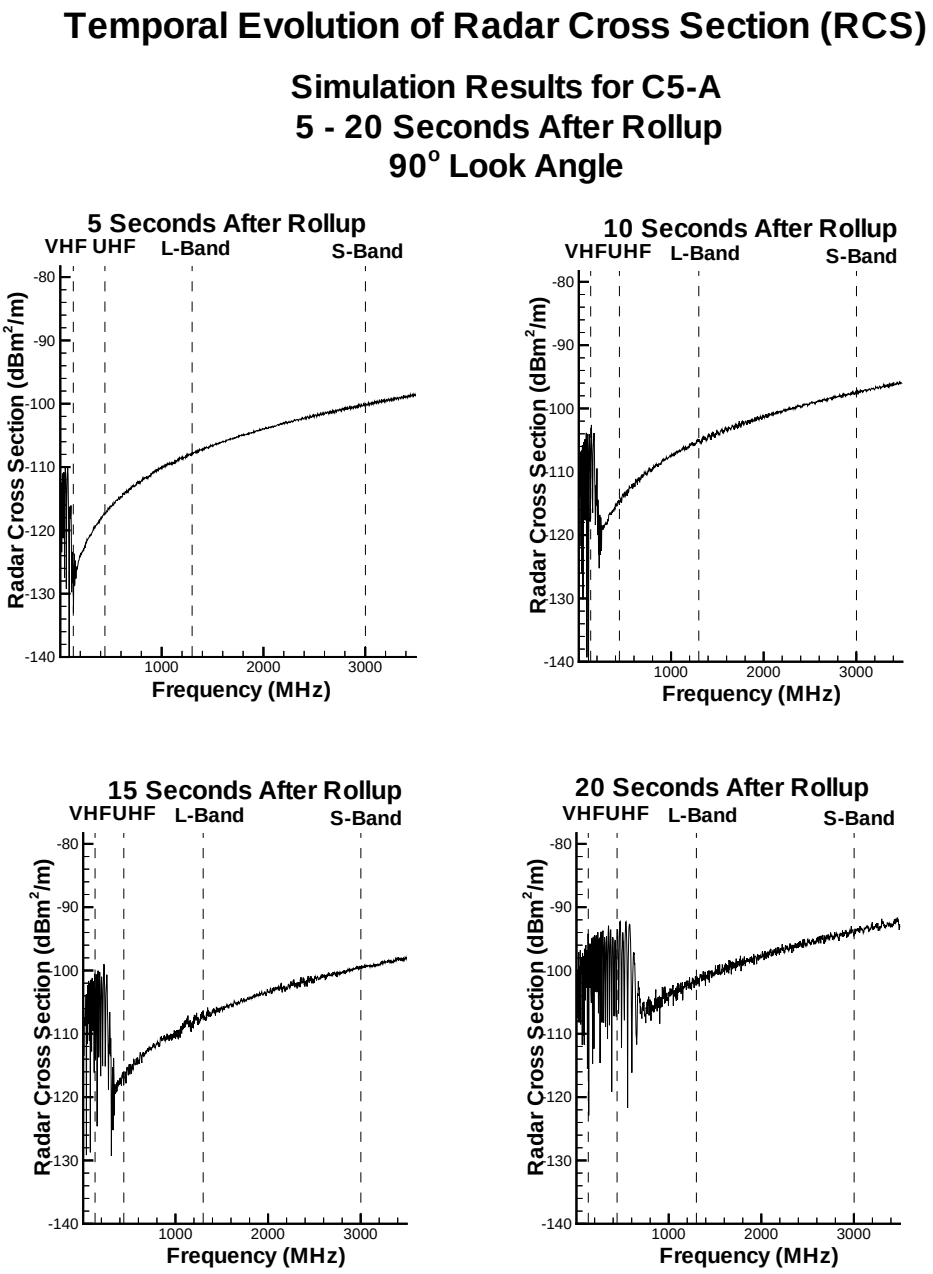

Figure 5.4: Evolution of RCS for C-5A, 5-20 Seconds, 90^o Look Angle

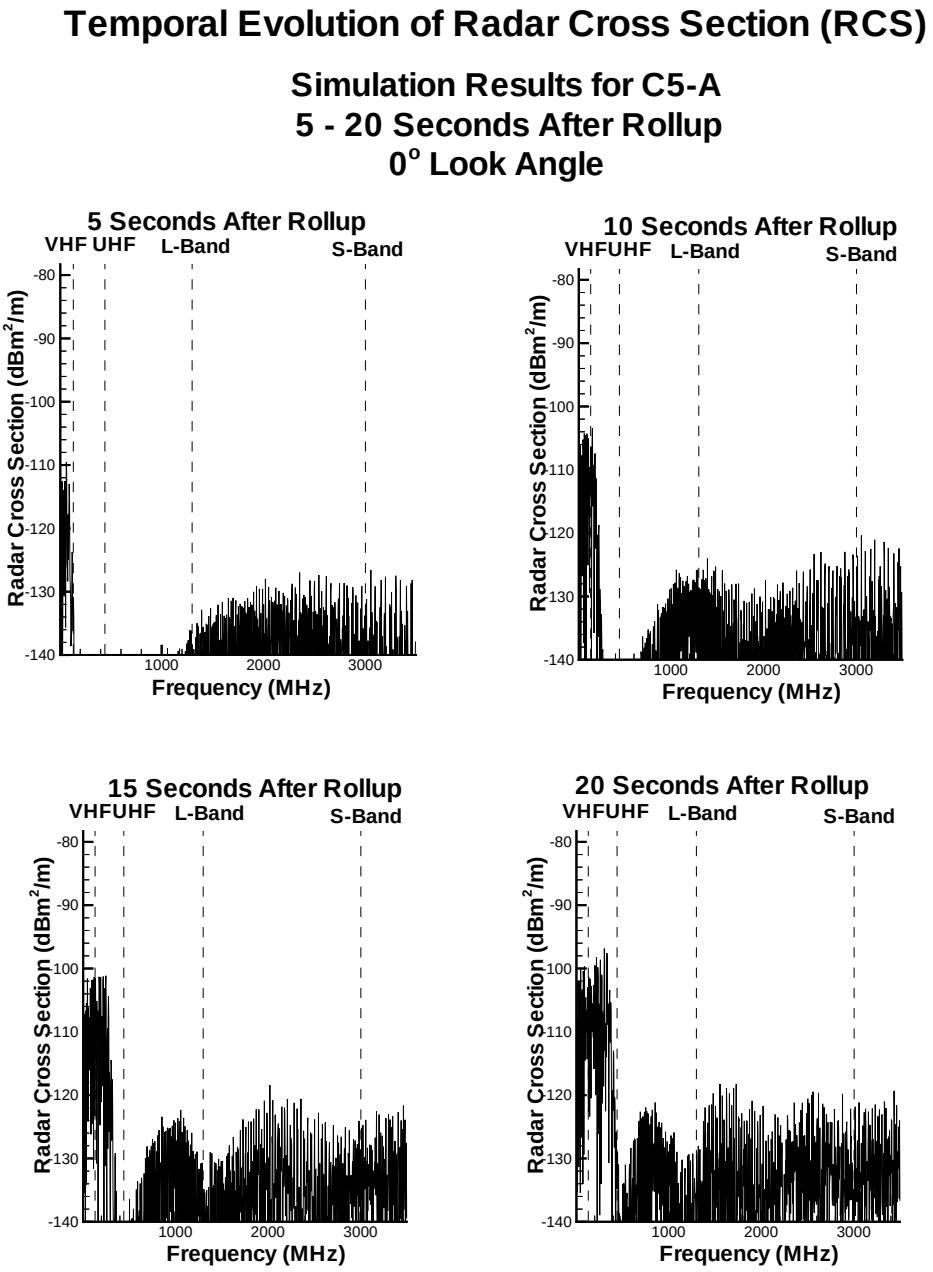

Figure 5.5: Evolution of RCS for C-5A, 5-20 Seconds, 0^o Look Angle

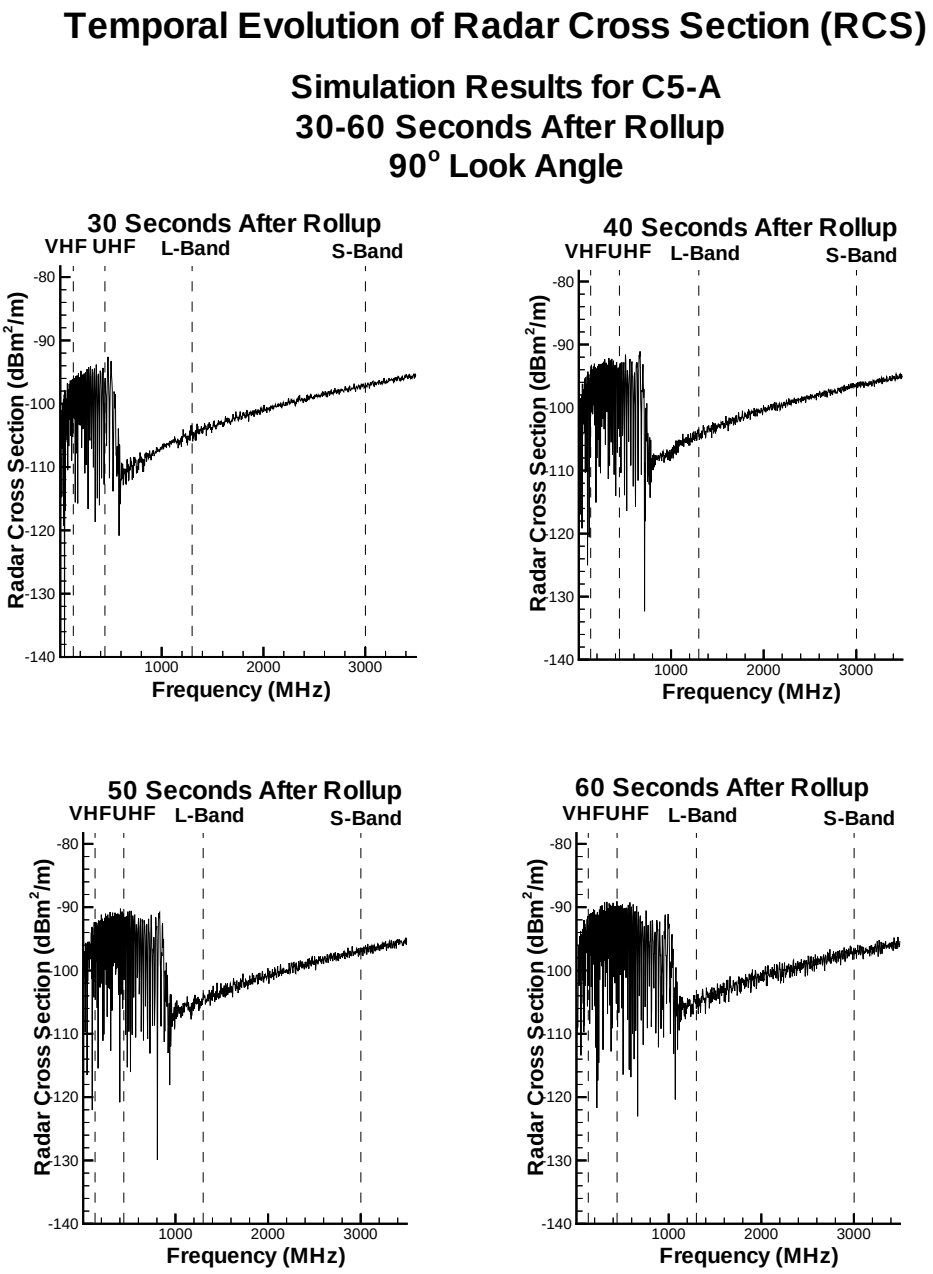

Figure 5.6: Evolution of RCS for C-5A, 30-60 Seconds, 90^o Look Angle

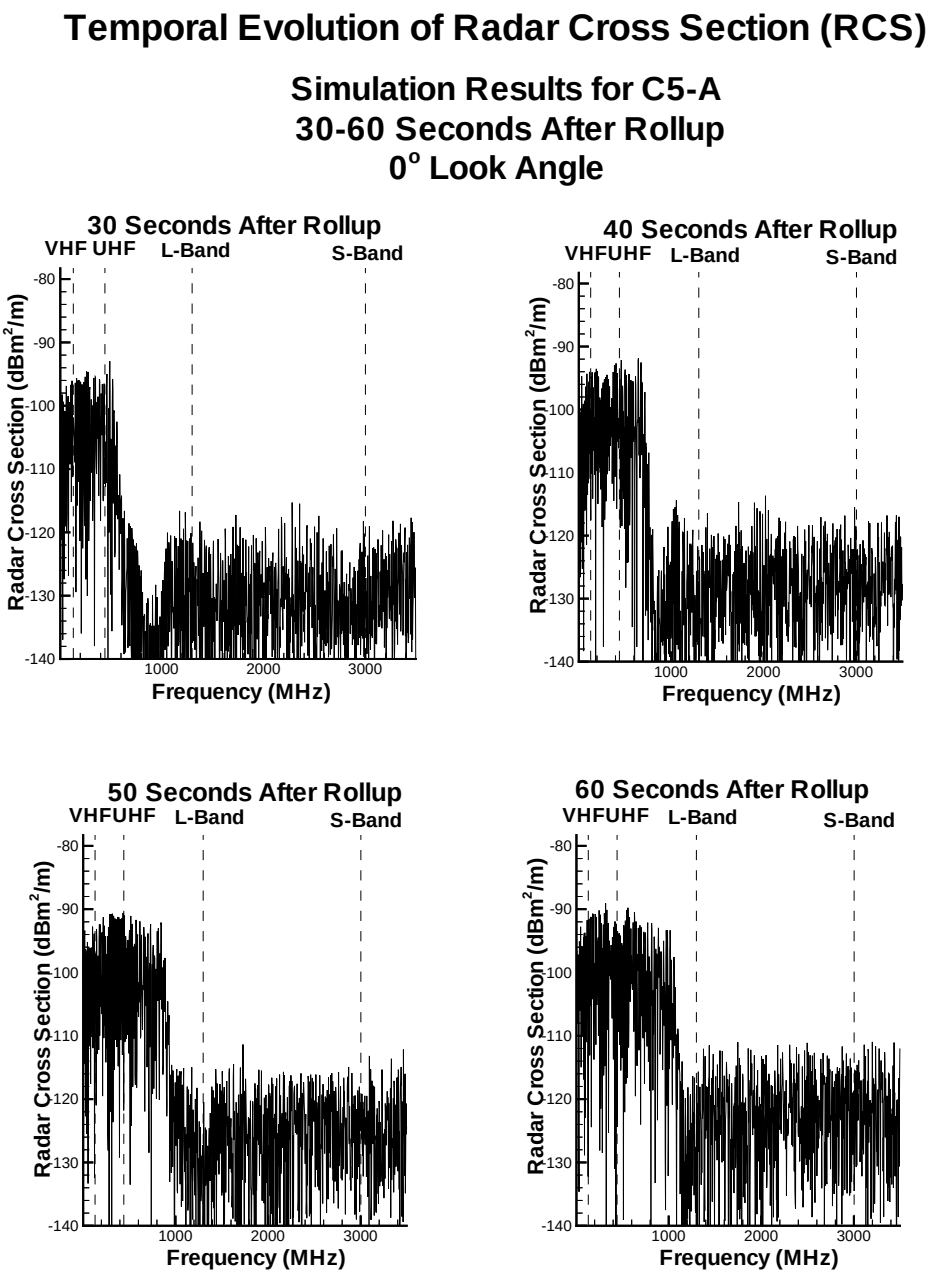

Figure 5.7: Evolution of RCS for C-5A, 30-60 Seconds, 0^o Look Angle

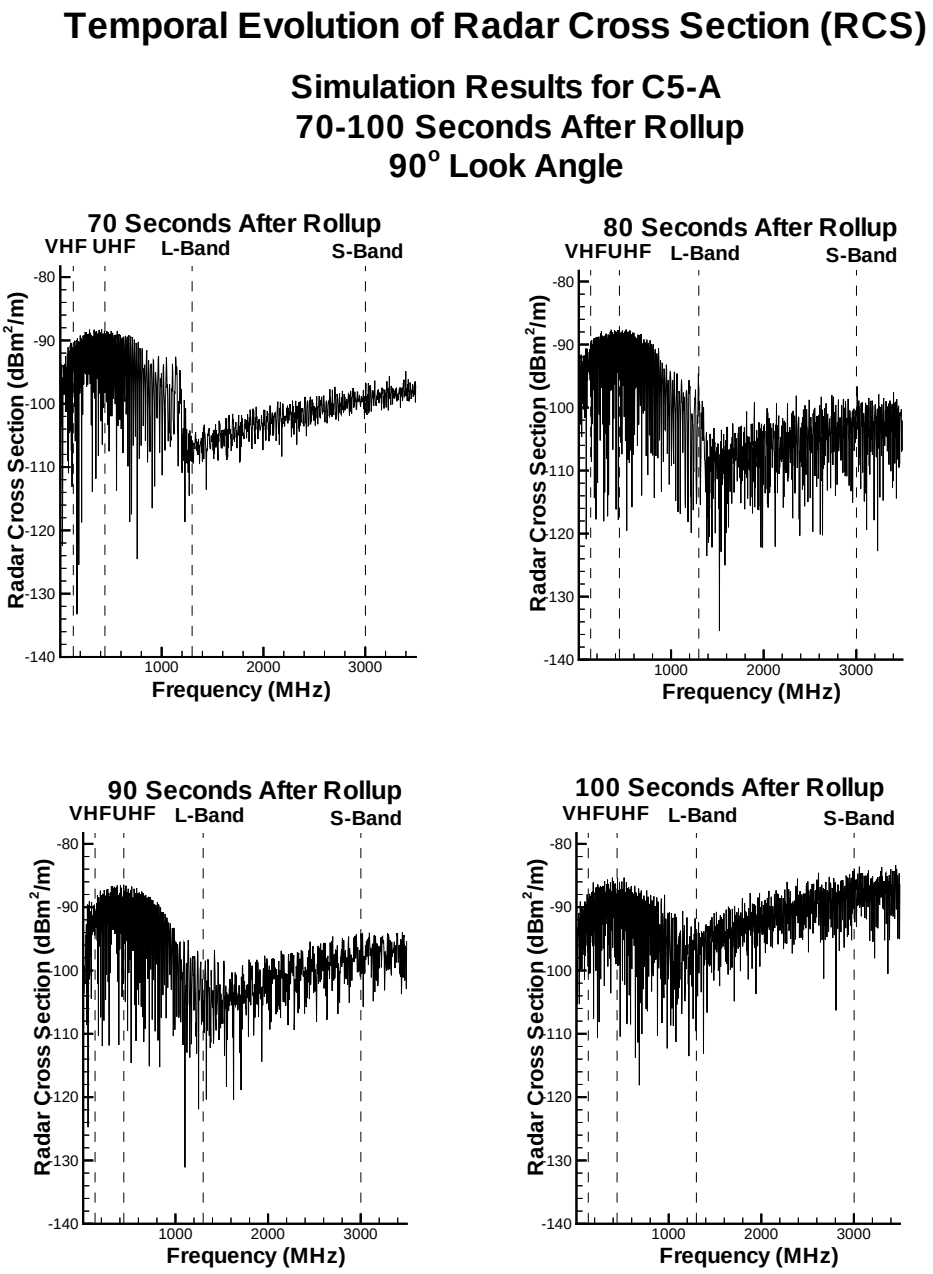

Figure 5.8: Evolution of RCS for C-5A, 70-100 Seconds, 90^o Look Angle

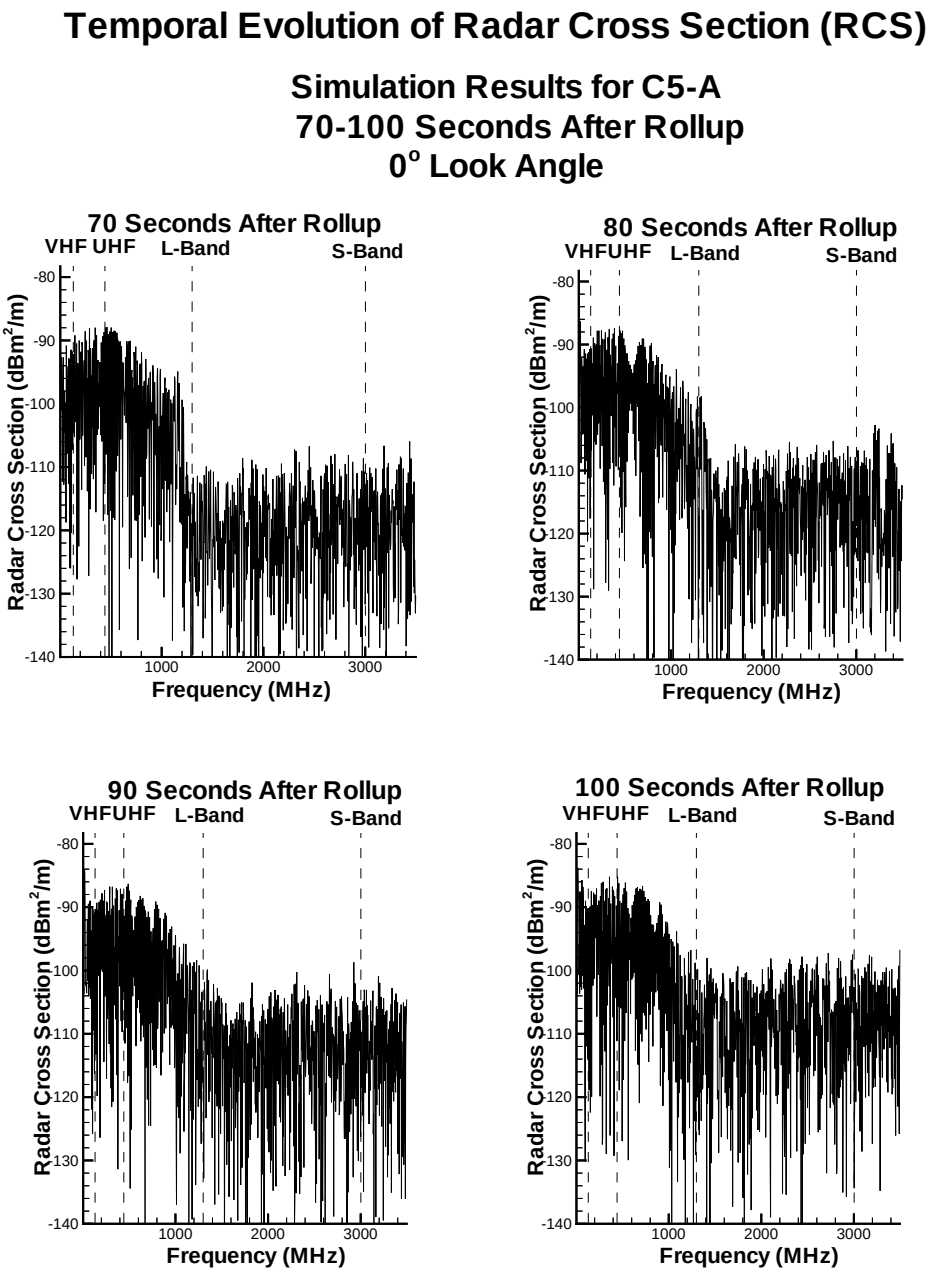

Figure 5.9: Evolution of RCS for C-5A, 70-100 Seconds, 0^o Look Angle

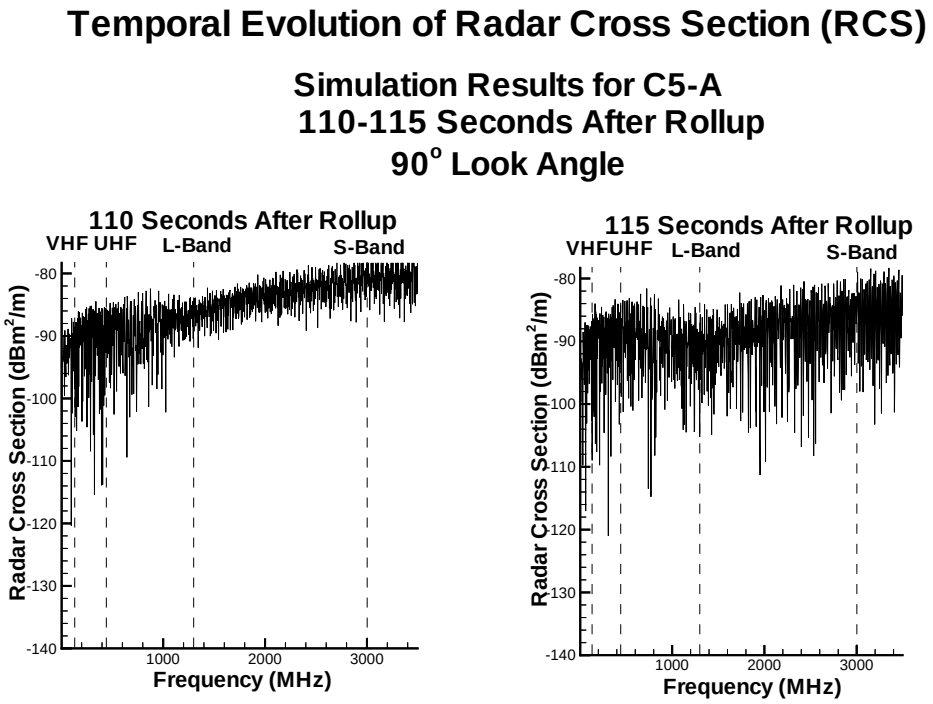

Figure 5.10: Evolution of RCS for C-5A, 110-115 Seconds, 90^o Look Angle

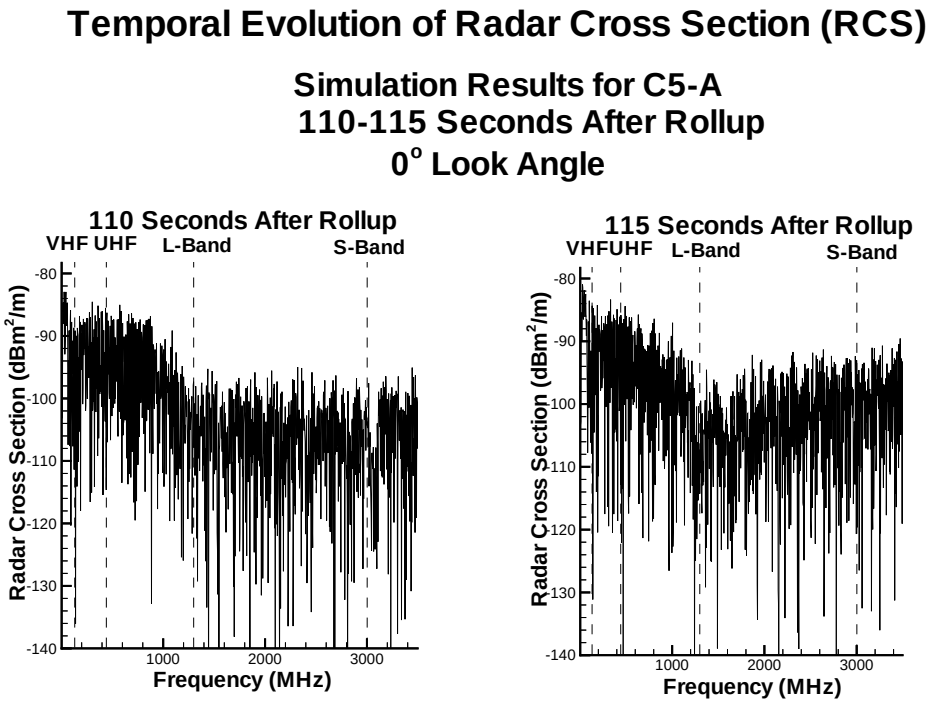

Figure 5.11: Evolution of RCS for C-5A, 110-115 Seconds, 90^o Look Angle

5.3.2 747

Figures 5.12 to 5.15 show the temporal evolution of the RCS spectrum for the wake vortex generated by the 747. This aircraft is assumed to be on final landing approach and thus a lower aircraft velocity is assumed. The RCS of the 747 has many similar features to that of the C5-A. Section 3.3 details the relationship between parameters of the aircraft and the behavior of the generated wake vortex system. Equation 3.40 contains a time scaling factor that is equal to $\left(\frac{B_{C5}}{B}\right)^2 \left(\frac{M}{M_{C5}}\right) \left(\frac{v_{C5}}{v}\right) \approx 3/8$. This means that, for example, the RCS spectrum of the 747 in Figure 5.14 at 30 seconds should be comparable to the RCS spectrum of the C5-A at 80 seconds in Figure 5.8.

Figure 5.13 shows the RCS spectrum at 0^o look angle. Similar to the C-5A, the coherent RCS is the same value as at the 90^o look angle. The incoherent scatter is much less at 0^o because of the "horizontally aligned ledge" shown in Figure 5.1.

Figures 5.14 and 5.15 show the RCS between 25 seconds and 35 seconds. This shows a trend similar to that of the C-5A where the coherent scatter continues to grow and stays at equal values for both 0^o and 90^o look angle. The value of this coherent RCS peaks at approximately -85 dBm^2/m for the VHF, UHF, and L-Band. The incoherent RCS at 90^o has reached -100 dBm^2/m. At 0^o, the incoherent RCS has reached -110 dBm^2/m. Note that at 35 seconds, these values are exceeded but this is probably due to the small scale instabilities that develop when the spirals become comparable in size to the resolution of the grid.

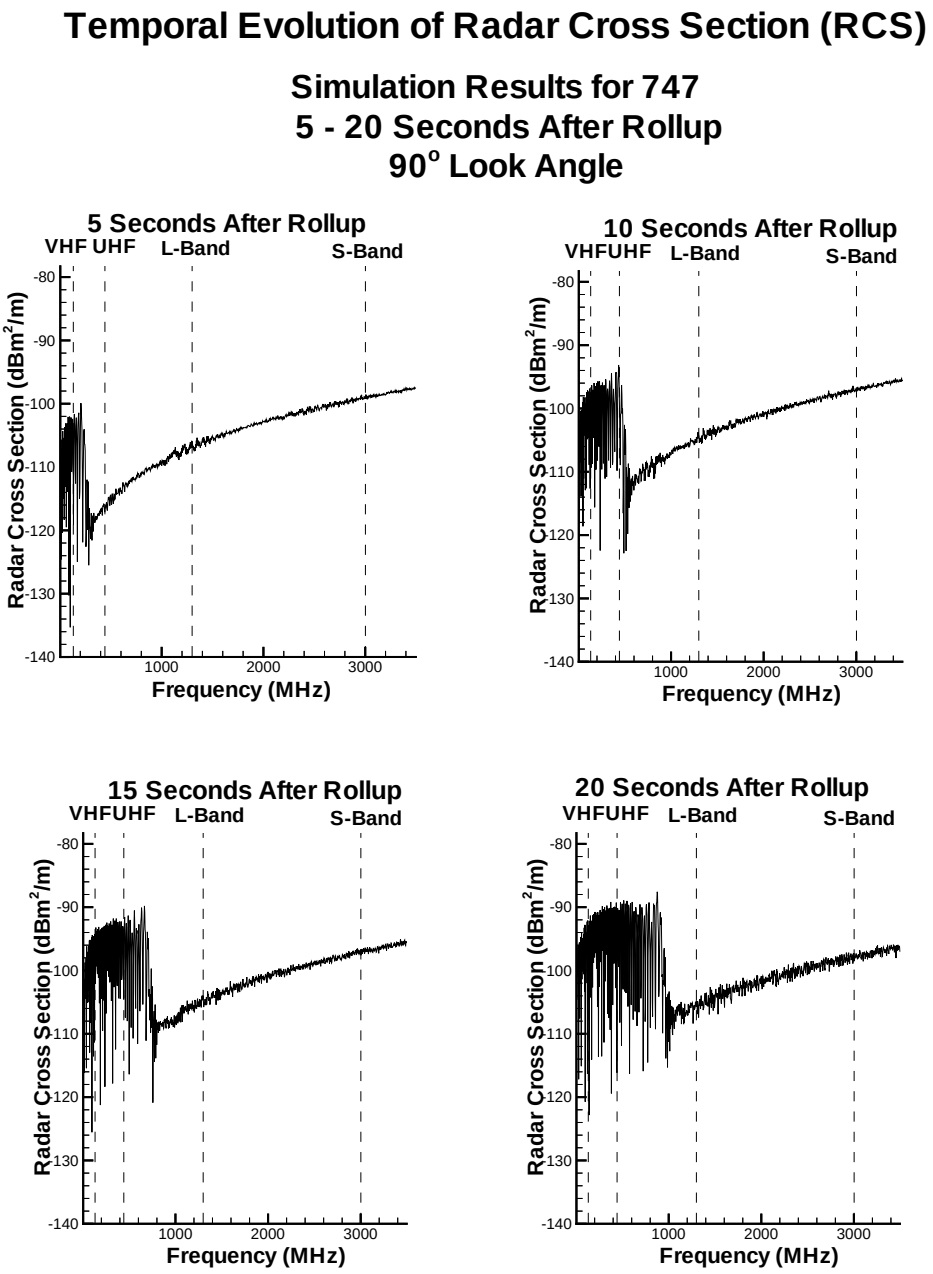

Figure 5.12: Evolution of RCS for 747, 5-20 Seconds, 90^o Look Angle

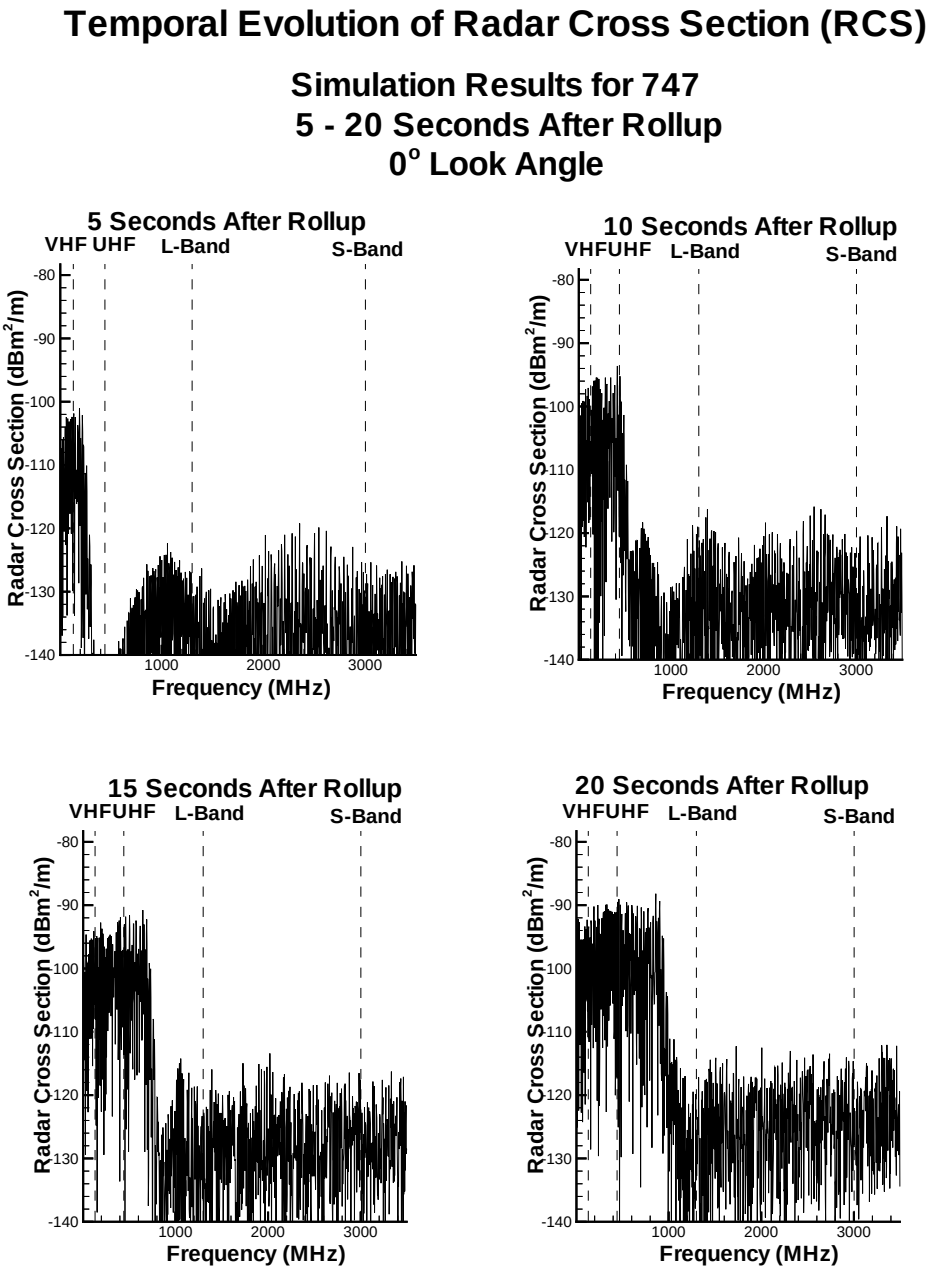

Figure 5.13: Evolution of RCS for 747, 5-20 Seconds, 0^o Look Angle

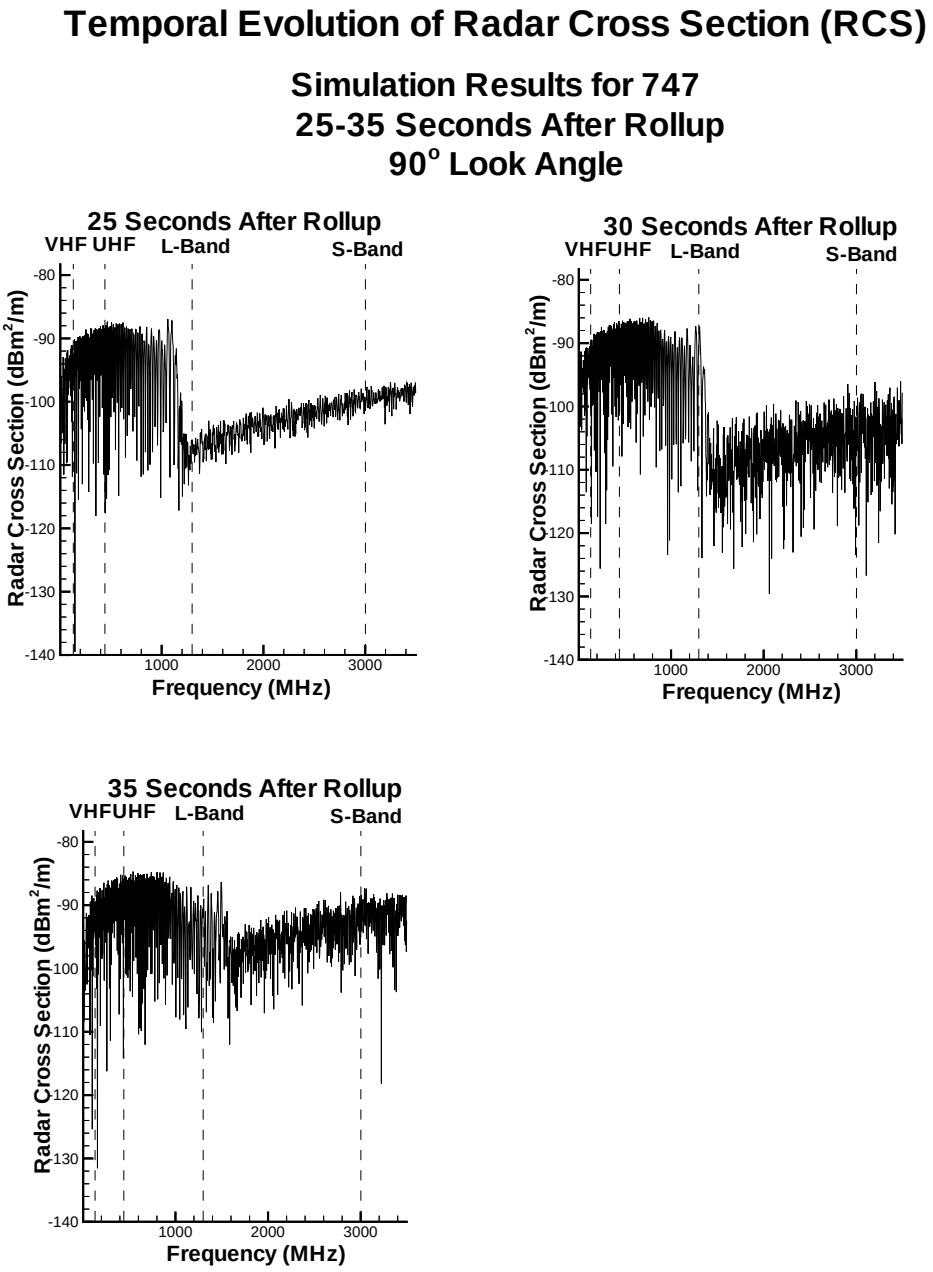

Figure 5.14: Evolution of RCS for 747, 25-35 Seconds, 90^o Look Angle

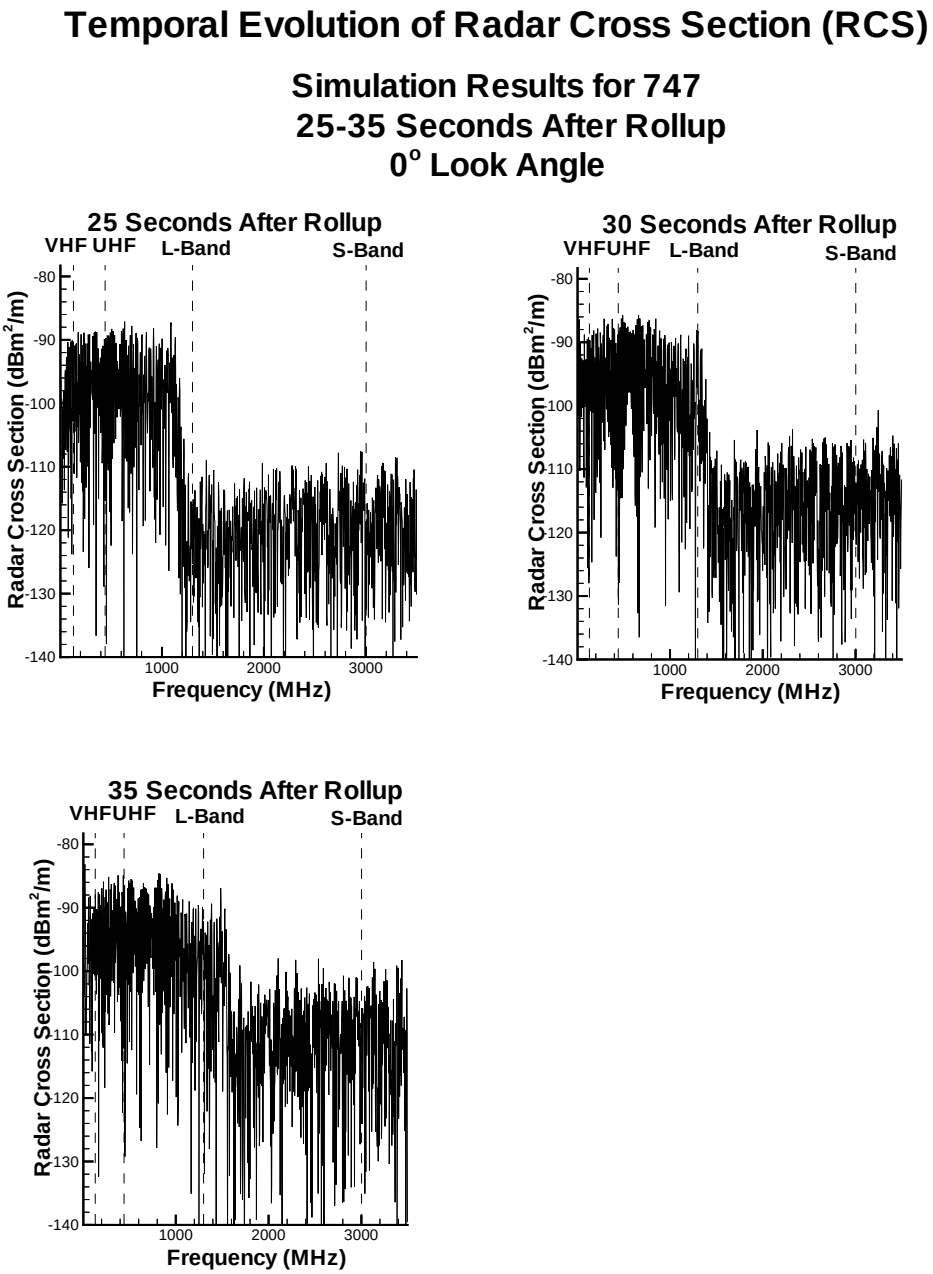

Figure 5.15: Evolution of RCS for 747, 25-35 Seconds, 0^o Look Angle

5.4 Temporal Evolution of RCS at Selected Bands

The WV-PCS outputs RCS after every iteration for select frequency bands. Output 3 from Section 4.8 is presented here. Figure 5.16 shows the evolution of RCS for VHF, UHF, L-Band, and S-Band. This corresponds to experimental results that cites 5 dB to 10 dB variability in the measure RCS for these bands [Gilson, 1991]. Note that Equation 5.4 is valid for generalization to any atmospheric stratification for Figures 5.16 through 5.18.

Figure 5.16 and 5.17 shows the temporal evolution for the C5-A at 90^o and 0^o respectively. These figures indicate the point when the coherent scatter occurs. At VHF, this occurs at 10 seconds, and at UHF, the larger coherent scatter begins at approximately 20 seconds. This is consistent in both the 90^o and 0^o look angles which is verification that the coherent scatter is isotropic. At L-Band, the drastic increase in RCS occurs at 80 seconds for both look angles.

Figure 5.18 shows the temporal evolution of the 747. There is a more rapid development of RCS than with the C-5A. This is consistent with Equation 3.40 which contains a time scaling factor of $\left(\frac{B_{C5}}{B}\right)^2 \left(\frac{M}{M_{C5}}\right) \left(\frac{v_{C5}}{v}\right) \approx 3/8$.

Tables 5.2 and 5.3 contain the experimental results of the C5-A run for which the simulation corresponds for both the 90^o and 0^o look angle. The RCS determined through simulation compares favorable to that reported during the Kwajelein experiment. Also, the time for the RCS to develop (on the order of a minute) is consistent in both simulation and experiment. Though the experimental results were reported for 90 seconds after rollup, they match more closely simulation results at 115 seconds or greater. The discrepancy may be accounted for by errors in the velocity initialization either by an inaccurate circulation, vortex core radius, vortex core separation, or inaccuracy in the Burnham-Hallock model itself.

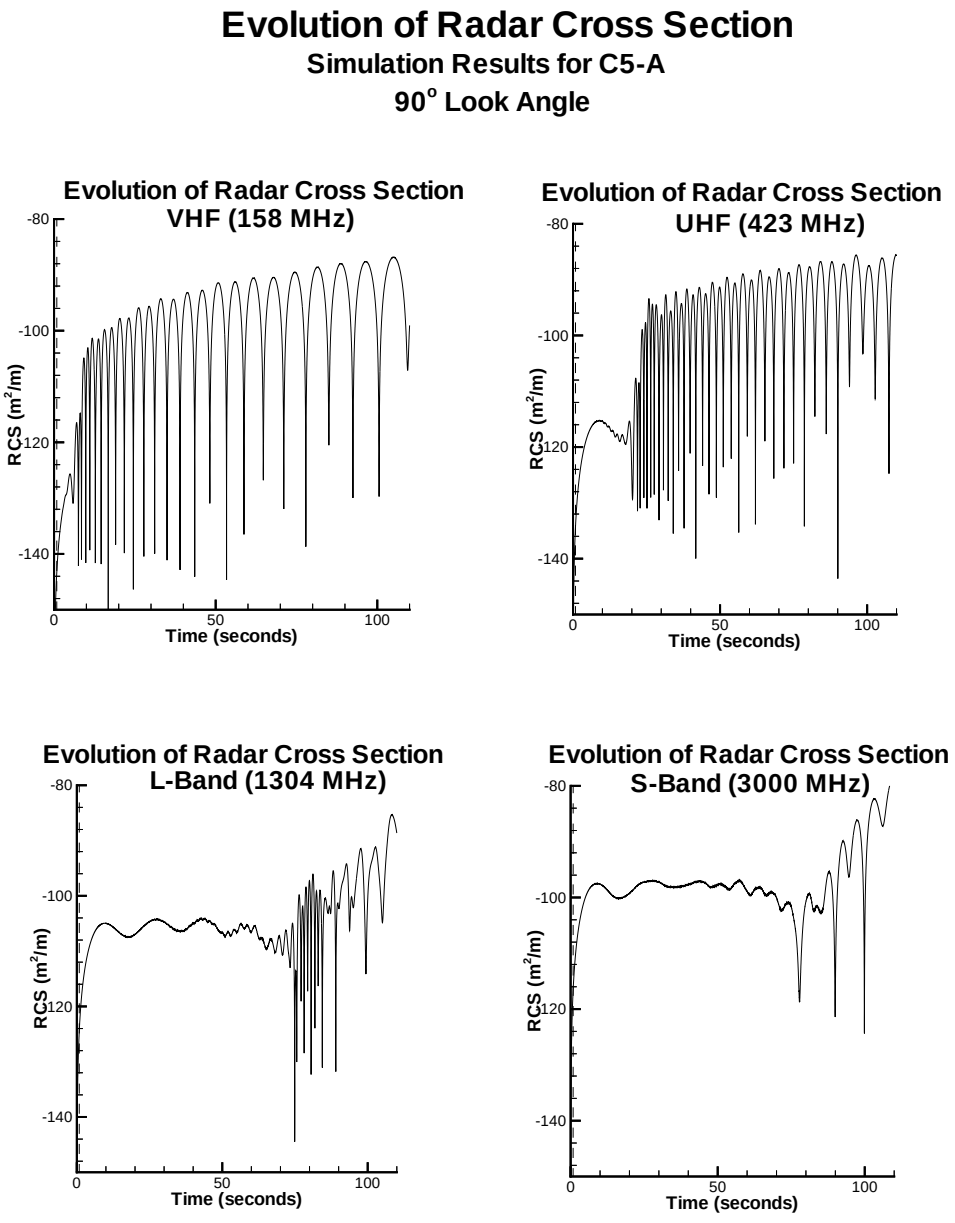

Figure 5.16: RCS Evolution for C-5A at 90^o Look Angle

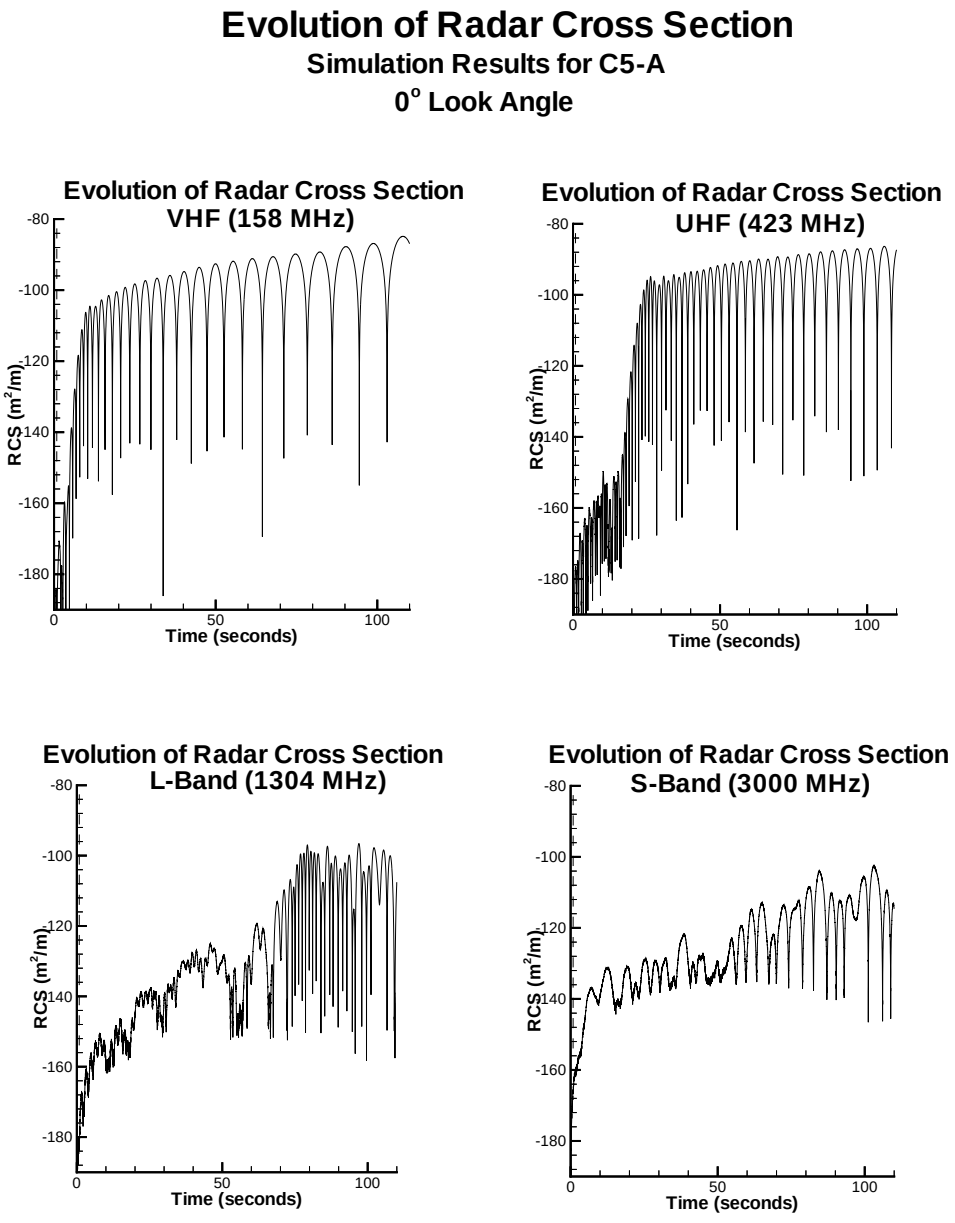

Figure 5.17: RCS Evolution for C-5A at 0^o Look Angle

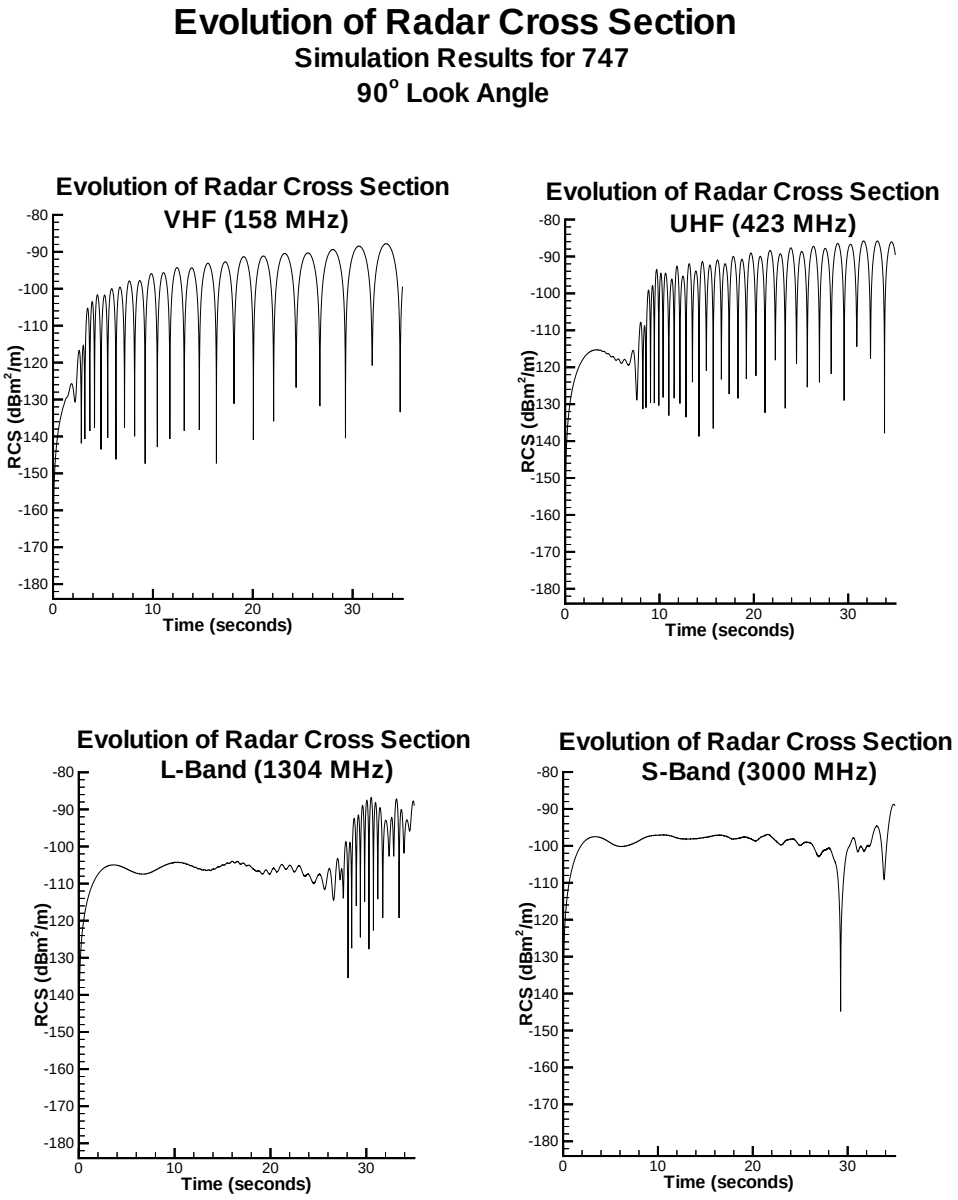

Figure 5.18: RCS Evolution for 747 at 90^o Look Angle

Table 5.2: Reported Radar Cross Sections at 90 Seconds for a C5-A at a 90^o Look Angle

Band	Radar Cross Section Range
VHF	-82 dB to -80 dB
L-Band	-85 dB to -81 dB
S-Band	-83 dB to -79 dB

Table 5.3: Reported Radar Cross Sections at 90 Seconds for a C5-A at a 10^o Look Angle

Band	Radar Cross Section Range
L-Band	-83 dB to -86 dB
S-Band	-84 dB to -85 dB

5.5 Extrapolated Radar Cross Section

To demonstrate the validity of the approximation in Equation 3.40 regarding extrapolation of C5-A results to other aircraft, it is useful to compare the extrapolated RCS spectrum to the RCS spectrum of the actual 747 simulation. Figure 5.19 shows these two spectra side by side. As mentioned earlier, there is a very good match of the lower frequencies. At higher frequencies there is an error due to the artificially small diffusion constant that is implicit in the extrapolation. This causes unrealistically large RCS in the extrapolated spectrum.

Figure 5.20 shows the extrapolated spectrum for a Learjet-36. The Learjet-36 was another aircraft used in wake vortex RCS measurement during the Kwajalein experiment [Gilson, 1991]. The parameters of the aircraft are summarized in Table 5.4.

It is very important to emphasize that the extrapolated RCS at the higher frequencies is actually smaller than shown due to the diffusion factor being artificially reduced by a factor

Table 5.4: Learjet-36 Parameters

Quantity	Value
mass M	8 Mg
wingspan B	12 m
air speed V_a	133 m/s
Γ_∞	$54\,\mathrm{m}^2/\mathrm{s}$

of approximately 5 in Equation 3.40. In actuality, the diffusion process would reduce the small scale variations corresponding to the larger wavenumbers. To compute the effect of this, a full simulation would need to be performed for the Learjet-36.

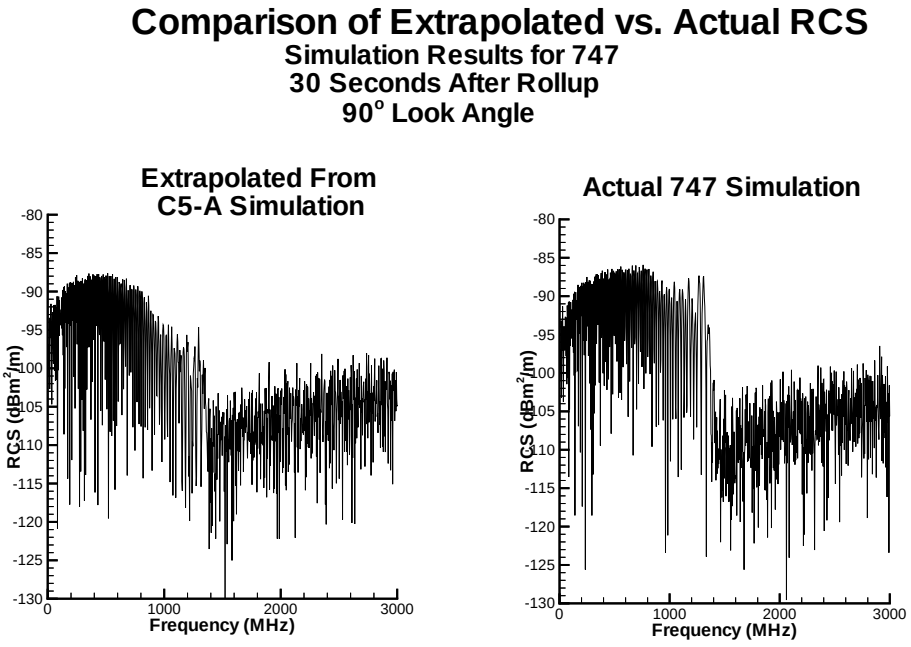

Figure 5.19: Extrapolated vs. Actual 747 RCS

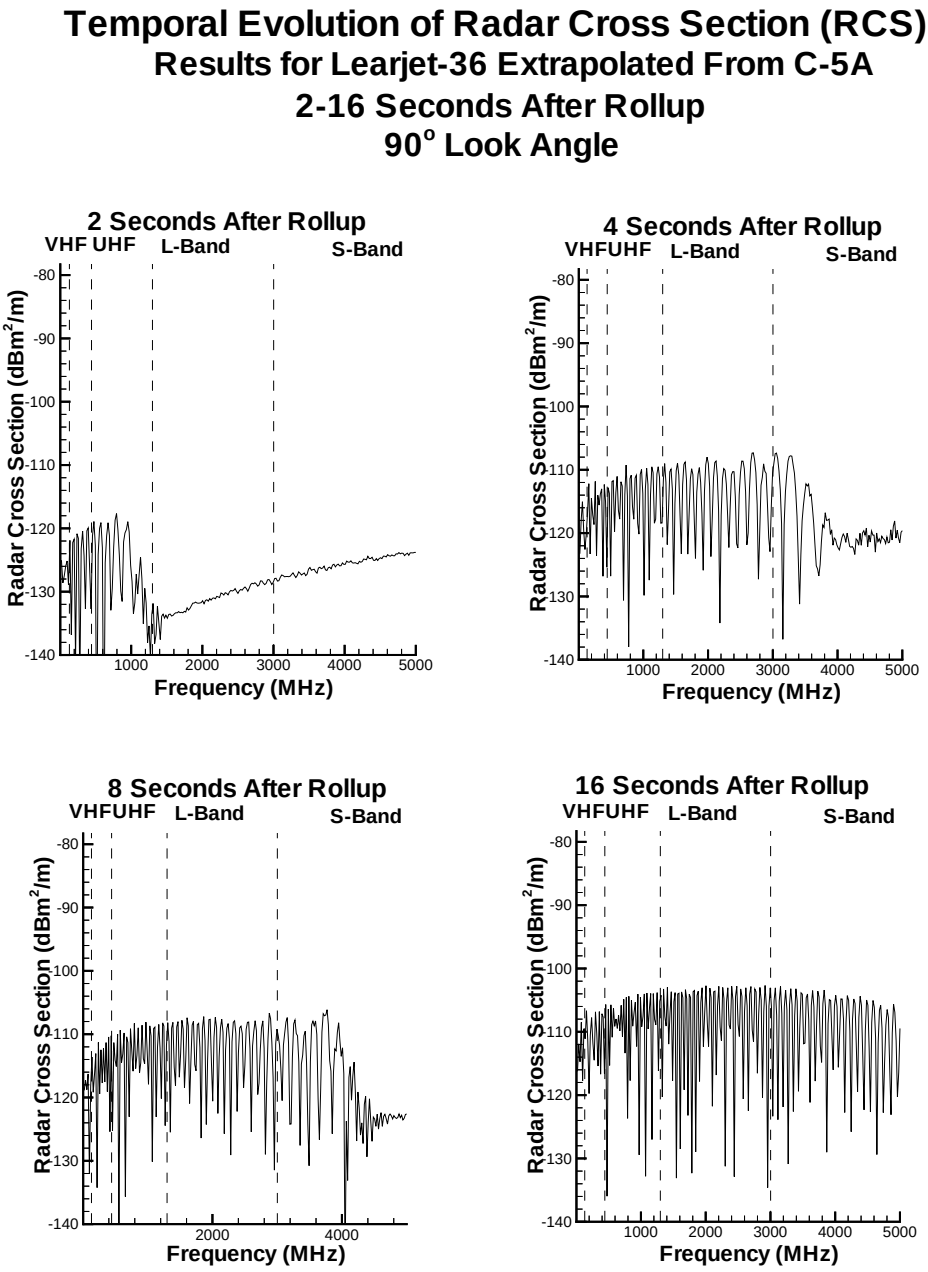

Figure 5.20: Extrapolated Learjet-36 RCS

5.6 Bistatic Radar Cross Section

The bistatic measurement was attempted at L-Band using an angle of 150^o between transmitter direction and receiver direction [Gilson, 1991]. The general expression for bistatic radar cross section was determined in Section 2.4. Substituting Equation 3.21 into Equation 2.48 yields

$$\sigma(\frac{\mathbf{k_t} - \mathbf{k_r}}{2}) = A\frac{k_o^4}{\pi}|\phi_s(\mathbf{k_t} - \mathbf{k_r})|^2 = A\frac{k_o^4}{\pi}|\phi_s(\cos(\theta/2)\mathbf{k_v})|^2 \tag{5.4}$$

where $\mathbf{k_t}$ is the vector in the direction of the transmitter to the wake vortex, $\mathbf{k_r}$ is the vector in the direction of the wake vortex to the receiver, $\mathbf{k_v}$ is in the vertical direction, and $|\mathbf{k_t}| = |\mathbf{k_r}| = |\mathbf{k_v}| = k_o$.

When the test was performed, turbulence was thought to be the generator of RCS. The turbulent spectrum is isotropic and proportional to $k_o^{-11/3}$ [Tartarski, 1971] thus

$$|\phi_s(\cos(\theta/2)\mathbf{k_v})|^2 = |\phi_s(\cos(\theta/2)k_o)|^2 = \cos(\theta/2)^{-11/3}|\phi_s(k_o)|^2. \tag{5.5}$$

Thus, if turbulence was the cause of RCS, the bistatic measurement would yield a value of $\cos(75^o)^{-11/3} \approx 21.5\,\text{dB}$ greater than the monostatic measurement.

Figure 5.26 shows the calculated monostatic RCS and the bistatic RCS for the laminar flow mixing mechanism as output by the WV-PCS. The simulation could not resolve to the bistatic size scales at L-Band (or equivalently compute $\phi_s(\cos(75^o)\mathbf{k_v})$), but 800 MHz was resolvable and on the same order of magnitude. Note that there is coherent RCS for the monostatic case at 800 MHz but the same frequency for the bistatic RCS is from incoherent scatter. Although the magnitude at 800 MHz is still approximately 10 dB greater in the

bistatic case, it should be pointed out that the value of incoherent RCS reported in the simulation is most subject to error due to long wavelength instabilities that effect the large scale structures which predominantly contribute to incoherent RCS.

The experiment did not show an RCS enhancement with the bistatic system. This is consistent with the laminar flow mechanism and inconsistent with turbulence being the cause of the RCS.

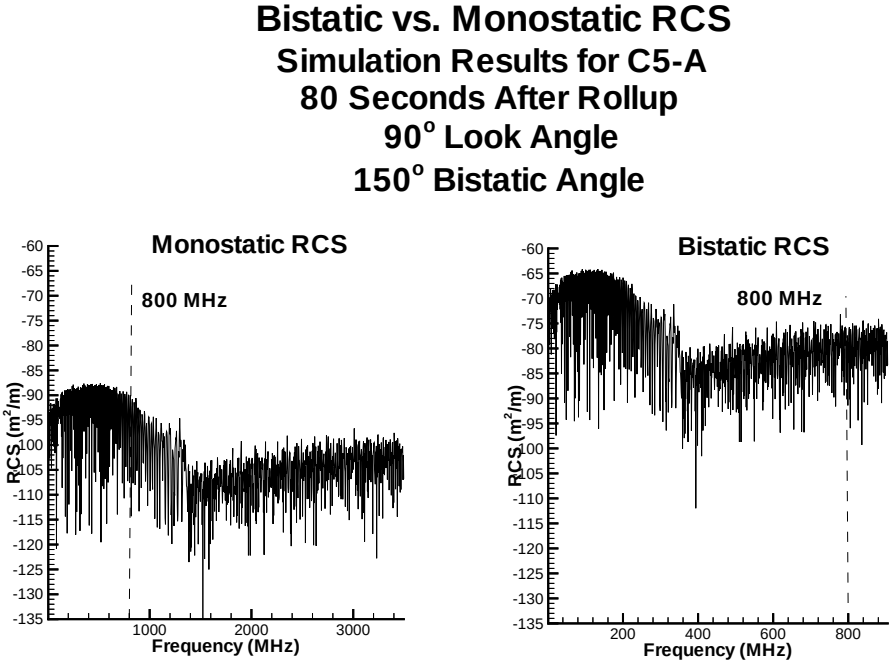

Figure 5.21: Bistatic vs. Monostatic RCS

Chapter 6

Doppler Processing

Doppler processing may be used to provide enhanced wake vortex detection capabilities. To determine the optimal processing, it is very useful to simulate the function of the doppler processor. In most modern radars, doppler processing is accomplished digitally [Schleher, 1991].

Figure 6.1 shows the block diagram of a typical doppler processor. The single pulse return signal serves as the in-phase (x_n) and quadrature (y_n) input. These inputs are weighted and summed using the shift registers and the adders. The Doppler Processing Simulator (DPS) simulates the doppler processor and uses the output of the WV-PCS as the input signals x_n and y_n. The DPS is useful to determine an optimal set of weights to provide the greatest likelyhood of coherent detection.

For a "hard" target such as an aircraft with a constant velocity, SNR is enhanced by using coherent doppler processing because upon weighted addition of received doppler pulses, the coherent signal power is proportional to the square of the number of pulses, while the incoherent noise power adds proportionally to the number of pulses. This yields an SNR

enhancement proportional to the number of pulses.

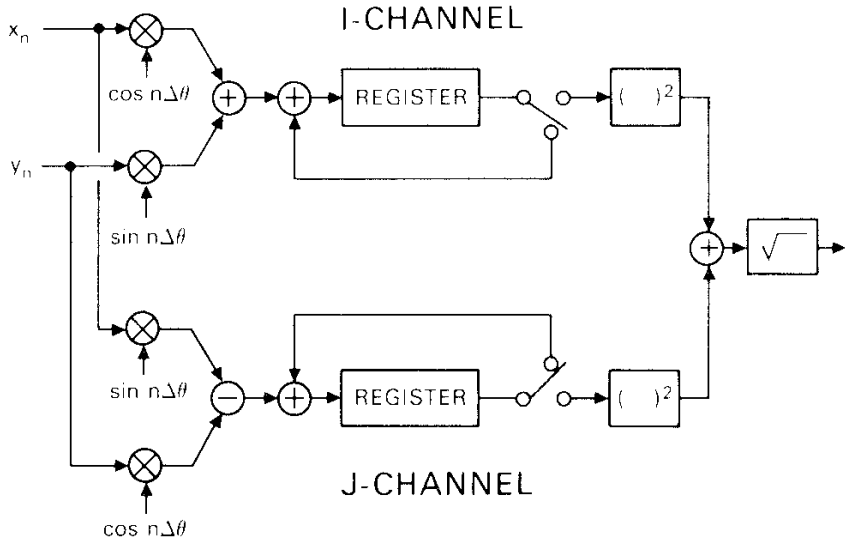

Figure 6.1: Doppler Processor [Schleher, 1991]

6.1 Doppler Processing Simulation (DPS)

The Doppler Processor Simulator (DPS) has been developed to simulate a digital doppler processor. The expression for the output of the processor shown in Figure 6.1 is

$$v_o = \sum_{n=1}^{N} w_n s_n \tag{6.1}$$

where the input complex signal s_n is the output of Figure 6.1 and is defined as $s_n = x_n + jy_n$, w_n is the set of complex filter weights which are

$$w_n = e^{-j2\pi f n \Delta t_p}, \tag{6.2}$$

and Δt_p is the interval between pulses such that $\Delta t_p = \frac{1}{\text{PRF}}$ where PRF is the pulse repetition frequency and

$$f = \frac{2v}{\lambda} \tag{6.3}$$

where v is the doppler velocity.

The coherent processing interval (CPI) is the time that the pulses are coherently summed which is $N\Delta t_p$ for this doppler processor.

The power of the output is then

$$P_o = |\sum_{n=1}^{N} w_n(v_{sn} + n_n)|^2 \tag{6.4}$$

where the input complex signal s_n has been divided into $s_n = v_{sn} + n_n$ where v_{sn} is the signal and n_n is the noise.

Assuming that the signal is not correlated with the noise, Equation 6.4 can be written as

$$P_o = |\sum_{n=1}^{N} w_n v_{sn}|^2 + |\sum_{n=1}^{N} w_n n_n|^2. \tag{6.5}$$

The signal to noise ratio for the output of the doppler processor is thus

$$(SNR)_{dop} = \frac{|\sum_{n=1}^{N} w_n v_{sn}|^2}{|\sum_{n=1}^{N} w_n n_n|^2}. \tag{6.6}$$

The signal v_{sn} is determined using the WV-PCS and the radar equation for a single pulse (Equation 1.1). This equation is for the signal power so we must take the square root to find the voltage level normalized to a 1 Ω impedance. Equation 2.39 is used to find the phase of this voltage which is the phase of the electric field. Thus

$$v_{sn} = \sqrt{\frac{APG^2\lambda^2\ell k_o^4}{(4\pi)^3 R^4 L_a \pi}}\phi_s(2\mathbf{k_t}, n\Delta t_s). \tag{6.7}$$

In this case, we are assuming that the time spacing between adjacent summed pulses is the same as the time spacing in the WV-PCS or that $\Delta t_p = \Delta t_s$. The results will be generalized at the end of the section to allow for an arbitrary PRF.

The noise voltage n_n is assumed to be uncorrelated Gaussian noise and the expression is

$$n_n = \sqrt{kTB}r(n\Delta t_p) \tag{6.8}$$

where $r(t)$ represents a random, independently distributed complex phase.

Substituting Equation 6.7 and 6.8 into Equation 6.6 yields the expression for signal to noise ratio as

$$(SNR)_{dop} = \frac{APG^2\lambda^2\ell k_o^4}{(4\pi)^3 L_a kTB\pi}\frac{|\sum_{n=1}^{N_s} w_n\phi_s(2\mathbf{k_t}, n\Delta t_s)|^2}{|\sum_{n=1}^{N} w_n r(n\Delta t_p)|^2} \tag{6.9}$$

where N_s is the number of simulation time steps during the CPI interval.

Using the fact that for a random phase noise source

$$|\sum_{n=1}^{N} w_n r(n\Delta t_p)|^2 = N|w_n|^2 = N \tag{6.10}$$

Equation 6.9 can be written as

$$(SNR)_{dop} = \frac{APG^2\lambda^2 k_o^4}{(4\pi)^3 L_a kTB\pi} \frac{|\sum_{n=1}^{N_s} w_n \phi_s(2\mathbf{k_t}, n\Delta t_s)|^2}{N}. \tag{6.11}$$

If we introduce the quantity $\sigma(\mathbf{k_t}, t, v)$ as effective RCS and define it as

$$\sigma(\mathbf{k_t}, t, v) = A\frac{k_o^4}{\pi} \frac{|\sum_{n=1}^{N_s} w_n \phi_s(2\mathbf{k_t}, n\Delta t_s)|^2}{N} \tag{6.12}$$

and substitute into Equation 6.11,

$$(SNR)_{dop} = \frac{PG^2\lambda^2 \ell \sigma(\mathbf{k_t}, t, v)}{(4\pi)^3 L_a kTB}. \tag{6.13}$$

Comparing Equation 6.13 with Equation 1.1, note that the effective RCS, $\sigma(\mathbf{k_t}, t, v)$, is the equivalent RCS required to yield the same SNR at the output of the doppler processor as with a single pulse.

To generalize to any PRF, it is necessary to determine the quantity $|\sum_{n=1}^{N} w_n \phi_s(2\mathbf{k_t}, n\Delta t_p)|^2$ where the summation does not necessarily coincide with data available from the WV-PCS. Note that

$$\sum_{n=1}^{N_s} \phi_s(2\mathbf{k_t}, n\Delta t_s) e^{-jfn\Delta t_s} \Delta t_s \approx \int \phi_s(2\mathbf{k_t}, n\Delta t_s) e^{-jft}\, dt \approx \sum_{n=1}^{N} \phi_s(2\mathbf{k_t}, n\Delta t_p) e^{-jfn\Delta t_p} \Delta t_p \tag{6.14}$$

for $f\Delta t_s << 1$, $f\Delta t_p << 1$, and smoothly varying ϕ_s which is a consequence of appropriate resolution in the WV-PCS.

Thus

$$\sum_{n=1}^{N} \phi_s(2\mathbf{k_t}, n\Delta t_p)e^{-jfi\Delta t_p} = \frac{\Delta t_s}{\Delta t_p} \sum_{n=1}^{N_s} \phi_s(2\mathbf{k_t}, n\Delta t_s)e^{-jfi\Delta t_s}. \tag{6.15}$$

Noting that $\frac{\Delta t_s}{\Delta t_p} = \frac{N}{N_s}$ Equation 6.12 may be written as

$$\sigma(\mathbf{k_t}, t, v) = A\frac{k_o^4}{\pi}\left(\frac{N}{N_s^2}\right)|\sum_{n=1}^{N_s} w_n\phi_s(2\mathbf{k_t}, n\Delta t_s)|^2 \tag{6.16}$$

and states that the effective RCS is proportional to the PRF.

6.2 Temporal Evolution of Doppler Spectra

The DPS uses Output 3 of the WV-PCS described in Section 4.8. The WV-PCS computes the complex quantity $\phi_s(2\mathbf{k_t}_i, n\Delta t_s)$ for specific frequency bands during each iteration of the simulation. Using Equation 6.16 and Output 3 described in Section 4.8, the DPS computes the effective RCS.

The following figures show effective radar cross section $\sigma(\mathbf{k_t}, t, v)$ as a function of velocity for the various frequency bands. The dotted line represents the descent velocity of the wake vortex system. Doppler cross section is calculated for VHF, UHF, L-Band, and S-Band. For the 90^o look angle, there is appreciable power centered around v_d. For the 0^o look angle, the doppler cross section is centered around 0 velocity. A doppler processor would enhance SNR if the output corresponding to or near the descent rate of the wake

Table 6.1: Learjet-36 Parameters

Figure	Time	UHF Max.	VHF Max.	L-Band Max.	S-Band Max.
6.2	10 s	-81 dBm^2/m	-82 dBm^2/m	-74 dBm^2/m	-79 dBm^2/m
6.3	20 s	-73 dBm^2/m	-84 dBm^2/m	-77 dBm^2/m	-82 dBm^2/m
6.4	30 s	-64 dBm^2/m	-67 dBm^2/m	-73 dBm^2/m	-79 dBm^2/m
6.5	40 s	-72 dBm^2/m	-64 dBm^2/m	-74 dBm^2/m	-79 dBm^2/m
6.6	50 s	-66 dBm^2/m	-65 dBm^2/m	-76 dBm^2/m	-80 dBm^2/m
6.7	60 s	-70 dBm^2/m	-64 dBm^2/m	-74 dBm^2/m	-80 dBm^2/m
6.8	70 s	-59 dBm^2/m	-61 dBm^2/m	-78 dBm^2/m	-81 dBm^2/m
6.9	80 s	-63 dBm^2/m	-64 dBm^2/m	-72 dBm^2/m	-80 dBm^2/m
6.10	90 s	-55 dBm^2/m	-58 dBm^2/m	-70 dBm^2/m	-82 dBm^2/m
6.11	100 s	-60 dBm^2/m	-62 dBm^2/m	-70 dBm^2/m	-73 dBm^2/m
6.12	110 s	-66 dBm^2/m	-54 dBm^2/m	-54 dBm^2/m	-61 dBm^2/m

vortex system is used. This is a positive feature of the laminar flow mixing mechanism. If turbulence was the cause of the RCS, then the doppler spectrum would be distributed over a large velocity spread. For coherent doppler detection, it is the peak doppler cross section that is of interest. The doppler processor could be tuned to the velocity where there is the greatest doppler cross section. Thus, the more peaked the distribution, the better the SNR at the output of the doppler processor.

The data for the DPS simulation of the C5-A is presented in Section 6.2.1 for the 90^o and 0^o look angles. Section 6.2.2 presents the DPS data for the 747 simulation. Tables 6.1 to 6.3 summarize the figures shown in Sections 6.2.1 and 6.2.2.

Table 6.2: Doppler Processor Summary, C5-A, 0^o Look Angle

Figure	Time	UHF Max.	VHF Max.	L-Band Max.	S-Band Max.
6.13	10 s	-80 dBm^2/m	-132 dBm^2/m	-122 dBm^2/m	-108 dBm^2/m
6.14	20 s	-70 dBm^2/m	-96 dBm^2/m	-117 dBm^2/m	-99 dBm^2/m
6.15	30 s	-67 dBm^2/m	-70 dBm^2/m	-112 dBm^2/m	-97 dBm^2/m
6.16	40 s	-66 dBm^2/m	-67 dBm^2/m	-98 dBm^2/m	-90 dBm^2/m
6.17	50 s	-61 dBm^2/m	-61 dBm^2/m	-99 dBm^2/m	-99 dBm^2/m
6.18	60 s	-67 dBm^2/m	-65 dBm^2/m	-102 dBm^2/m	-93 dBm^2/m
6.19	70 s	-60 dBm^2/m	-58 dBm^2/m	-84 dBm^2/m	-92 dBm^2/m
6.20	80 s	-68 dBm^2/m	-64 dBm^2/m	-72 dBm^2/m	-87 dBm^2/m
6.21	90 s	-56 dBm^2/m	-57 dBm^2/m	-72 dBm^2/m	-80 dBm^2/m
6.22	100 s	-54 dBm^2/m	-64 dBm^2/m	-77 dBm^2/m	-74 dBm^2/m
6.23	110 s	-53 dBm^2/m	-61 dBm^2/m	-79 dBm^2/m	-85 dBm^2/m

Table 6.3: Doppler Processor Summary, 747, 90^o Look Angle

Figure	Time	UHF Max.	VHF Max.	L-Band Max.	S-Band Max.
6.24	5 s	-80 dBm^2/m	-84 dBm^2/m	-103 dBm^2/m	-90 dBm^2/m
6.25	10 s	-70 dBm^2/m	-74 dBm^2/m	-102 dBm^2/m	-90 dBm^2/m
6.26	15 s	-76 dBm^2/m	-69 dBm^2/m	-103 dBm^2/m	-90 dBm^2/m
6.27	20 s	-67 dBm^2/m	-64 dBm^2/m	-104 dBm^2/m	-90 dBm^2/m
6.28	25 s	-70 dBm^2/m	-69 dBm^2/m	-104 dBm^2/m	-90 dBm^2/m
6.29	30 s	-68 dBm^2/m	-68 dBm^2/m	-90 dBm^2/m	-100 dBm^2/m
6.30	35 s	-73 dBm^2/m	-58 dBm^2/m	-90 dBm^2/m	-84 dBm^2/m

6.2.1 C5-A

90^o Look Angle

Figures 6.2 to 6.12 show the effective RCS for a doppler process with a PRF of 1 kHz and a CPI of 2 seconds. The target is the wake vortex for the C5-A and the look angle is 90^o. The effective RCS is plotted as a function of doppler velocity for the four bands: UHF, VHF, L-Band, and S-Band. The doppler processing is shown between 10 seconds and 110 seconds after rollup.

Figure 6.2 shows the effective RCS for 10 seconds after rollup. For each of the frequency bands, the effective RCS peaks at the descent rate of the wake vortex system which is 0.83 m/s and shown by the dotted line. There is the exception of a larger peak for S-Band at -0.2 s which indicates that at the size scale corresponding to S-Band, the smaller scale details of the evolution of the refractive index field begin to dominate over the descent rate of the entire wake vortex system. The width of the velocity peak is largest for the lower frequency bands and get rather small for the higher frequencies. This indicates that in an actual doppler processor at a high frequency, the doppler tuning is much more critical.

Figure 6.3 shows the effective RCS at 20 seconds after rollup. At VHF, the descent rate actually represents a local minimum with peaks centered symmetrically around v_d. The peak effective RCS has increased from the value at 10 seconds. At UHF, the peak is still at the descent rate but the peak value has diminished. This is consistent with the fluctuations observed in Figure 5.21 although the doppler processor does tend to average out these fluctuations so there are not as severe for the case of the single pulse. The L-Band and S-Band peaks have similarly diminished consistent with local temporal variations. The widths of the peaks remains relatively constant.

Figure 6.4 shows the effective RCS at 30 seconds after rollup. There is an increase in peak VHF and UHF effective RCS with the value at approximate -65 dbm/m^2 for VHF and -68 dbm/m^2 for UHF. This represents coherent scatter for these bands off of the spirals that have reached sizes comparable to the wavelengths. At L-Band and S-Band, there exists incoherent scatter off of the horizontally aligned ledge shown in Figure 5.1.

Figure 6.5 shows an increase in VHF peak effective RCS at 40 seconds and a decrease in UHF peak effective RCS with a splitting of the spectrum around v_d. The effective RCS for L-Band and S-Band remains relatively constant.

Figures 6.6 through 6.8 show a continuation of earlier trends at 50 seconds through 70 seconds.

Figure 6.9 shows that at 80 seconds, there is coherent Bragg scatter at L-Band and the peak effective RCS begins to rise. Note that the shape of the doppler spectrum does not depend on whether the scattering mechanism is coherent or incoherent.

Figures 6.10 through 6.12 shows continuing trends at 90 seconds through 110 seconds with coherent scatter continuing to cause peak effective RCS to grow at VHF, UHF, and L-Band. Notice that throughout the simulation, the spectral width remains relatively constant for each of the frequency bands.

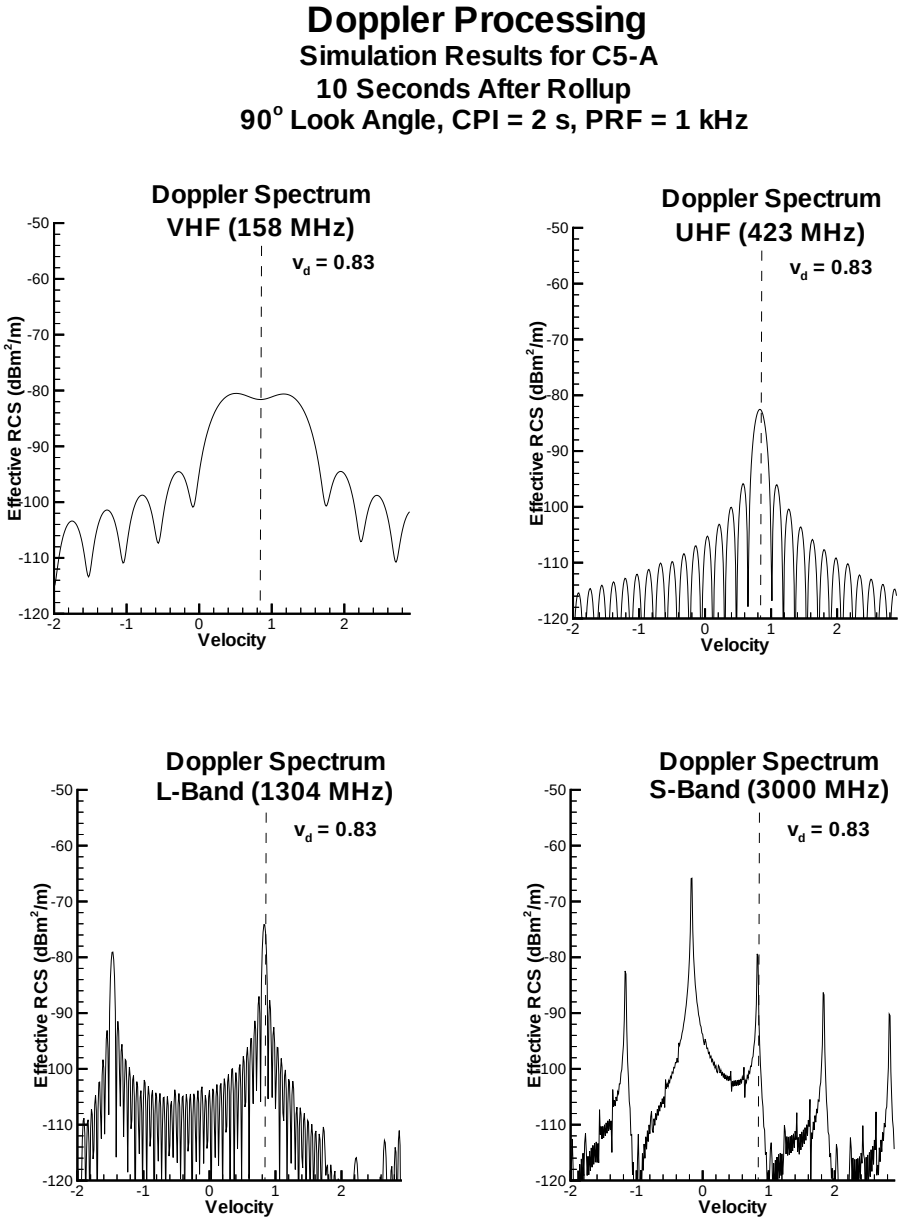

Figure 6.2: Doppler Processing for C-5A, 90^o Look Angle, 10 Seconds

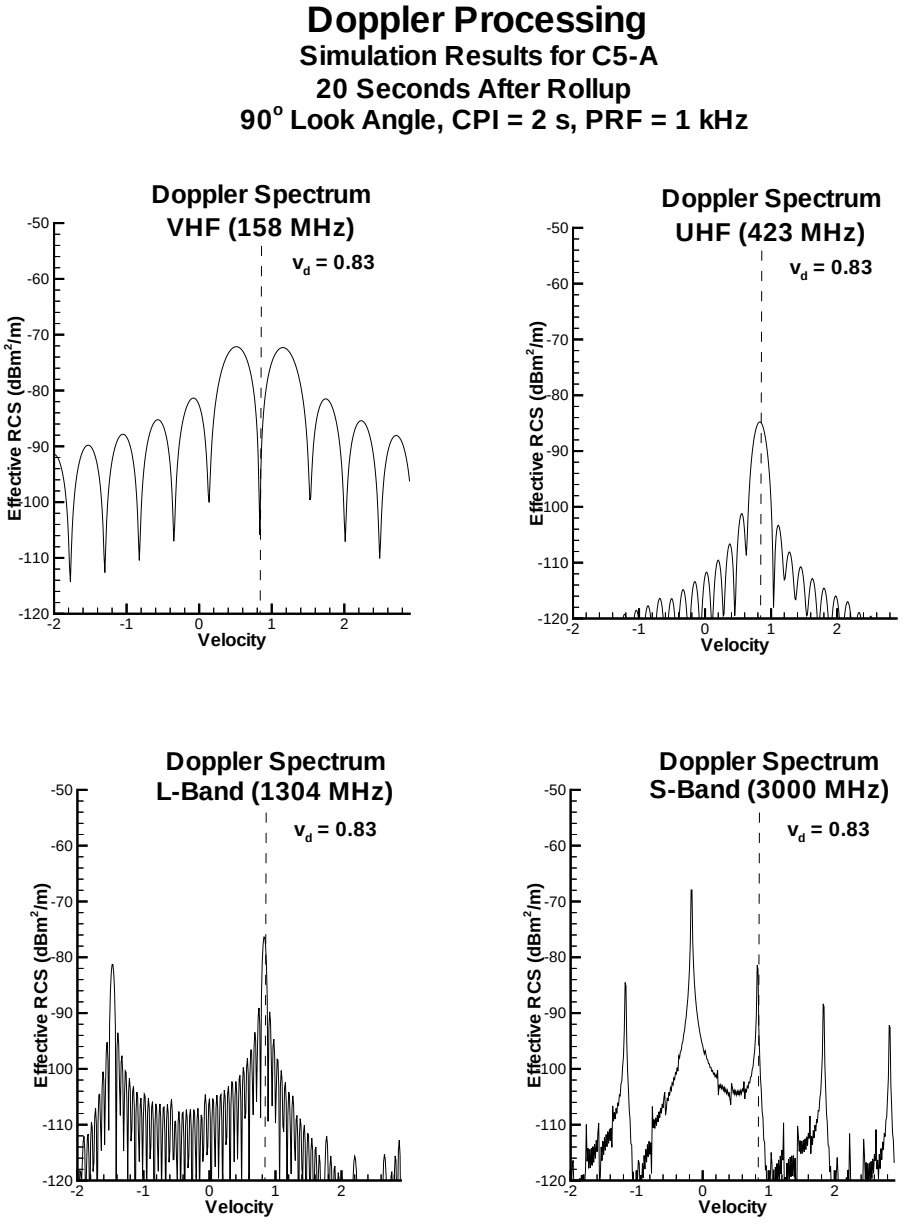

Figure 6.3: Doppler Processing for C-5A, 90^o Look Angle, 20 Seconds

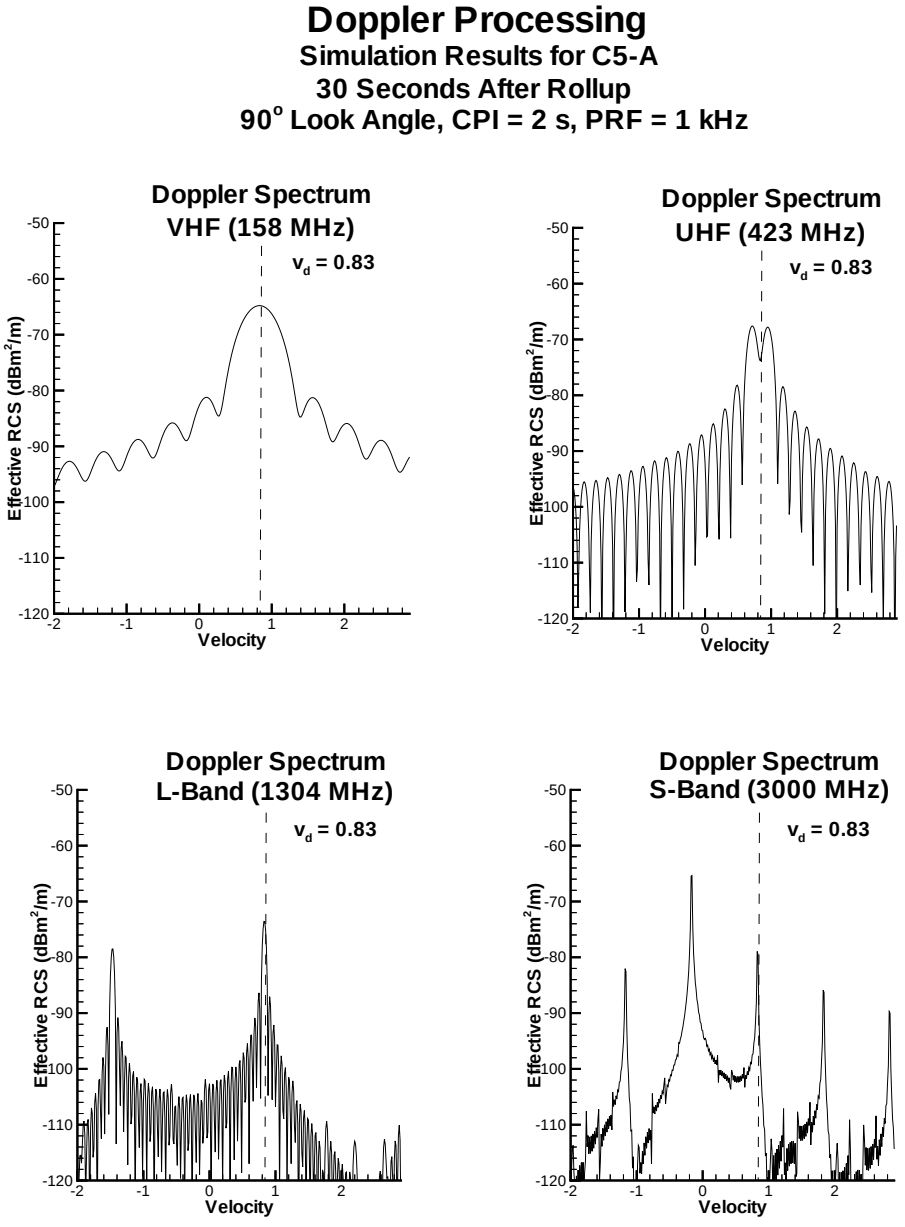

Figure 6.4: Doppler Processing for C-5A, 90^o Look Angle, 30 Seconds

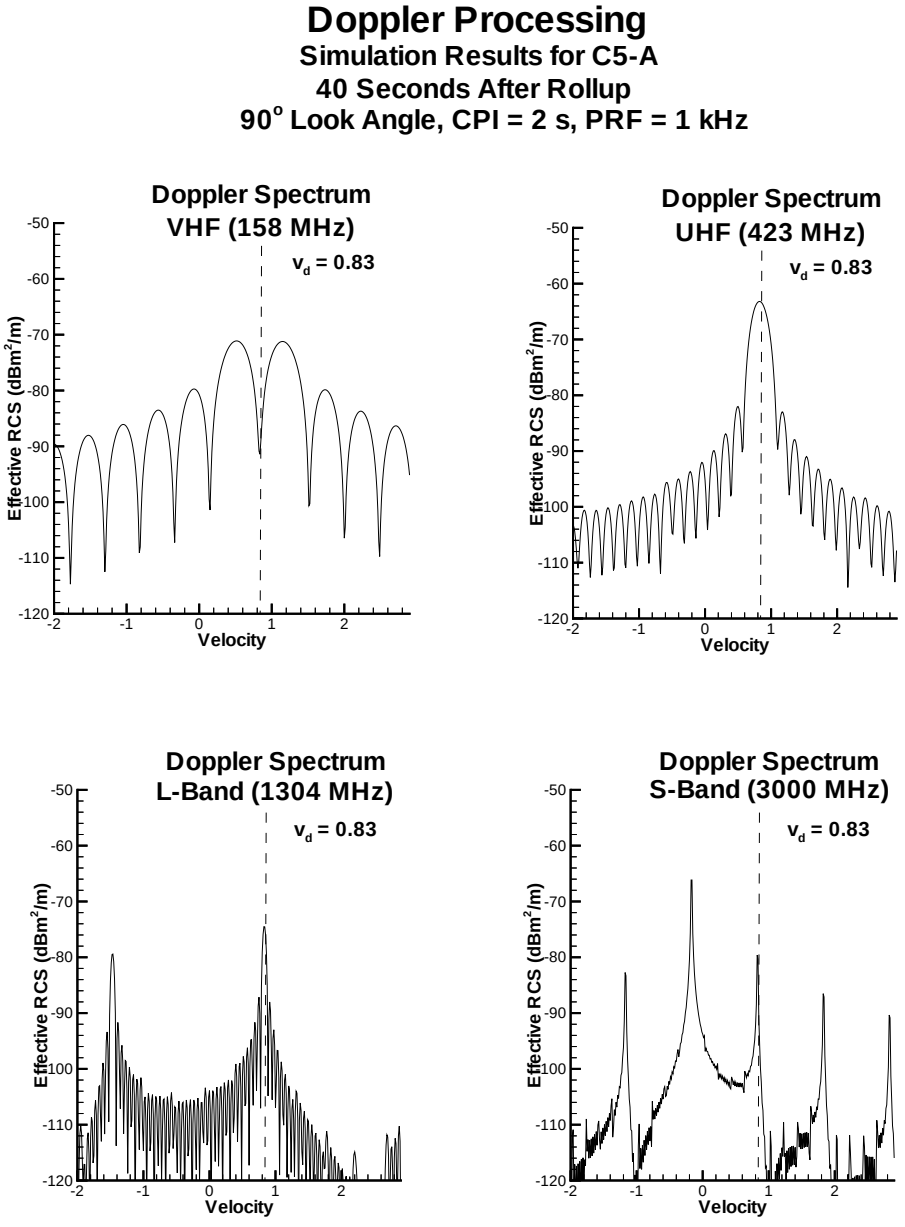

Figure 6.5: Doppler Processing for C-5A, 90^o Look Angle, 40 Seconds

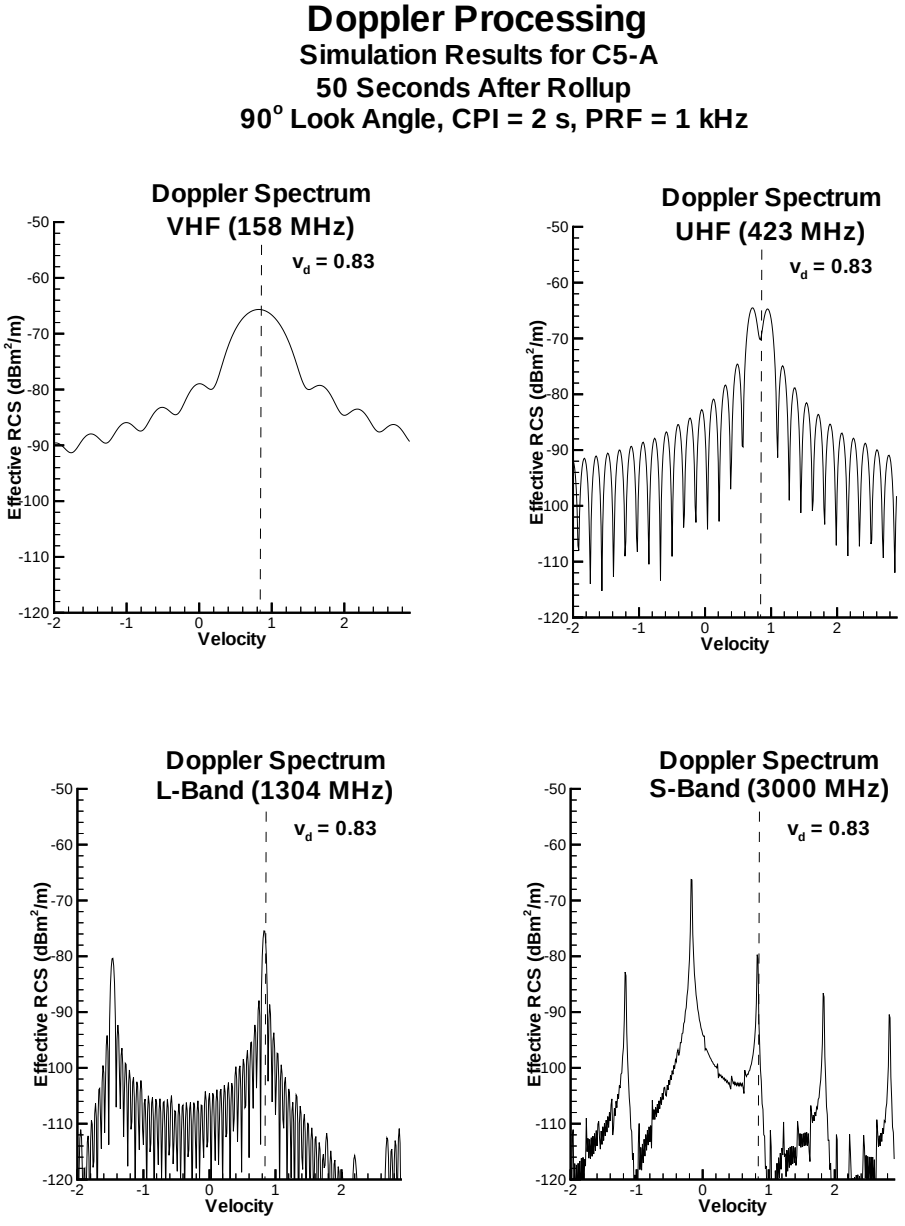

Figure 6.6: Doppler Processing for C-5A, 90^o Look Angle, 50 Seconds

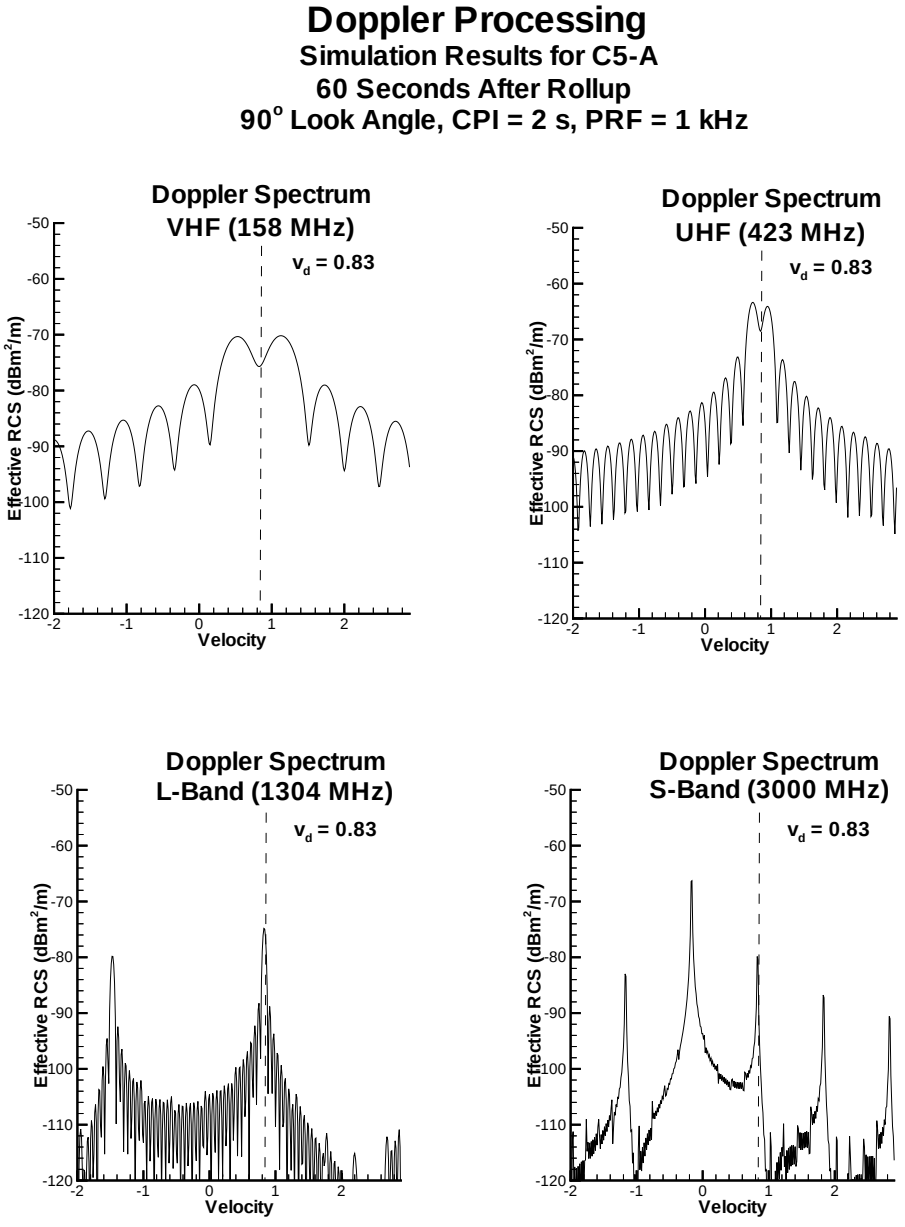

Figure 6.7: Doppler Processing for C-5A, 90^o Look Angle, 60 Seconds

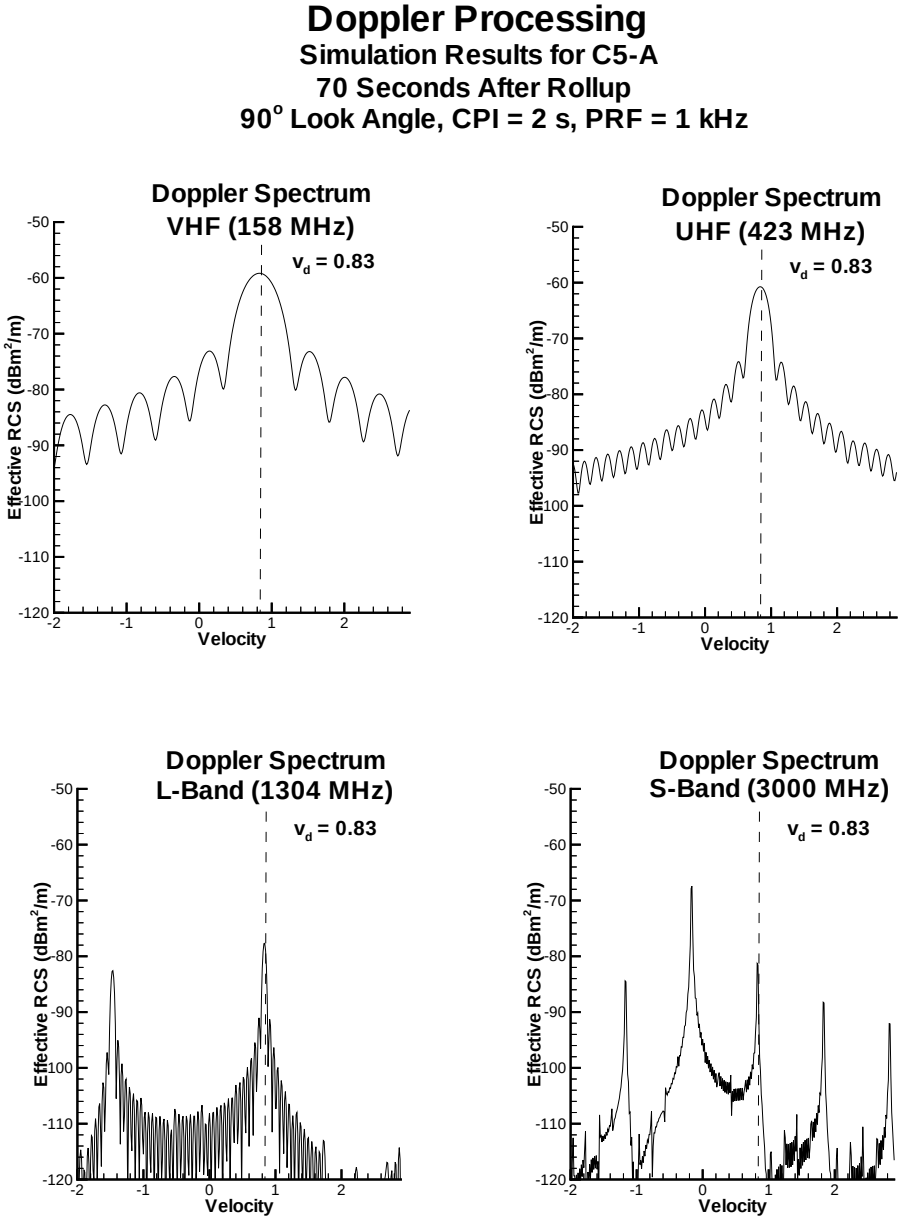

Figure 6.8: Doppler Processing for C-5A, 90^o Look Angle, 70 Seconds

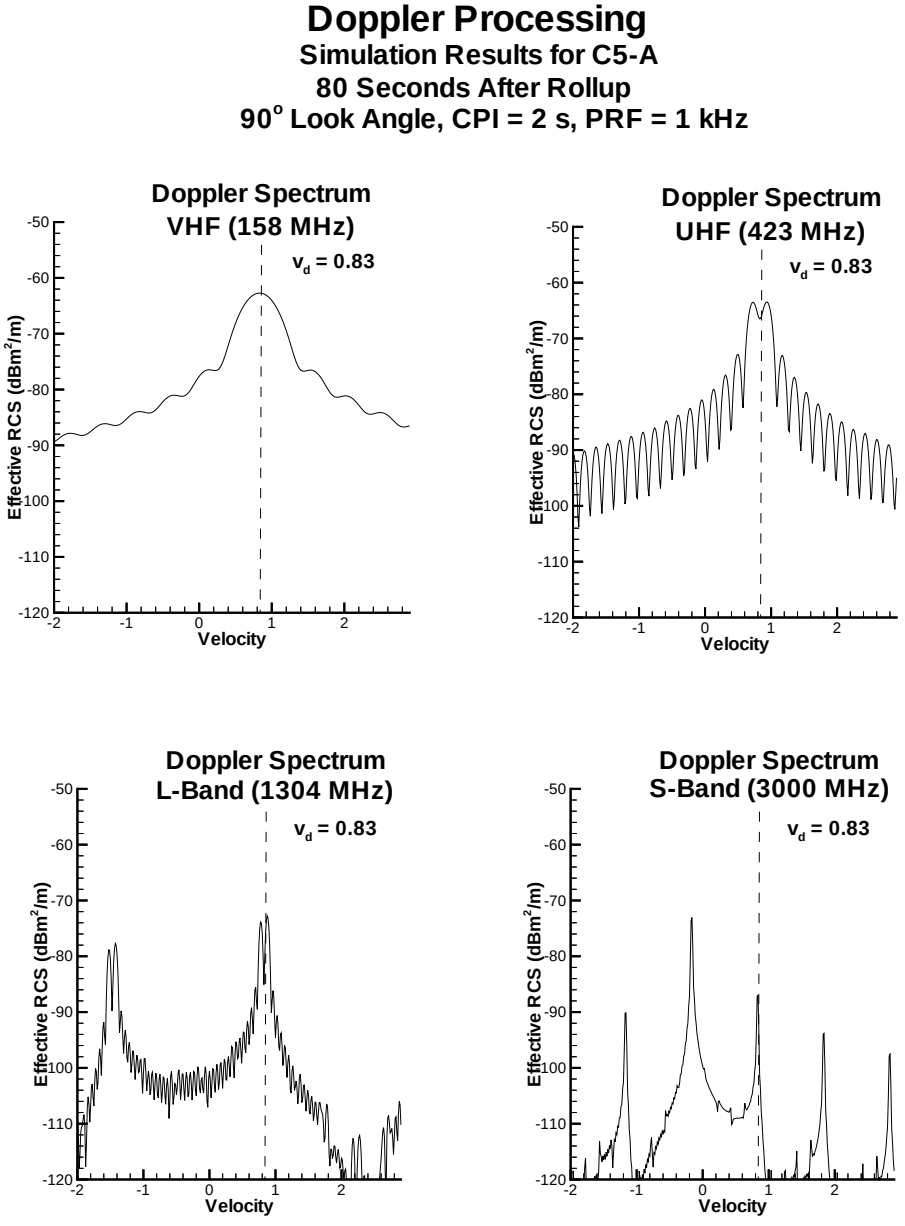

Figure 6.9: Doppler Processing for C-5A, 90^o Look Angle, 80 Seconds

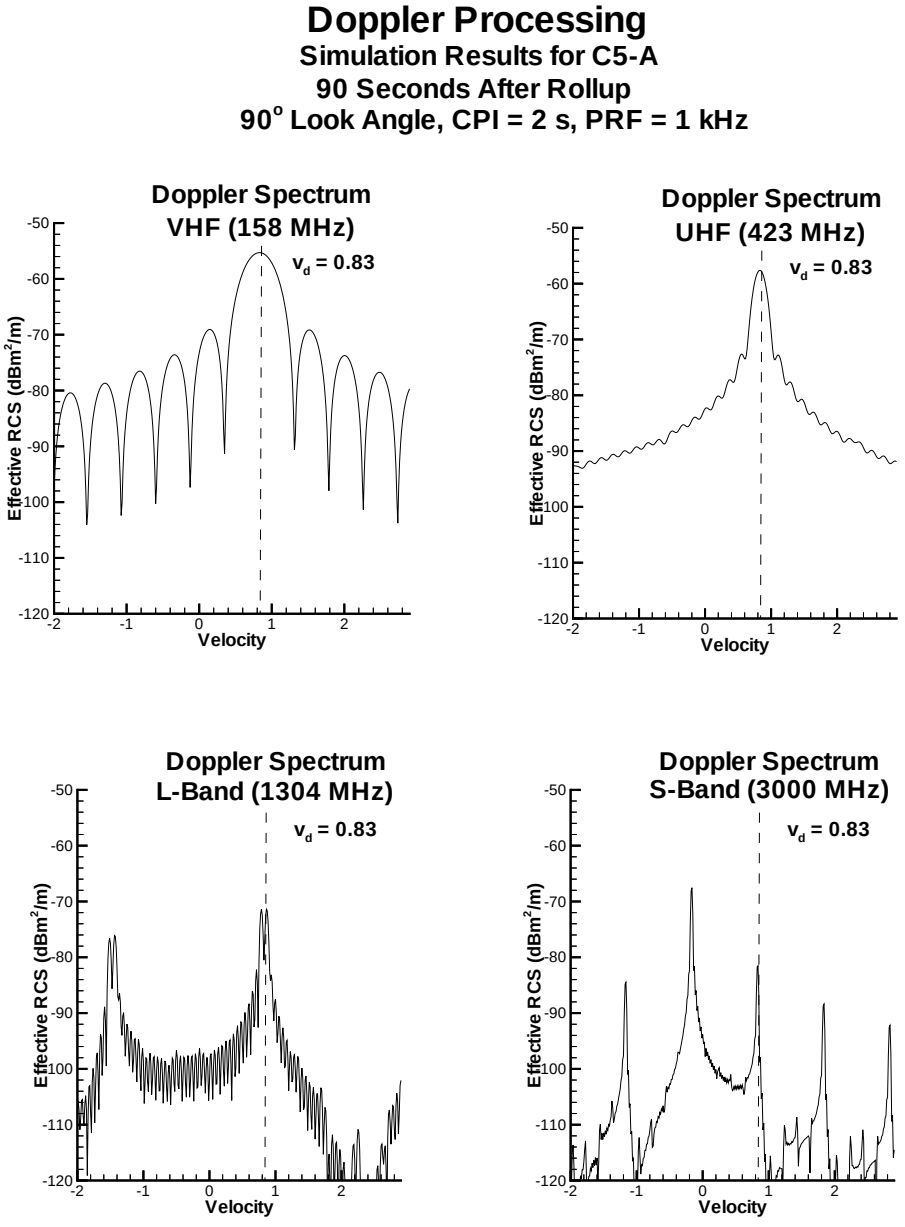

Figure 6.10: Doppler Processing for C-5A, 90^o Look Angle, 90 Seconds

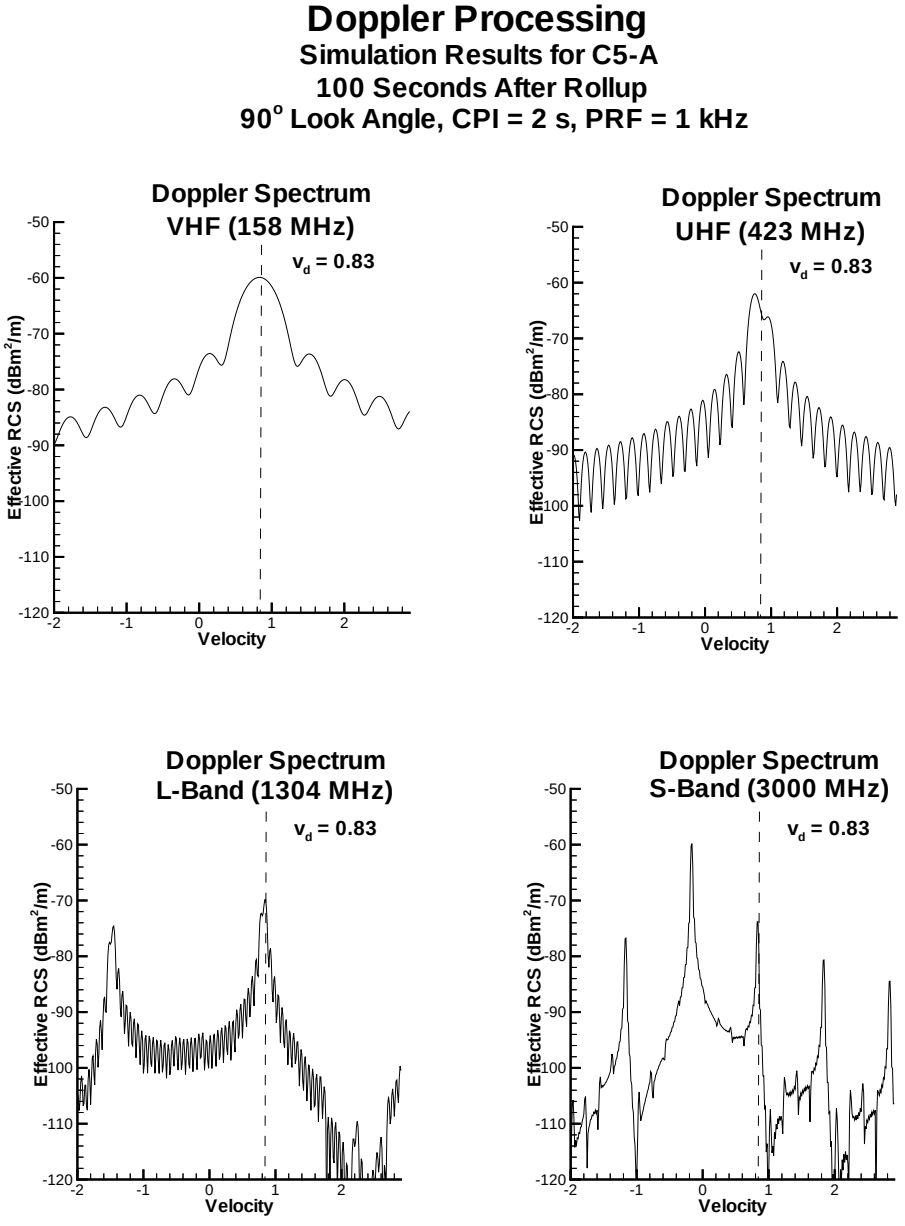

Figure 6.11: Doppler Processing for C-5A, 90^o Look Angle, 100 Seconds

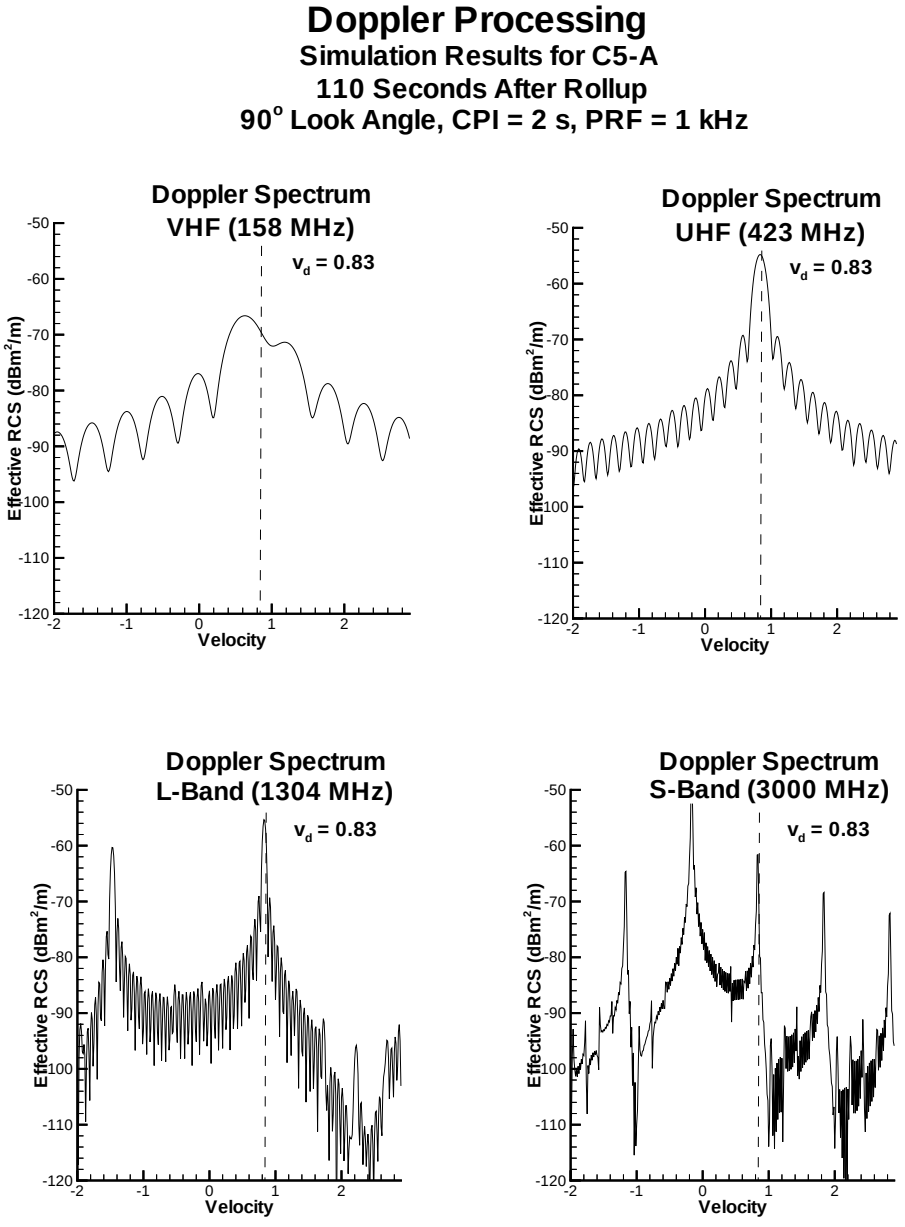

Figure 6.12: Doppler Processing for C-5A, 90^o Look Angle, 110 Seconds

0^o Look Angle

Figures 6.13 through 6.23 are analogous to Figures 6.2 through 6.12 with the different look angle of 0^o. The most noticeable difference is these figures is that the spectra are centered around a doppler velocity of 0 m/s. This is because the component of velocity of the wake vortex system is downward which is orthogonal to the direction of the look angle. Thus, there is no component of wake vortex system motion towards the radar and this corresponds to no average doppler shift. Another noticeable difference is the relatively small effective RCS for the incoherent scatter. For example, Figure 6.13 shows incoherent scatter at VHF, UHF, L-Band, and S-Band at 10 seconds after rollup. In each of these, the peak effective RCS is approximately 10 dB lower than that of the 90^o look angle shown in Figure 6.2. This is a reflection of the fact that the single pulse RCS is 10 dB lower at 0^o and is not related to different doppler processing enhancements at the two look angles. At the time and frequency bands where coherent scattering dominates, the effective RCS has approximately the same peak and spectral width with the most noticeable difference being the doppler velocity that the spectrum is centered around.

It is important to note that the WV-PCS did not contain a cross wind. If in the actual situation of a wake vortex being released in a cross wind, the 90^o spectrum would not change because there is no component of cross wind in the vertical direction. The 0^o look angle spectrum, however, would be uniformly upshifted or downshifted (depending upon the direction of the wind) by the component of wind velocity in the radar radial direction. For angles between 0^o and 90^o, the wind velocity and the descent rate would need to be added vectorally the summed velocity component in the radial direction to the radar would be the expected velocity where the peak effective RCS would be located. The full expression for the velocity where the doppler power would be centered around for an arbitrary look angle would be

$$v_c = v_d \sin\theta + v_c \cos\theta \tag{6.17}$$

where v_c is the doppler velocity to which the doppler processor should be tuned, v_d is the descent rate of the wake vortex system, v_c is the cross wind speed, and θ is the look angle.

Doppler processing is quite useful to eliminate ground clutter that lies in a different velocity region than the target. From this perspective, the 0^o effective RCS is the absence of cross wind has the disadvantage that the effective RCS peaks around 0 m/s which is also where the majority of ground clutter peaks. Thus, doppler processing does not help eliminate the adverse effects of ground clutter in this situation. At 90^o look angle, the ground clutter would need to extend to the descent rate of the wake vortex system to have adverse effects on the wake vortex detection. There are situations where the ground clutter would not extend that far.

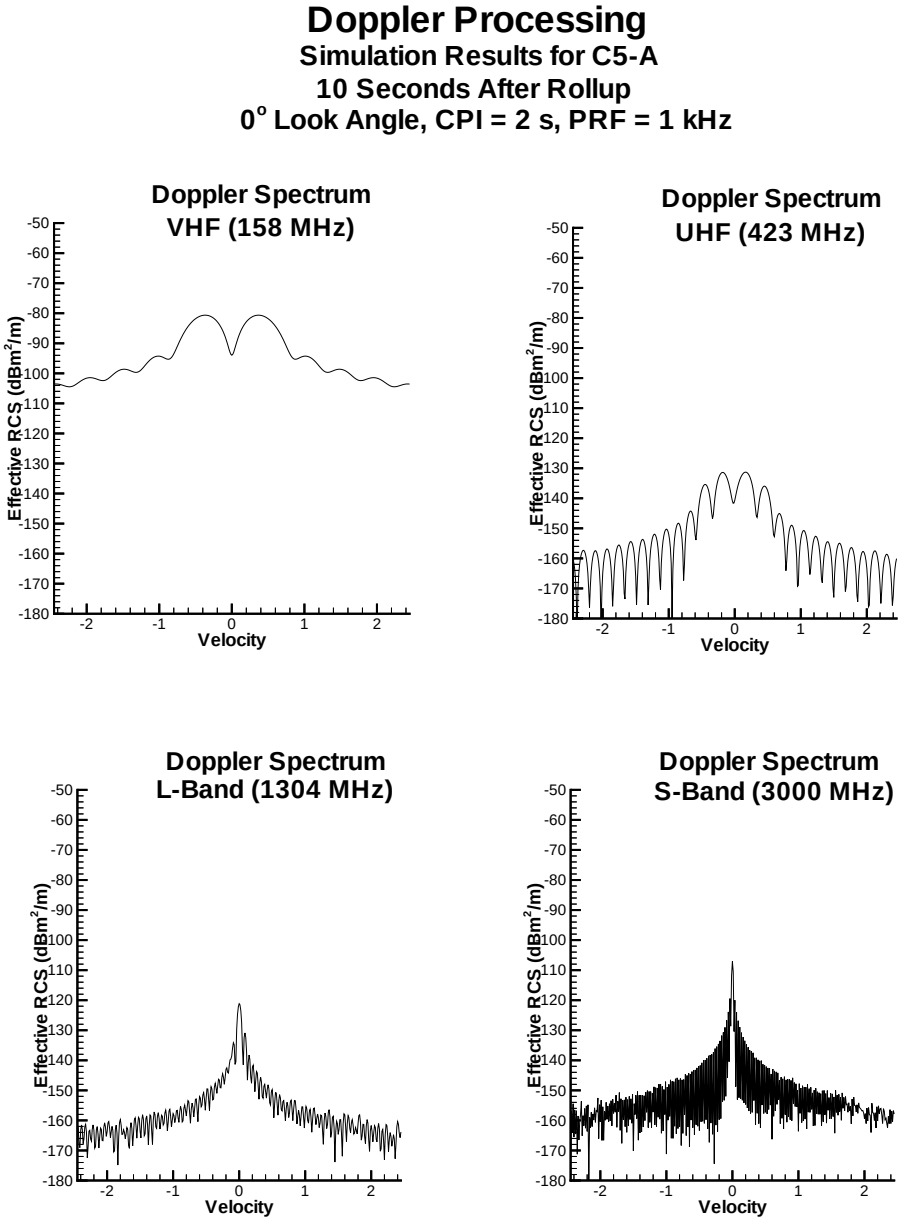

Figure 6.13: Doppler Processing for C-5A, 0^o Look Angle, 10 Seconds

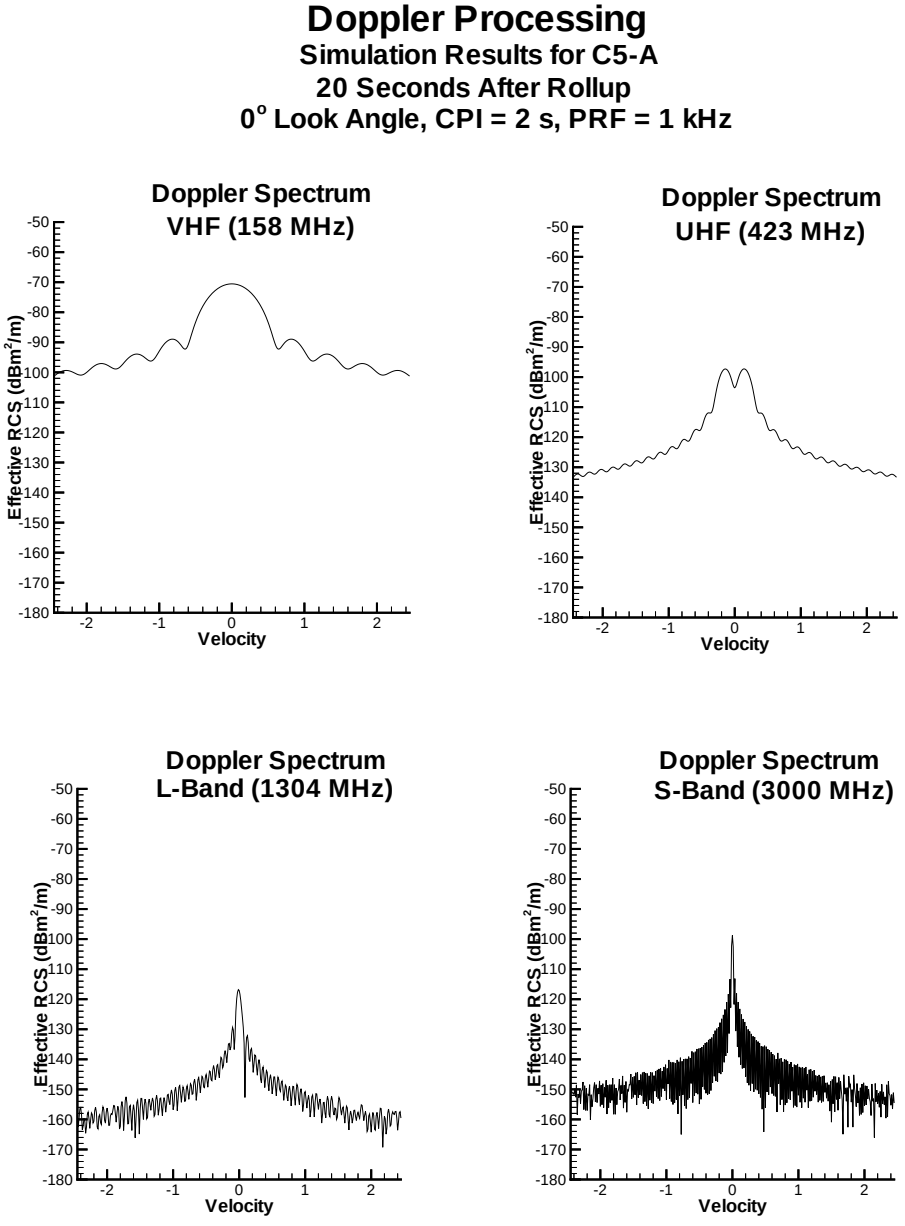

Figure 6.14: Doppler Processing for C-5A, 0^o Look Angle, 20 Seconds

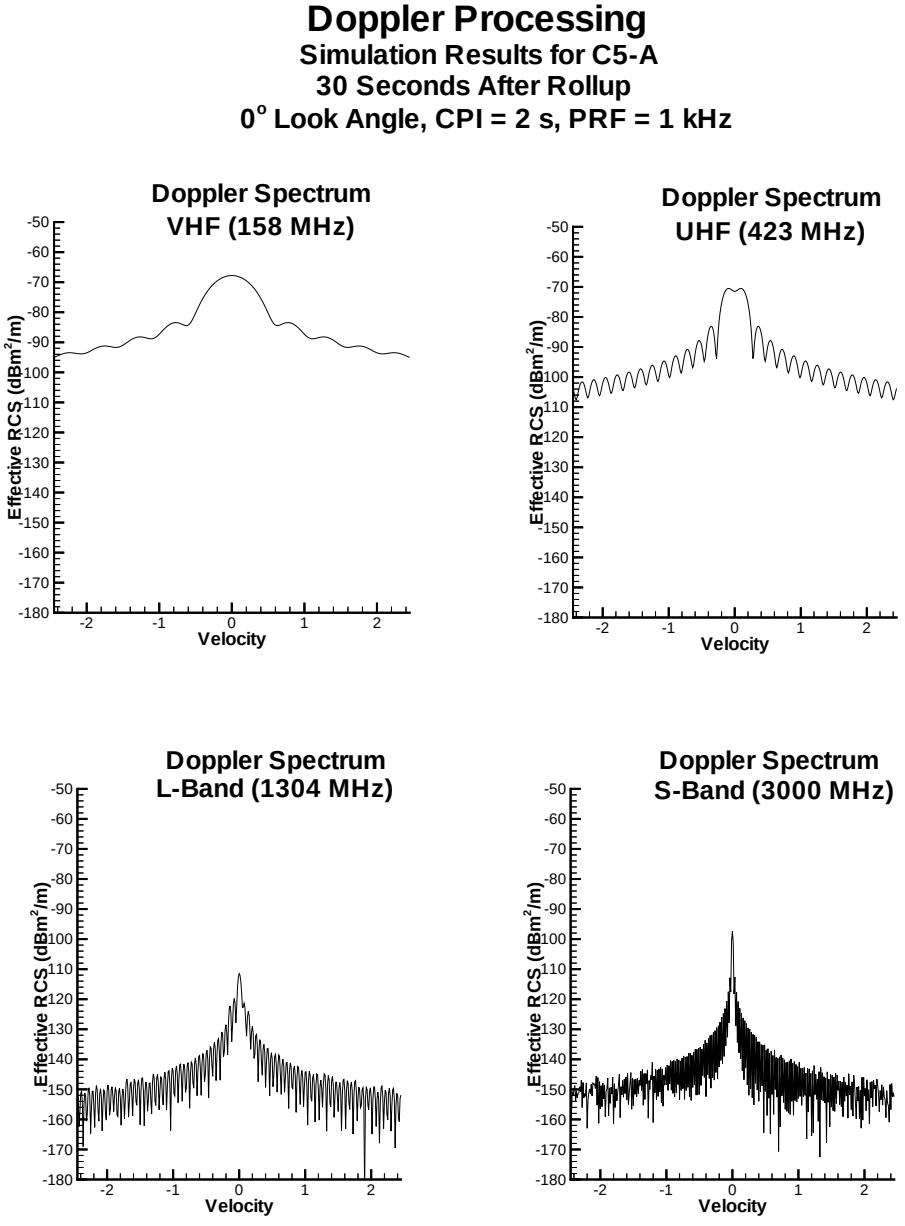

Figure 6.15: Doppler Processing for C-5A, 0^o Look Angle, 30 Seconds

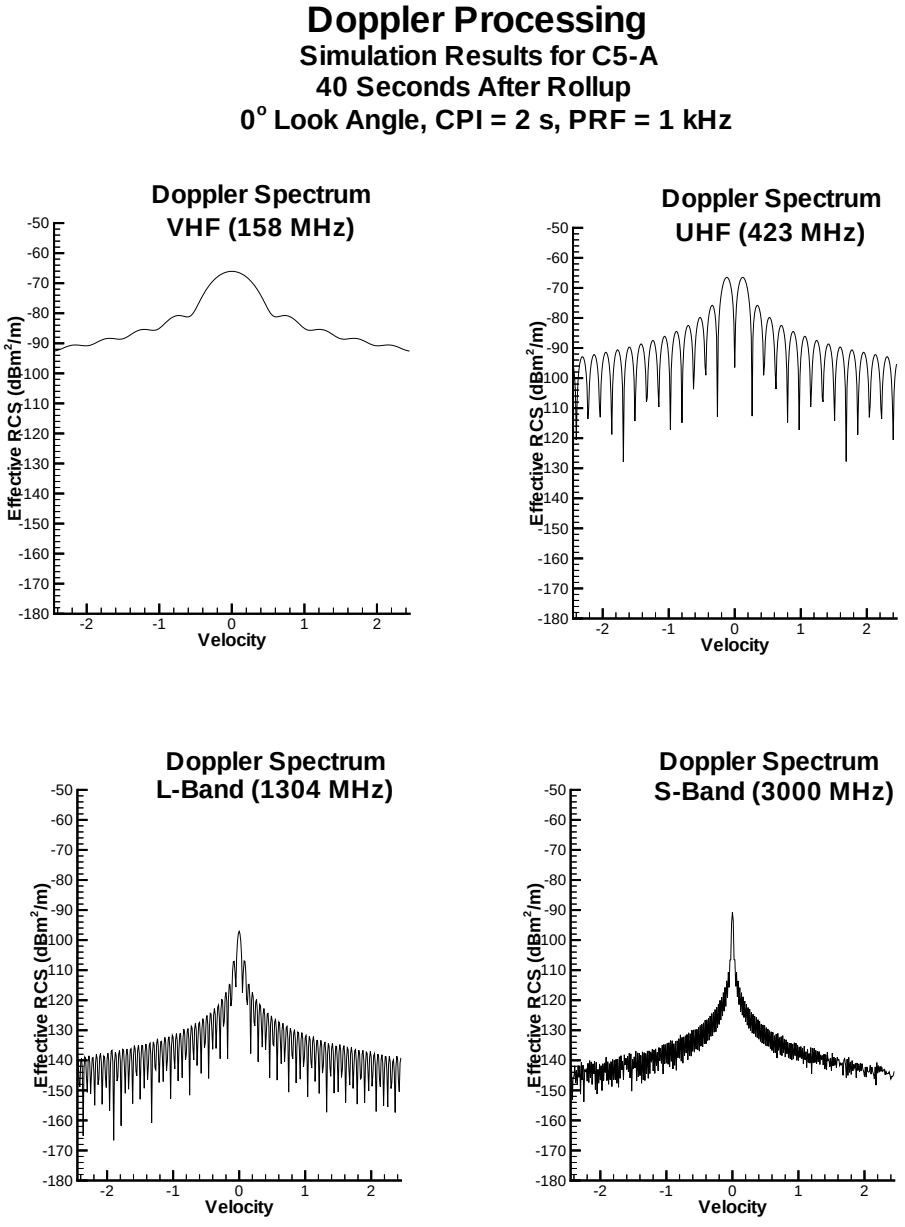

Figure 6.16: Doppler Processing for C-5A, 0^o Look Angle, 40 Seconds

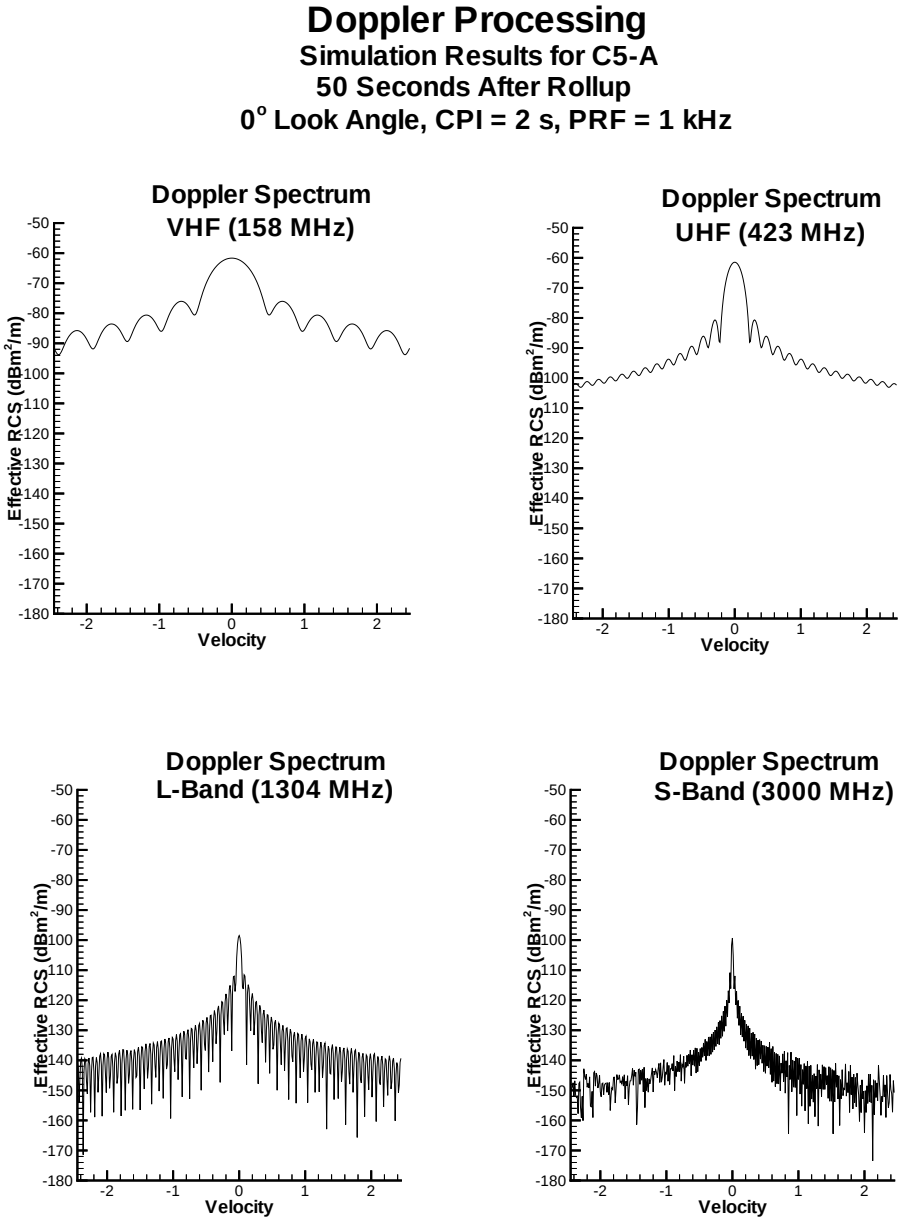

Figure 6.17: Doppler Processing for C-5A, 0^o Look Angle, 50 Seconds

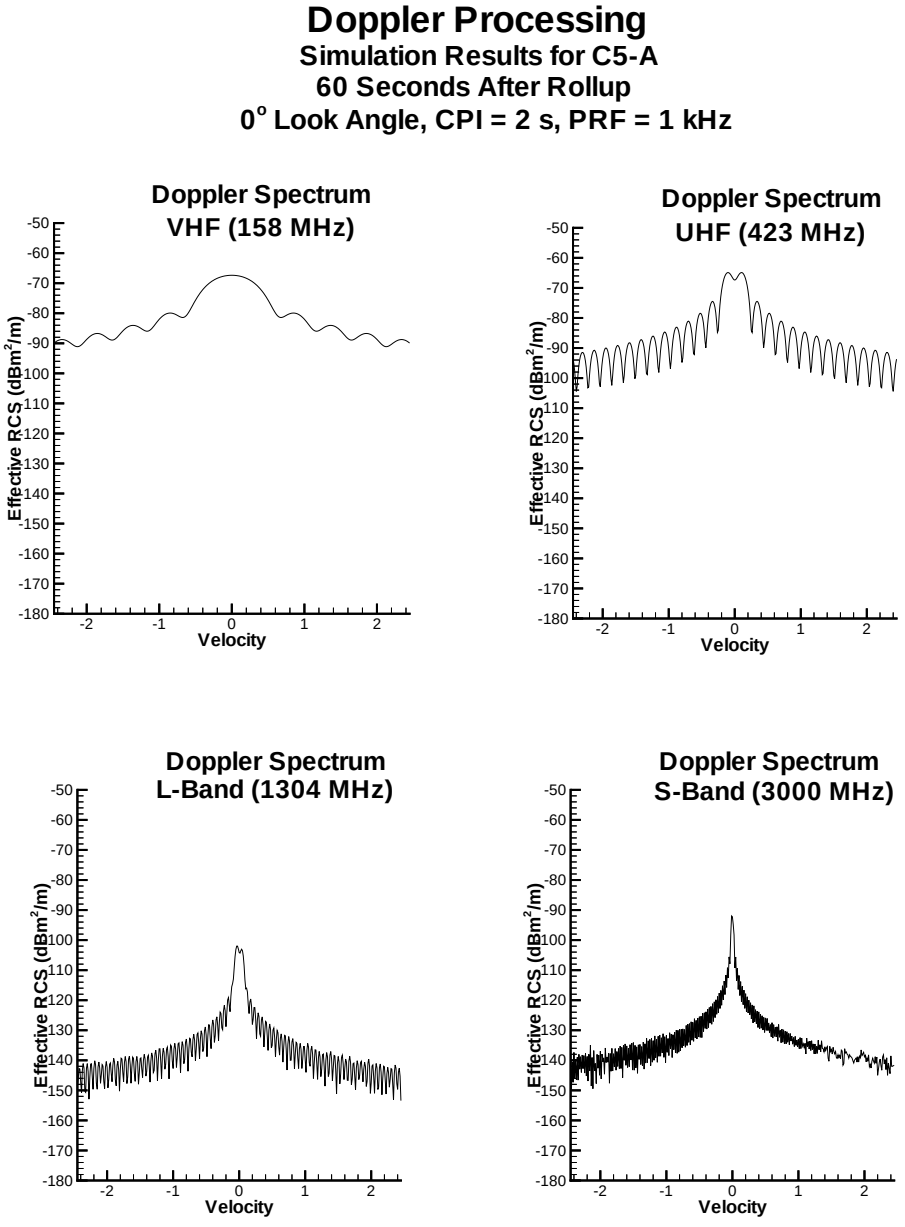

Figure 6.18: Doppler Processing for C-5A, 0^o Look Angle, 60 Seconds

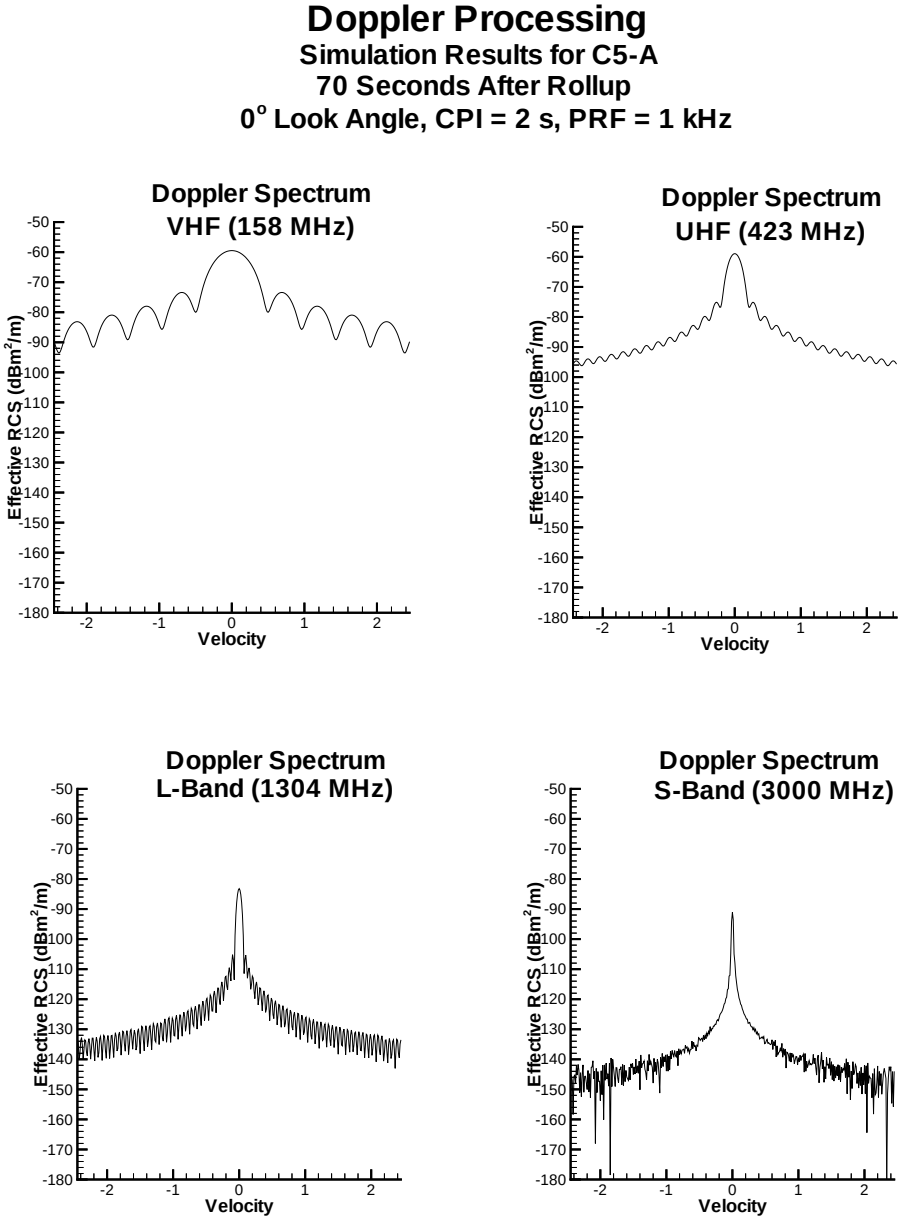

Figure 6.19: Doppler Processing for C-5A, 0^o Look Angle, 70 Seconds

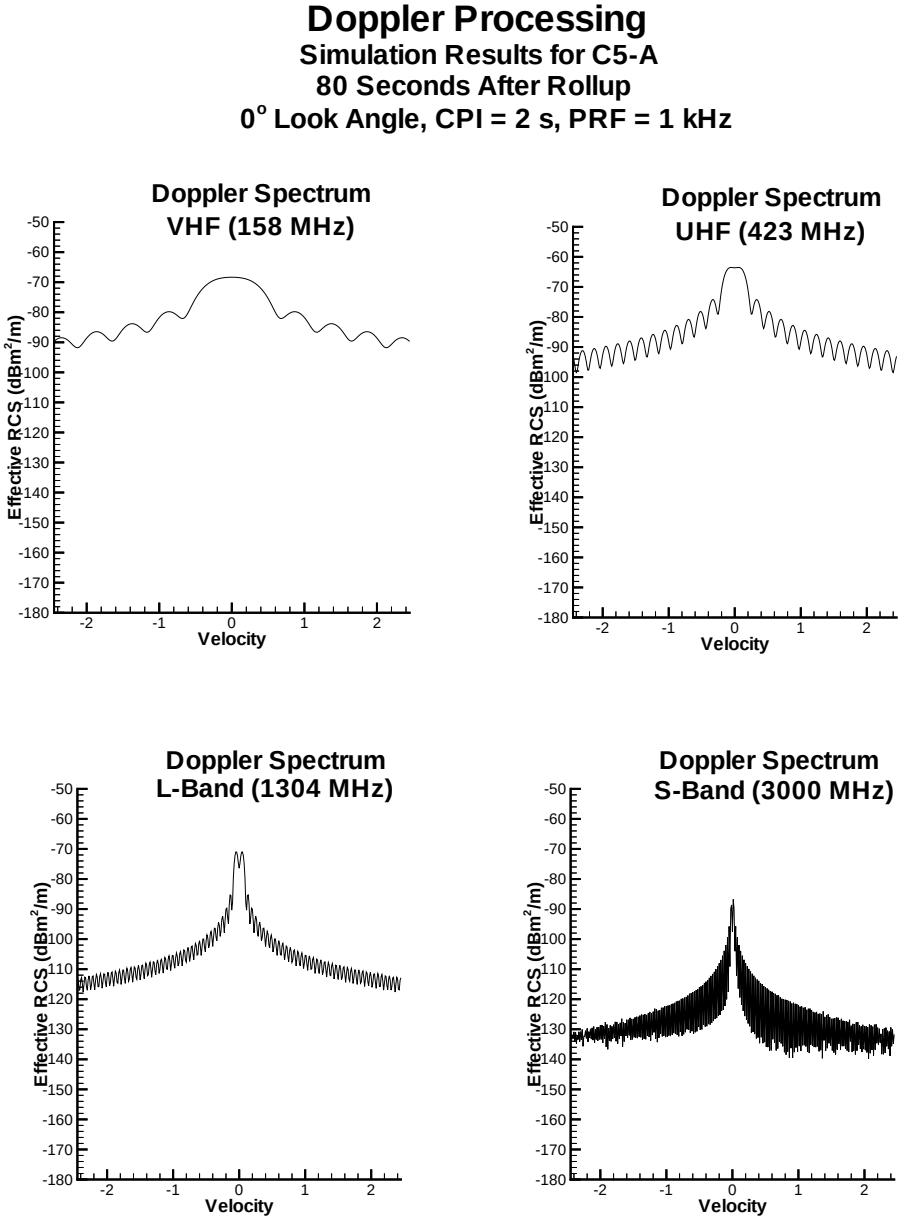

Figure 6.20: Doppler Processing for C-5A, 0^o Look Angle, 80 Seconds

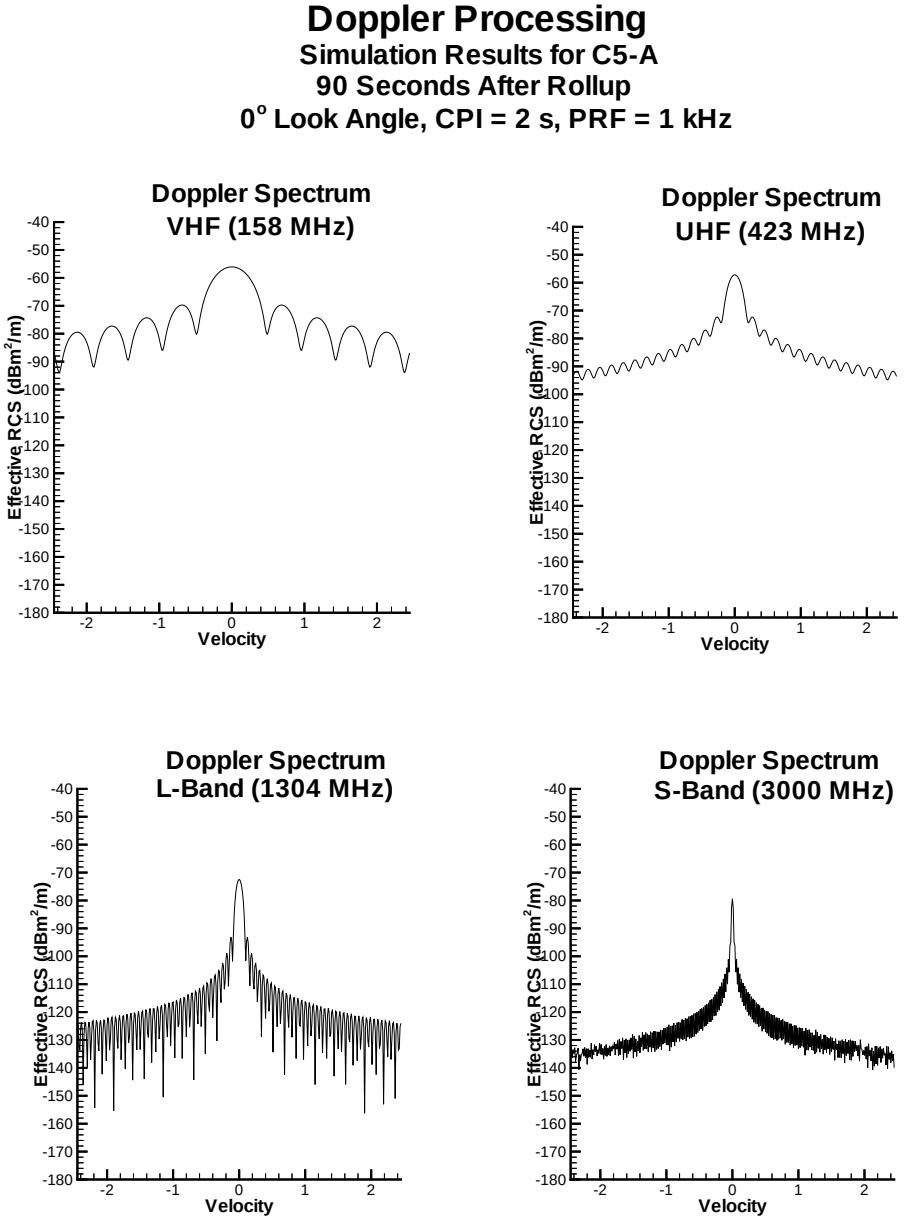

Figure 6.21: Doppler Processing for C-5A, 0^o Look Angle, 90 Seconds

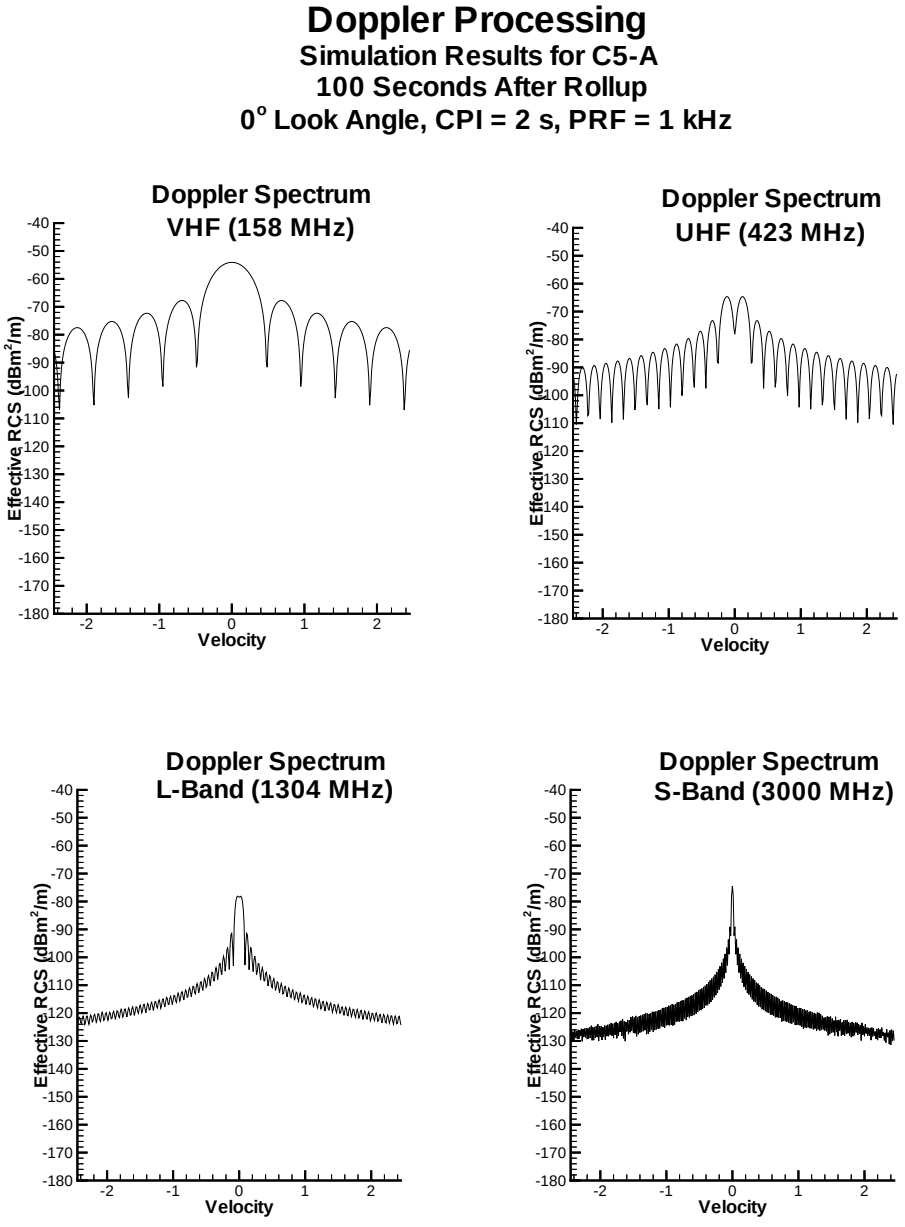

Figure 6.22: Doppler Processing for C-5A, 0^o Look Angle, 100 Seconds

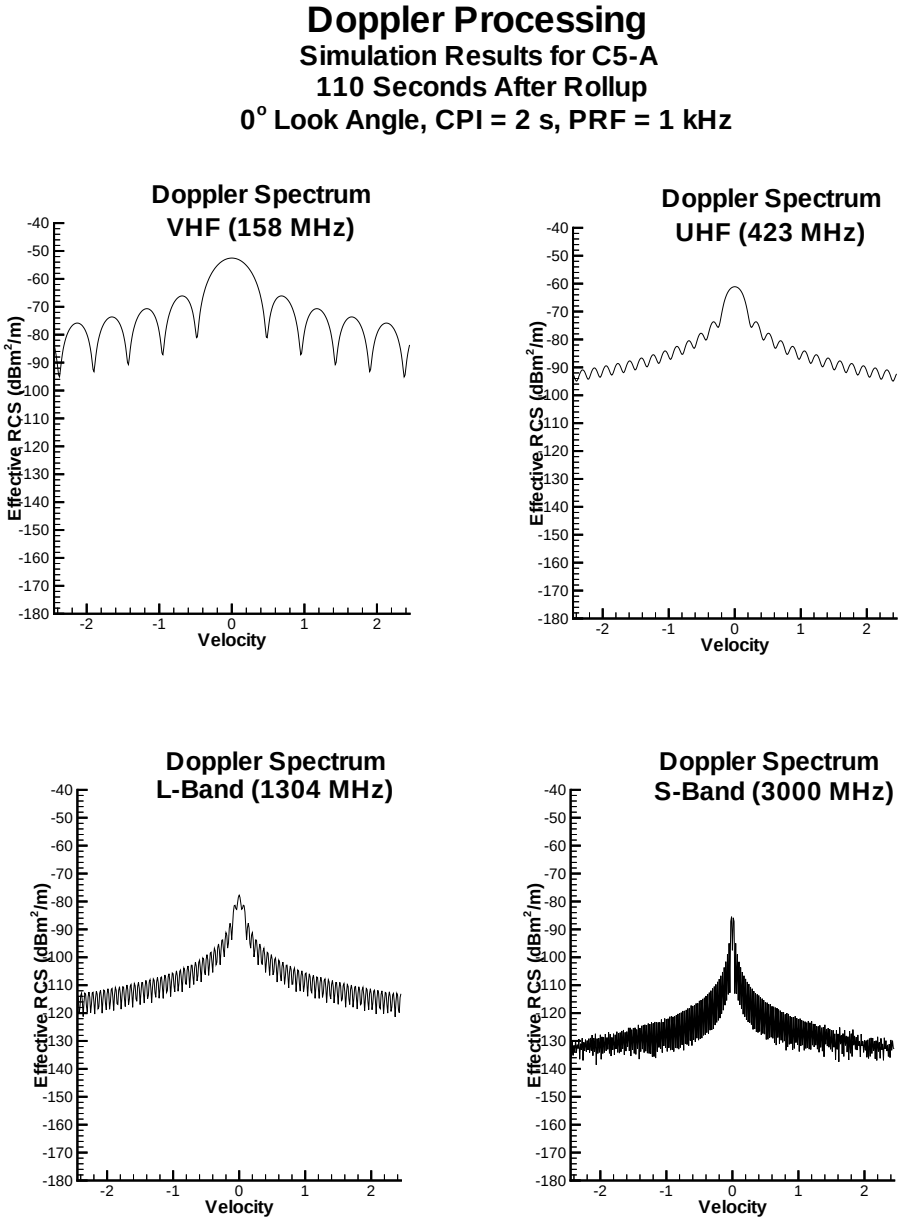

Figure 6.23: Doppler Processing for C-5A, 0^o Look Angle, 110 Seconds

6.2.2 747

The doppler spectrum of the 747 is shown in Figures 6.24 to 6.30 for the 90^o look angle. The selected coherent processing interval (CPI) was 0.75 seconds and was where the effective RCS saturated (see Section 6.3). The pulse repetition frequency (PRF) was 1 kHz.

The evolution of the doppler spectrum follows that of the C5-A very closely with the exception that the time for effective RCS to develop is scaled by a factor of approximately 3/8. In addition, the maximum effective RCS is diminished by the same factor of 3/8 because there is proportionally less time to coherently sum the return pulses.

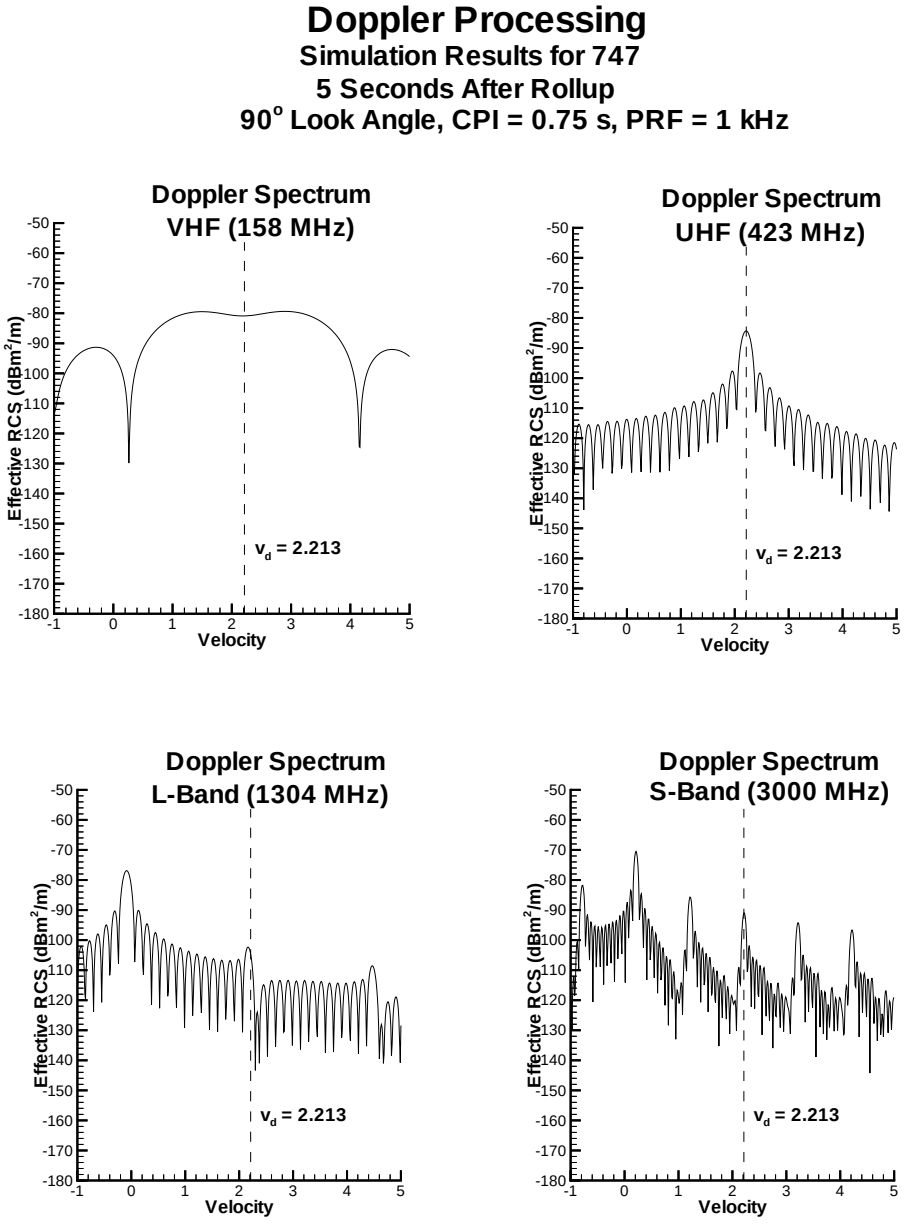

Figure 6.24: Doppler Processing for 747, 90^o Look Angle, 5 Seconds

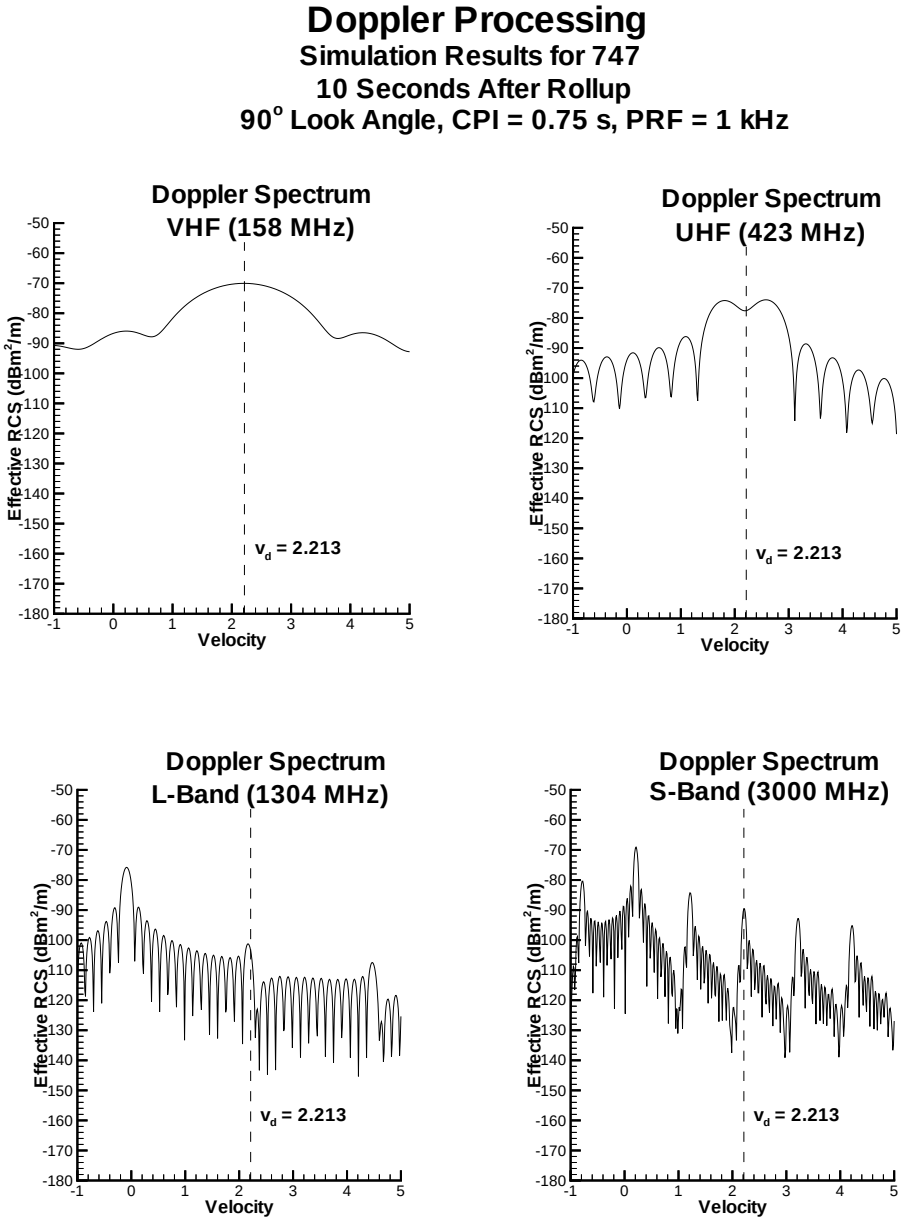

Figure 6.25: Doppler Processing for 747, 90^o Look Angle, 10 Seconds

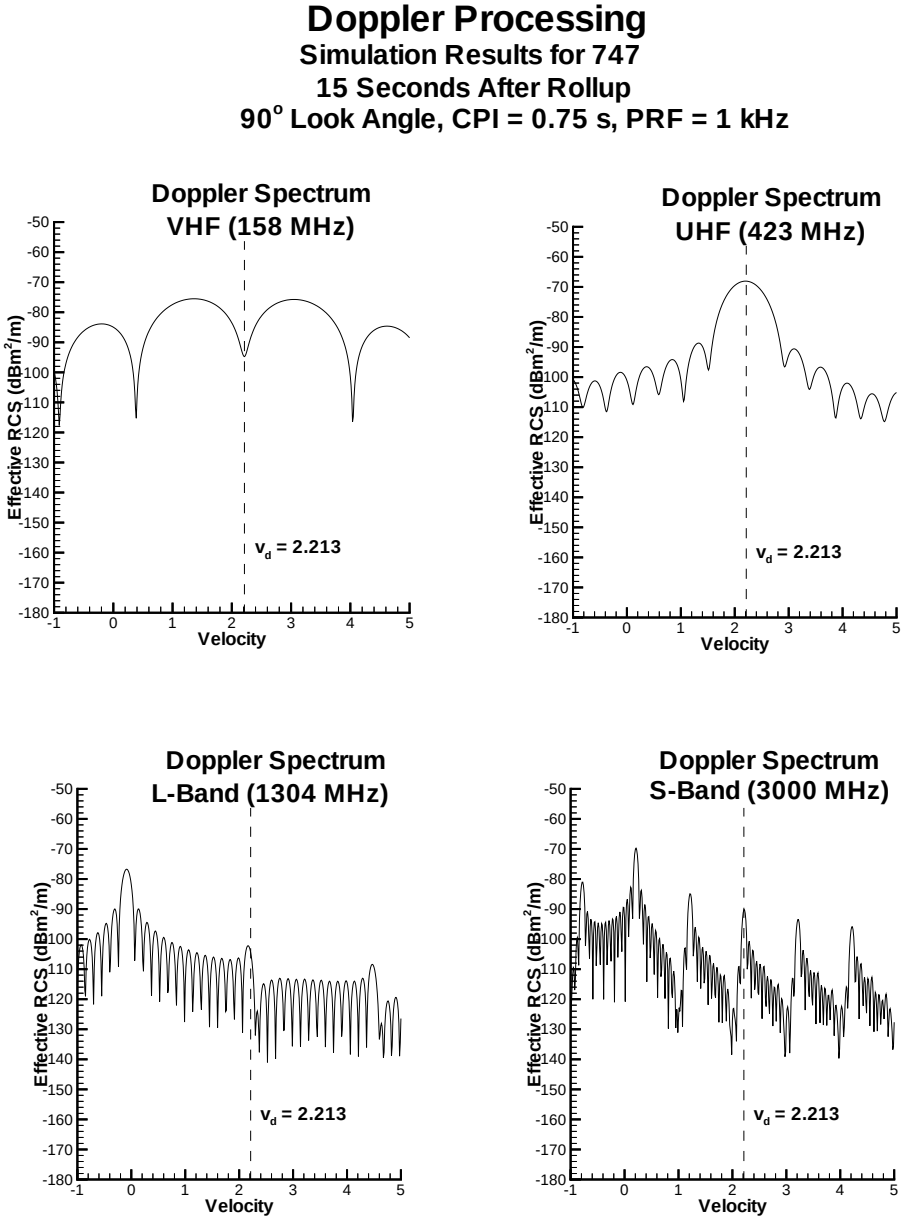

Figure 6.26: Doppler Processing for 747, 90^o Look Angle, 15 Seconds

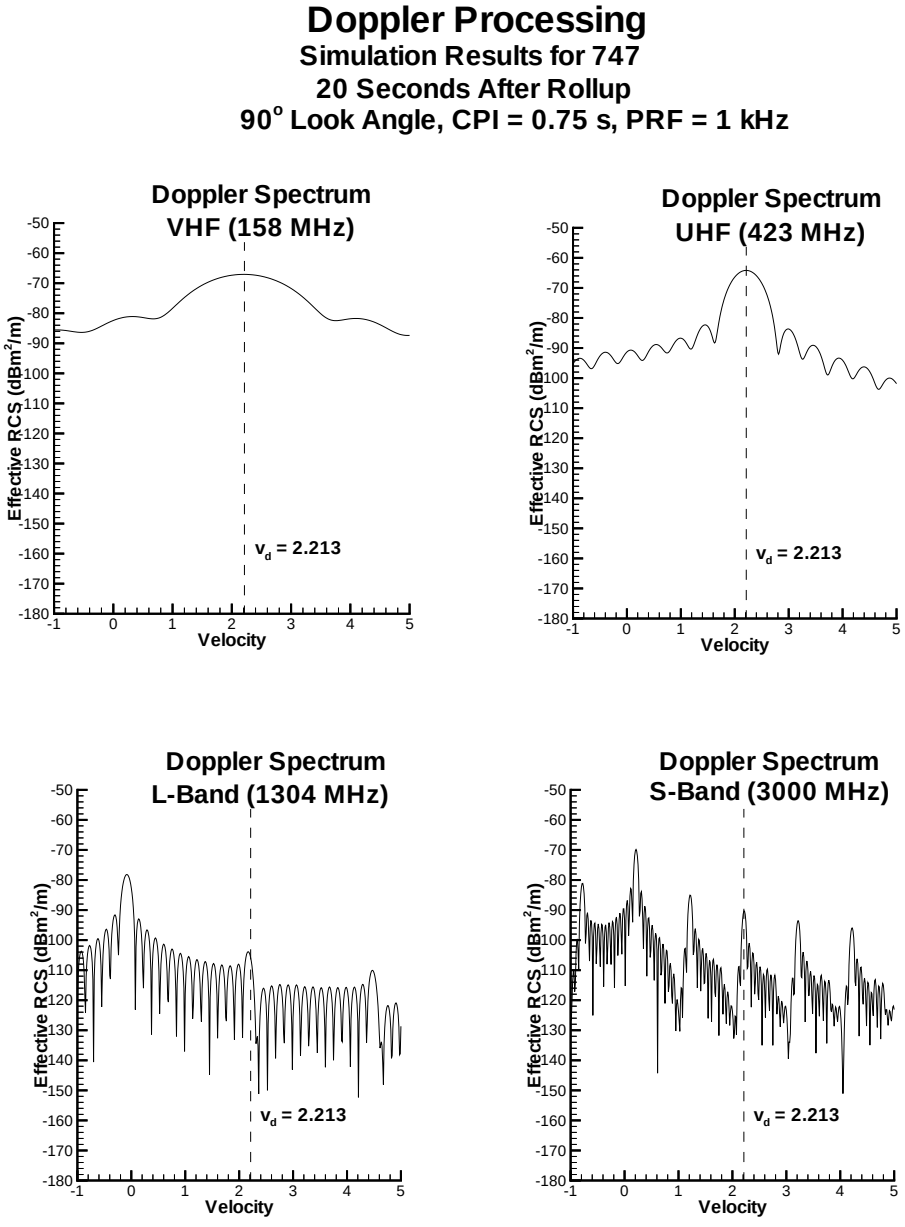

Figure 6.27: Doppler Processing for 7476, 90^o Look Angle, 20 Seconds

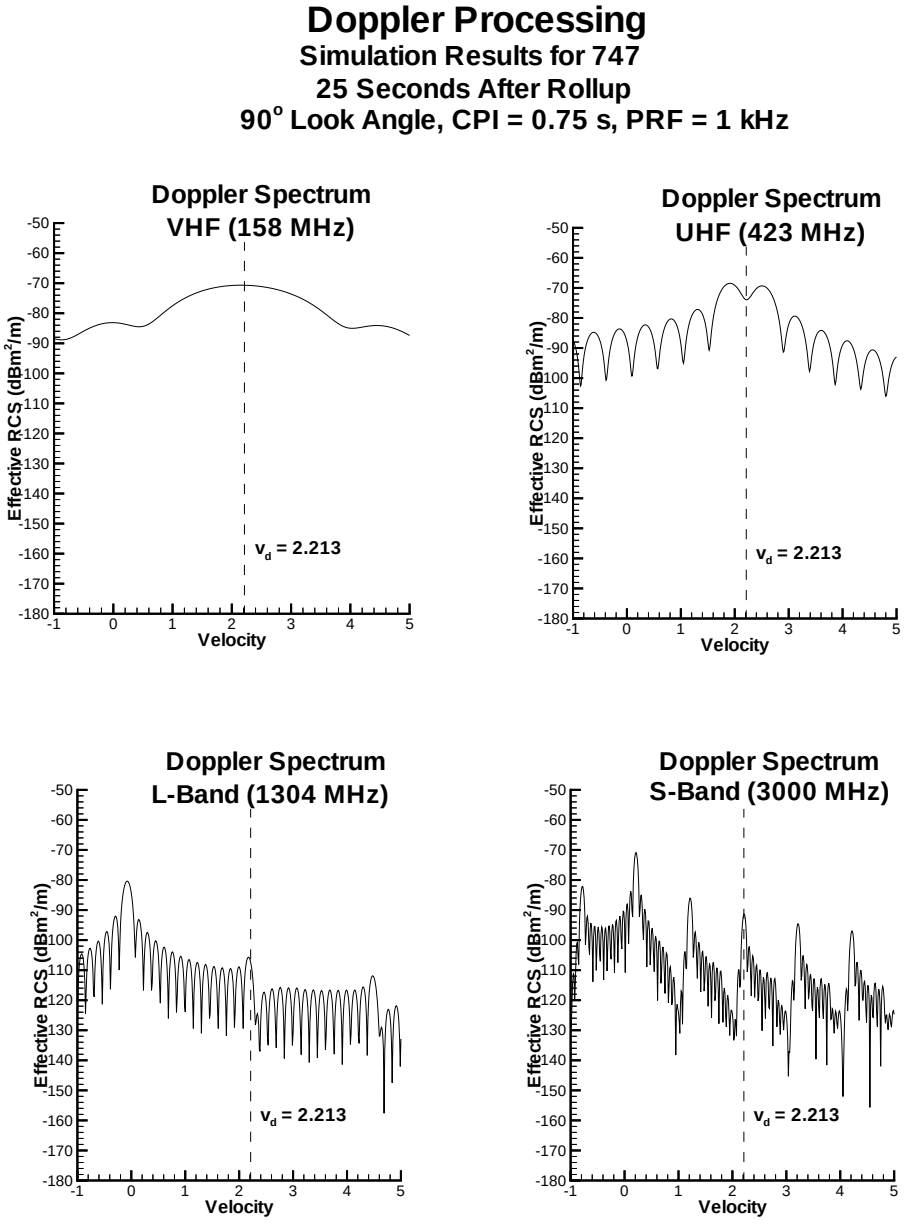

Figure 6.28: Doppler Processing for 747, 90^o Look Angle, 25 Seconds

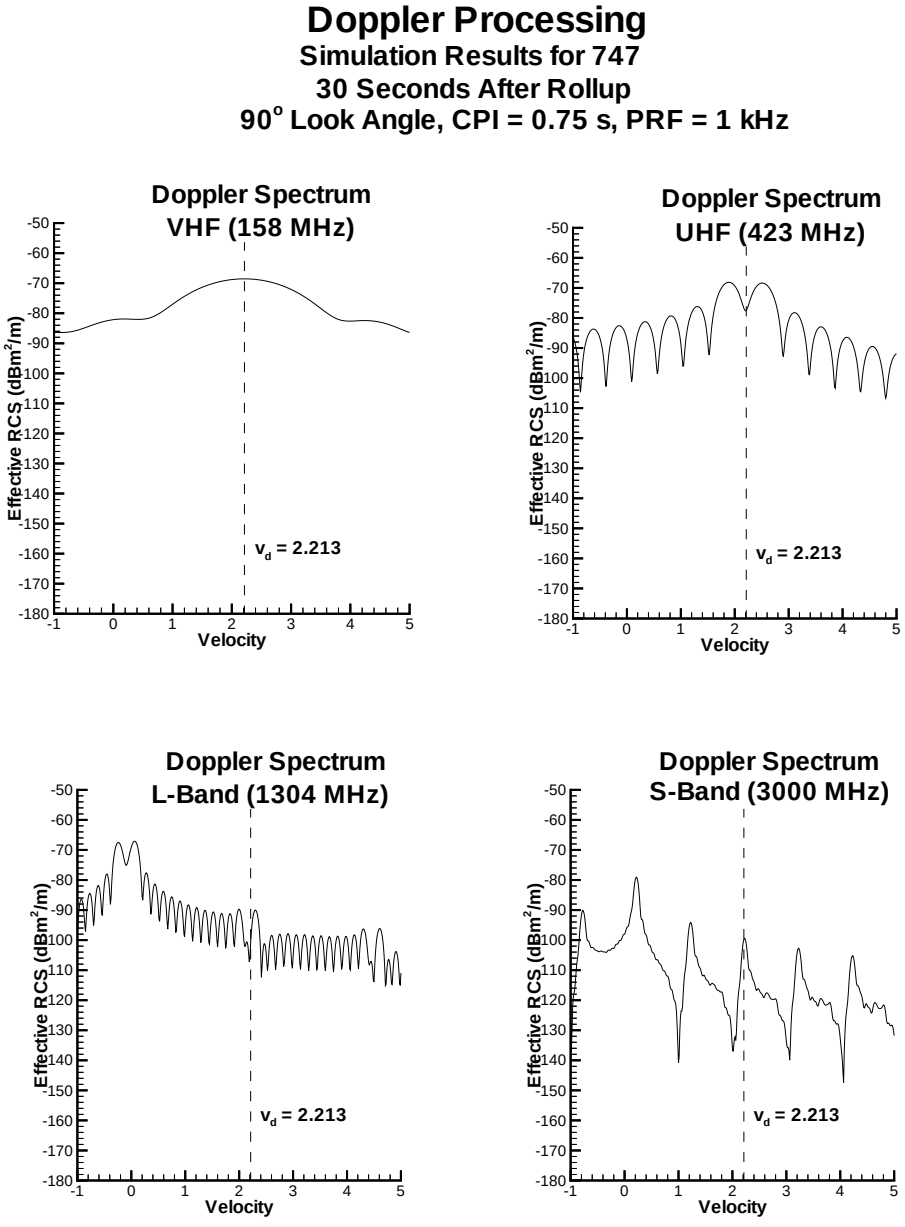

Figure 6.29: Doppler Processing for 747, 90^o Look Angle, 30 Seconds

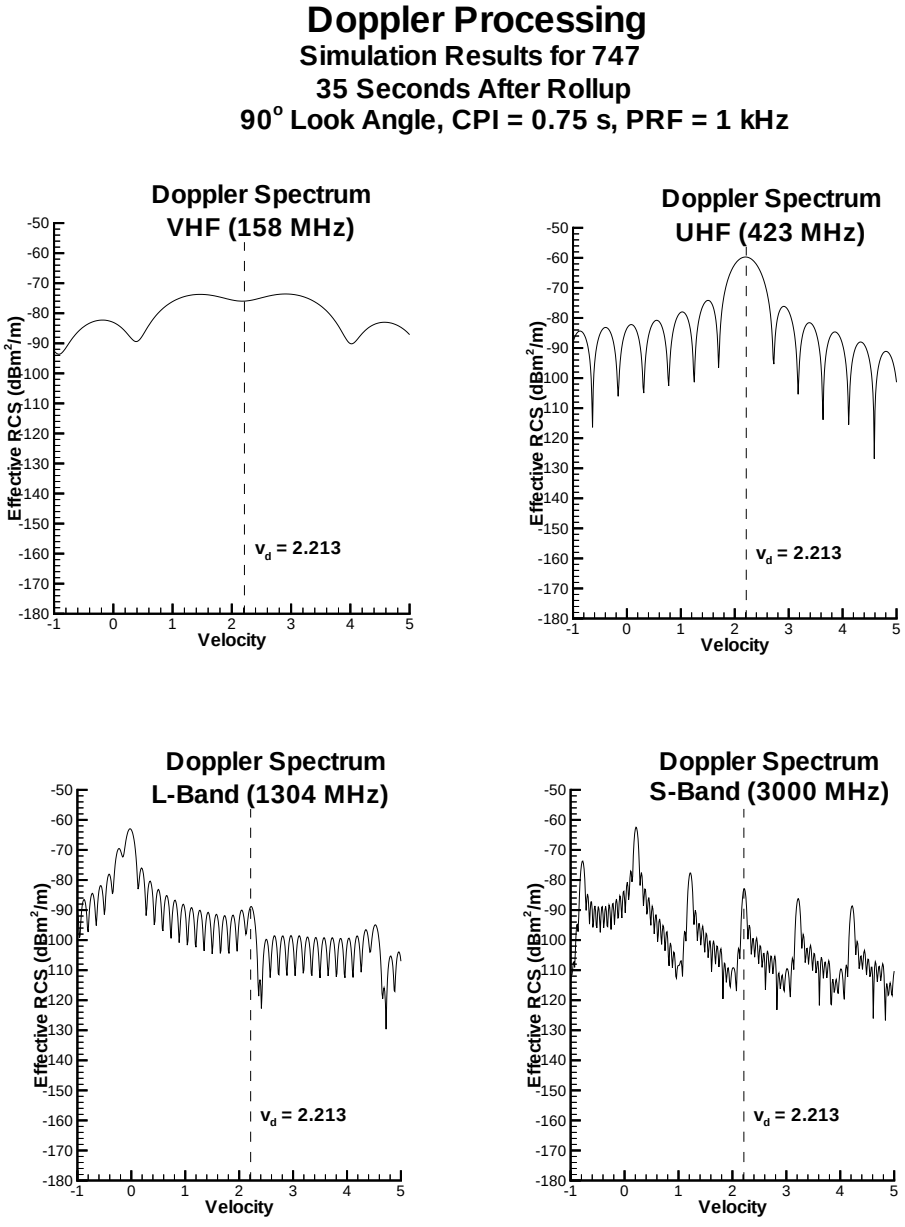

Figure 6.30: Doppler Processing for 747, 90^o Look Angle, 35 Seconds

6.3 Effect of Coherent Processing Interval (CPI)

An important factor in the design of the doppler processing algorithm is selection of the CPI. The coherent processing interval (CPI) is the period of coherent integration or the period of time that the pulses are weighted and summed. For a "hard" target such as an aircraft at a uniform velocity, the effective RCS would have a linear dependence on the CPI. For the wake vortex, however, the RCS eventually saturates with increasing CPI. Figure 6.31 shows the peak effective RCS as a function of CPI for the four frequency bands: VHF, UHF, L-Band, and S-Band. The look angle is 90^o, the PRF is 1 kHz, the wake vortex is generated by the C5-A, and the time after rollup is 100 seconds. The solid line represents the results of a "fixed" processing algorithm where the doppler processor looks at the frequency exactly corresponding to the descent rate of the wake vortex system. The "tunable" algorithm tracks the peak effective RCS within a small range around the descent velocity. Figures 6.32 through 6.35 shows the doppler spectrum at different CPI corresponding to the dotted lines in Figure 6.31. Note that the larger the CPI, the greater the peak and the smaller the width of the peak. This indicates that although more effective RCS comes with increasing the CPI, it is also more critical that the doppler processor be tuned to a more exacting frequency requirement. Figure 6.44 shows that the tunable doppler processing algorithm is advantageous because of the splitting effect of the effective RCS forming a local minimum at the descent velocity at a CPI of 2.65 seconds.

A CPI of 2 seconds seems like a good choice for all of the frequency bands where saturation is starting to begin for the C-5A. This can be extrapolated to the 747 by multiplication of the time scale factor of 3/8 as determined in Section 3.3.

It is important to realize that the doppler processing algorithm would need to be tunable in a practical implementation because the descent velocity is in reality, not entirely deterministic. A minute change in the descent velocity would (especially at higher frequency bands

and higher CPI) cause the effective RCS to reduce to up to 30 dB. Thus it is necessary to have a tunable algorithm such as a phase-lock-loop (PLL) that determines the doppler frequency in a closed-loop manner.

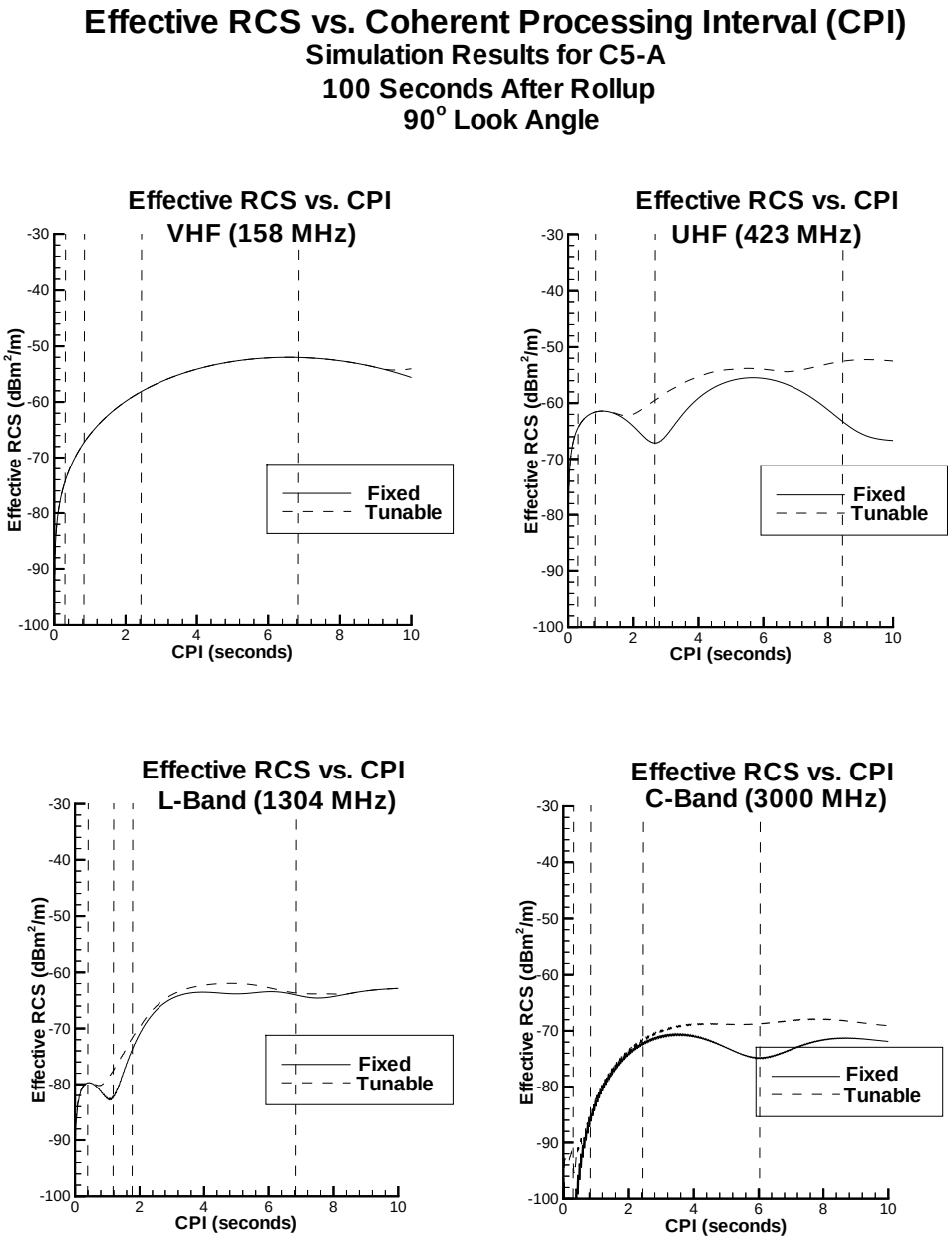

Figure 6.31: Peak Effective RCS as a Function of CPI

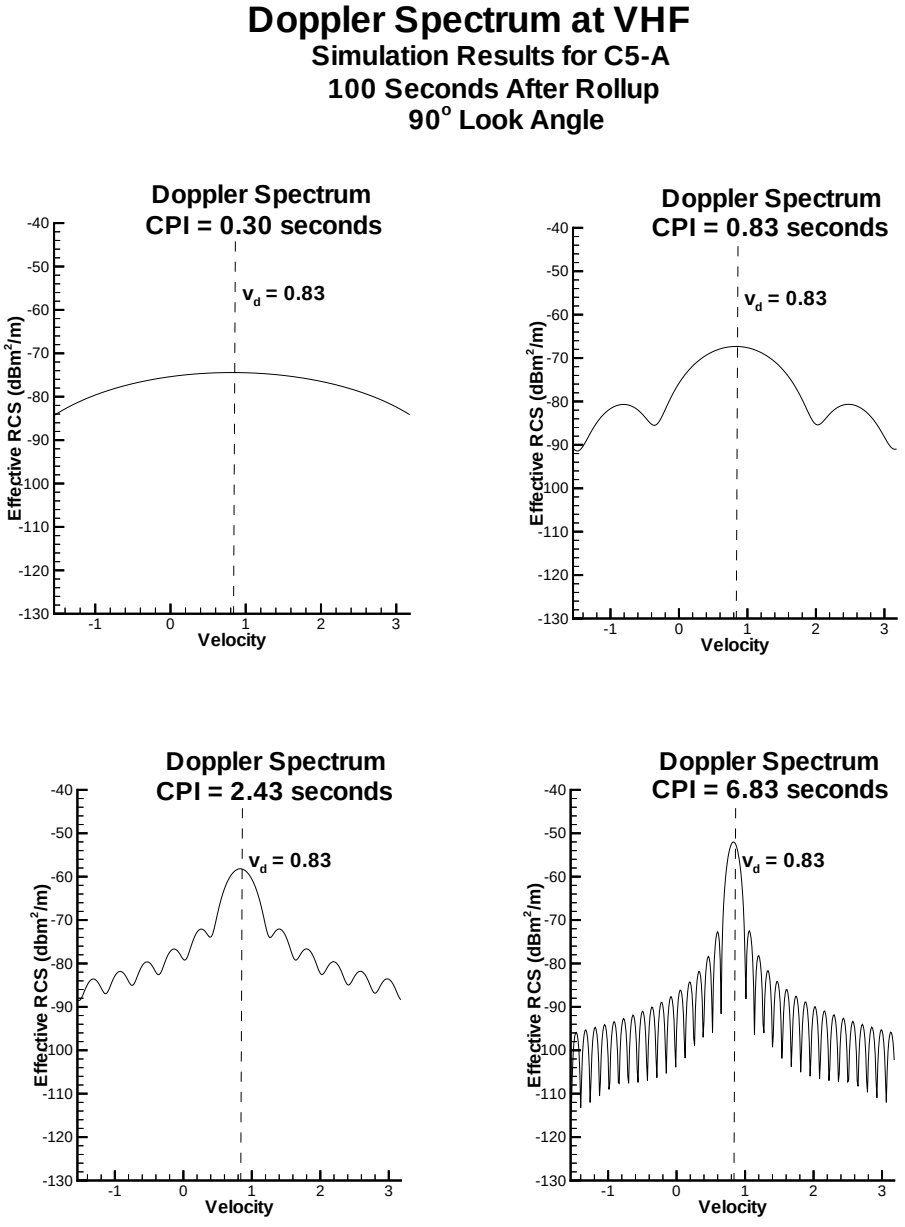

Figure 6.32: VHF Peak Effective RCS

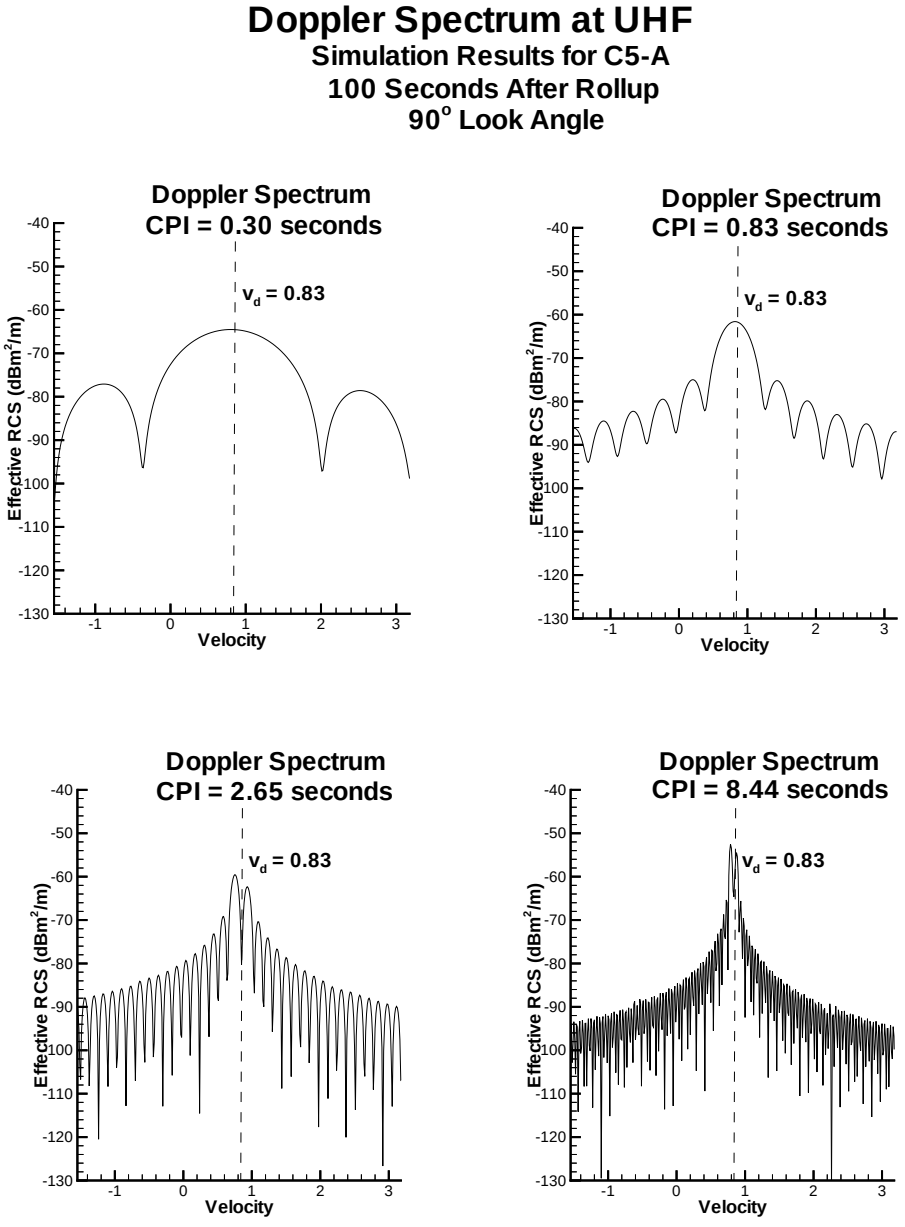

Figure 6.33: UHF Peak Effective RCS

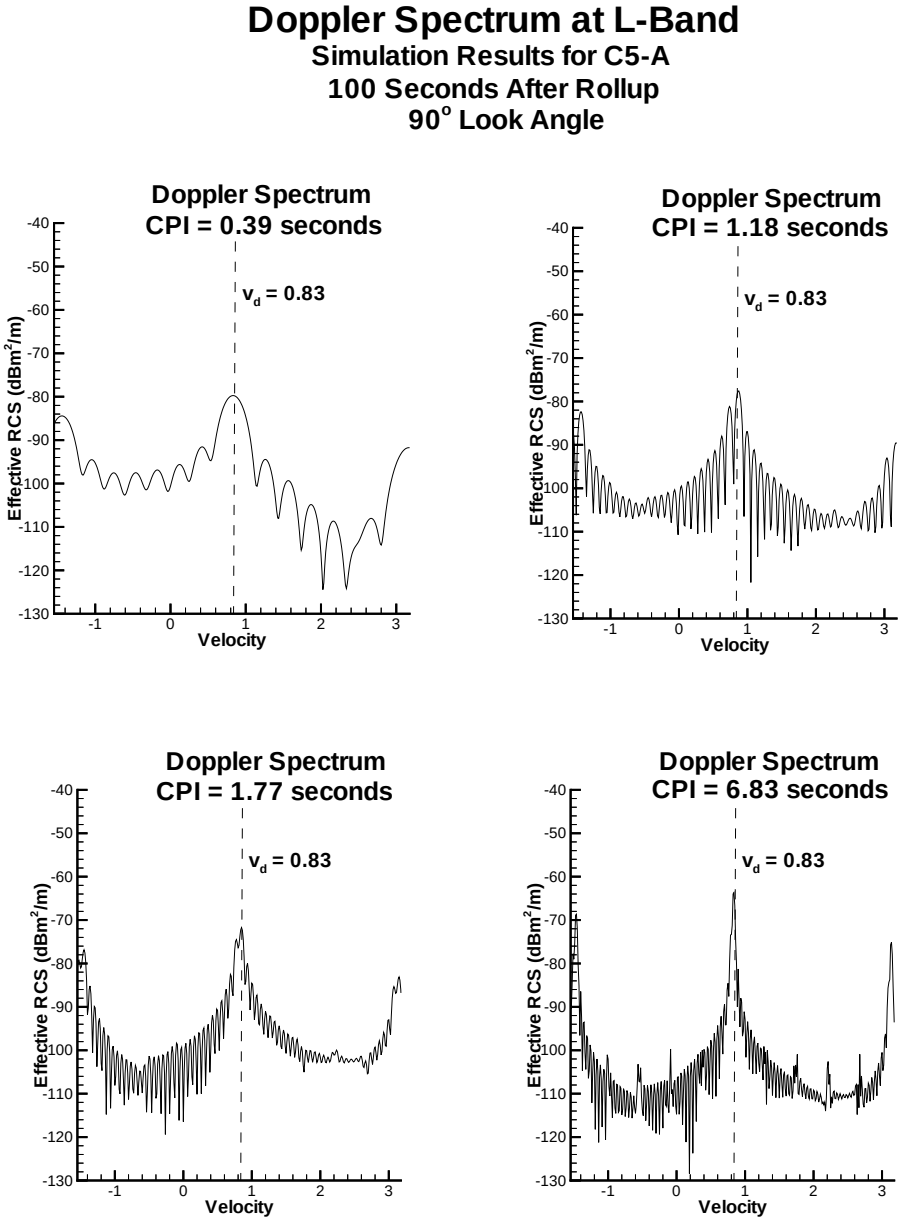

Figure 6.34: L-Band Peak Effective RCS

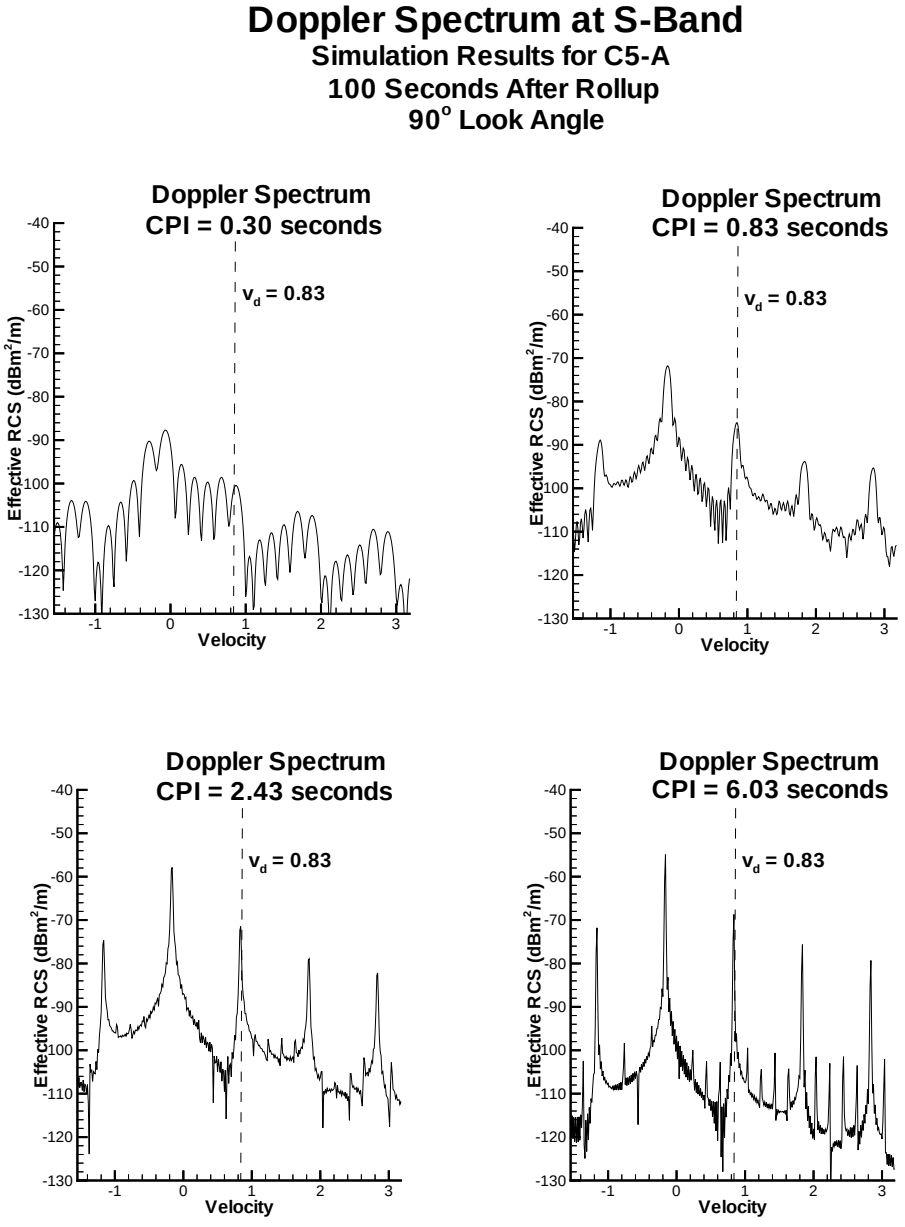

Figure 6.35: S-Band Peak Effective RCS

Chapter 7

Conclusions

7.1 Summary

In this work, radar cross section (RCS) of the aircraft generated wake vortex system that has previously been attributed to turbulent mixing, has been explained by a laminar flow mechanism. The evidence that supports this is:

- Recent literature indicates that previous modeling has greatly overestimated the turbulence levels within the wake vortex system.
- RCS values determined by the Wake Vortex - Passive Conservative Simulation (WV-PCS) yield values that are consistent with experimentally obtained results.
- The amount of time after rollup for the RCS to develop is consistent with that indicated by the simulated laminar flow mechanism.
- The lack of increased experimentally measured RCS by using a bistatic radar is explained by the laminar flow mechanism.

Table 7.1: Frequency Dependence of Important Wake Vortex Detection Parameters

Band	Max. RCS	Eff. RCS	Time for RCS to Develop	Doppler Width
VHF	-84 dBm/m^2	-60 dBm/m^2	10 seconds	1 m/s
UHF	-84 dBm/m^2	-64 dBm/m^2	20 seconds	0.5 m/s
L-Band	-86 dBm/m^2	-74 dBm/m^2	80 seconds	0.2 m/s
S-Band	-84 dBm/m^2	-72 dBm/m^2	unknown	0.05 m/s

For generalization of RCS to various atmospheric conditions and aircraft, a formalism has been developed to allow a single computationally expensive WV-PCS simulation to be extrapolated. A uniform approach has been developed for RCS due to water vapor gradients and potential temperature gradients. This is absorbed in the parameter A in the formalism. In addition, there is a way to extrapolate the parameter, $s(\mathbf{r}, t)$, that is the output of the WV-PCS to other aircraft at the expense of some accuracy.

Enhanced detection may be achieved using a pulsed doppler radar system. The Doppler Processing Simulation (DPS) has been implemented in software to quantify this detection enhancement. The metric used to quantify this is the effective RCS which is the RCS of the target that a single pulse would need for the same signal-to-noise (SNR) ratio of the pulsed doppler system output.

Table 7.1 summarizes some important results from the WV-PCS and DPS simulation of the laminar flow mechanism. Although there are a large number of factors in designing a doppler radar system, this table indicates reasons why the lower frequencies may be more suitable for coherent detection of the wake vortex system:

- The maximum effective RCS for lower frequency bands is several dB larger than that at the higher frequencies.

- The atmospheric structure is stretched to the larger VHF wavelength sized scales more rapidly than the smaller high frequency scales thus the greater RCS due to coherent scatter develops much more rapidly.
- The doppler width is larger at the lower frequencies meaning the exact a priori knowledge of the descent rate, cross wind, and angle to the wake vortex system is not as critical in the lower frequency systems.
- At VHF, for example, a bistatic radar system could be constructed that relies on even smaller scale sizes for coherent detection without a large amount of time after rollup for these to develop.

7.2 Future Work

There are several limitations of the WV-PCS with regards to large wavelength instabilities, non-constant descent rate, and ground effects that are not accounted for in the simulation. However, since the simulation consumes a great deal of CPU time and memory space, incorporation of these factors into the WV-PCS would increase (perhaps by orders of magnitude) and make the simulation not feasible. It is reasonable to conclude that computer simulation can not completely characterize wake vortex phenomenon and its corresponding RCS with current computational capabilities. At this point, it would be advantageous to continue with experiments that measure RCS and doppler spectra. Unlike previous experiments, the doppler processor and doppler processing algorithms could be tailored to the laminar flow mechanism rather than using a broad band doppler assumption that would be more appropriate with turbulent mixing.

An enhancement to the DPS can be made such that the ground clutter effects are simulated. Ground clutter is the unwanted radar return that leaks in through the side lobes of the

antenna. Incorporation of a ground clutter model that is accurate for the geographical location of the radar system would be useful for accurate modeling of the radar return.

A particularly useful radar experiment would be to repeat the bistatic RCS measurement that was performed at L-Band in the Kwajelein experiment, except this time at VHF where coherent Bragg scatter would exist at size scales diminished by the bistatic angle. This may yield substantial RCS especially after appropriate doppler processing.

The development of wake vortex RCS is a complicated phenomenon that neither simulation nor experimentation alone is sufficient to characterize. It is hoped that this work may yield valid insight into the salient features that may be specifically looked for if it is fully accepted that turbulence in not the generator of the RCS. Iterations of experiment, analysis, and simulation may result in a commercially viable product that will effectively track and detect hazardous aircraft generated wake vortices dependably and economically.

Bibliography

[ASRS, 1992] ASRS, N. A. S. R. S. (1992). In flight weather encounters. Technical report, ASRS Office, 625 Ellis Strees, Suite 305, Mountain View, California. Search Request No. 2587.

[Batchelor, 1964] Batchelor, G. (1964). Axial flow in trialing line vortices. *Journal of Fluid Mechanics*, 20:645–658.

[Burnham and Hallock, 1982] Burnham, D. C. and Hallock, J. N. (1982). Chicago monostatic acoustic vortex sensing system, volume iv: Wake vortex decay. Technical Report DOT/FAA/RD-79-103 IV, Department of Transportation. Available from NTIS.

[Devenport et al., 1996] Devenport, W. J., Zsoldos, J. S., and Vogel, C. M. (1996). The structure and development of a counter-rotating wing-tip vortex pair. *Journal of Fluid Mechanics*.

[Eaves and Reedy, 1987] Eaves, J. and Reedy, E. K. (1987). *Principles of Modern Radar*. Van Nostrand Reinhold.

[Gilson, 1991] Gilson, W. H. (1991). Radar measurement of aircraft wakes. Technical report, Massachusetts Institute of Technology Lincoln Laboratories. Project Report AAW-11.

[Hatliner and Williams, 1980] Hatliner, G. J. and Williams, R. T. (1980). *Numerical Prediction and Dynamic Meteorology*. John Wiley and Sons, 2nd edition.

[Karamcheti, 1980] Karamcheti, K. (1980). *Principles of Ideal Fluid Aerodynamics*. Robert E. Krieger Publishing Co.

[Lapidus and Pinder, 1982] Lapidus, L. and Pinder, G. (1982). *Numerical Solution of Partial Differential Equations in Science and Engineering*. Wiley-Interscience.

[Lewellen and Lewellen, 1996] Lewellen, D. and Lewellen, W. (1996). Large-eddy simulations of the vortex-pair breakup in aircraft wakes. *AIAA Journal*, 34(11):2337–2345.

[Lide and Fredericks, 1997] Lide, D. R. and Fredericks, H. P. R. (1996-1997). *CRC Handbook of Chemistry and Physics*. CRC Press.

[Marshall et al., 1996] Marshall, R. E., Scales, W. A., and Myers, T. J. (1996). Radar reflectivity due to turbulent production of refractive index fluctuations in aircraft generated wake vortices. In *Proceedings of the National Radar Conference*.

[Maxworthy, 1972] Maxworthy, T. (1972). The stability and structure of vortex rings. *Journal of Fluid Mechanics*, 51(11):15–32.

[Mayer and Powell, 1992] Mayer, E. and Powell, K. (1992). Similarity solutions for viscous vortex cores. *Journal of Fluid Mechanics*, 238:487–507.

[McCormick, 1968] McCormick, B. (1968). Structure of trailing vortices. *Journal of Aircraft*, 5(3):260–267.

[Newman, 1959] Newman, B. (1959). Flow in a viscous trailing vortex. *The Aeronautical Quarterly*, pages 149–162.

[Ottersten, 1969a] Ottersten, H. (1969a). Atmospheric structure and radar backscattering in clear air. *Radio Science*, 4(12):1179–1193.

[Ottersten, 1969b] Ottersten, H. (1969b). Radar backscatter from the turbulent clear atmosphere. *Radio Science*, 4(12):1251–1255.

[Press, 1986] Press, W. H. (1986). *Numerical Recipes*. Cambridge.

[Proctor, 1996] Proctor, F. H. (1996). Numerical simulation of wake vortices measured during the idaho falls and memphis field programs. *American Institute of Aeronautics and Astronautics*.

[Ragab, 1995] Ragab, S. A. (1995). Direct numerical simulation of instability waves in a trailing vortex. *AIAA*.

[Saffman, 1973] Saffman, P. (1973). Structure of turbulent line vortices. *Journal of Aircraft*, 16(8):1181–1189.

[Schleher, 1991] Schleher, D. C. (1991). *MTI and Pulsed Doppler Radar*. Artech House.

[Schmidt et al., 1984] Schmidt, Henderson, and Wolgemuth (1984). *Thermal Sciences*. John Wiley and Sons.

[Tartarski, 1971] Tartarski, V. I. (1971). *The Effects of the Turbulent Atmosphere on Wave Propagation*. Israel Program for Scientific Transactions.

[Tennekes and Lumley, 1972] Tennekes and Lumley (1972). *A First Course in Turbulence*. The MIT Press.

[Zeman, 1995] Zeman, O. (1995). The persistance of trailing vortices: a modeling study. *Physics of Fluids*, 7(1):135–143.

Vita

Ted Myers was born in Baltimore, MD in 1969. He received the B.S. from Virginia Tech in Electrical Engineering in 1991. During this time he was a Cooperative Education student with IBM. He then received the M.S. from the University of Maryland at College Park in 1992. Afterward, he started with SAIC working on modeling of satellite communication systems. In 1994, he returned to Virginia Tech where he completed the Ph.D. in Electrical Engineering in 1997.